Metamaterial Analogues of Molecular Aggregate Systems

Milo Baraclough
School of Physics
University of Exeter

Thesis submitted for the degree of
Doctor of Philosophy

March 2021

Metamaterial Analogues for Molecular Aggregate Systems

Submitted by Milo Baraclough to the University of Exeter as a thesis for the degree of Doctor of Philosophy in Physics
2021

I certify that all material in this thesis which is not my own work has been identified and that no material has previously been submitted and approved for the award of a degree by this or any other University.

Milo Baraclough
2021

I acknowledge financial support from the Engineering and Physical Sciences Research Council (EPSRC) of the United Kingdom, via the EPSRC Centre for Doctoral Training in Metamaterials (Grant No. EP/L015331/1).

Point of contact for any queries on the thesis/data and relevant code/software is Prof. William L. Barnes, email: w.l.barnes@exeter.ac.uk

In dedication to my grandfather, Graham Baraclough. Your endless enthusiasm to both learn and teach has forever changed me for the better.

Acknowledgements

Working on this thesis as part of the Electromagnetic group and XM^2 at Exeter has been far from a lonely experience, and without many of the people I worked alongside this thesis would be a very different and, I am certain, lesser document.

Firstly, I would like to acknowledge the constant enthusiasm and considered guidance provided by my two supervisors, Prof. Bill Barnes and Dr. Ian Hooper. Thank you always making time when I needed it and pushing me to do my best. Dr. Sathya Sai Seetharaman, who was a fellow PhD student when I started, thank you for showing me the ropes and helping me whenever I was stuck. I would also like to thank Prof. Alastair Hibbins, for allowing me the use of his lab space for my research, and Mark Heath, for showing me how to use to the clean room equipment.

For keeping me sane, or at least for allowing my mental slip to go unnoticed, I acknowledge the Ostriches: Austin, Frank Davies, Elizabeth Martin, Ned Taylor, and Rosamund Herapath. I couldn't have asked for a better group of people to face this with and I wish nothing but the best for all of you. To Ros especially, for weathering two lockdowns with me and for far more than could reasonably fit here.

To my loving parents and other family members who have patiently listened to me explain things I don't fully understand and that they don't care about, thank you. Without you I would not have started this journey, let alone have finished it.

Finally, Jet, for getting me up on mornings when I just wanted to lie in, and for teaching me that any chance at food, no matter how small, is worth going for, thank you. You tried to delete this thesis twice and you may well be the wisest of us all.

Abstract

Metamaterials offer a great degree of control over their physical properties through the tuning of the interactions between their elements within larger structures. Molecular Aggregates are a group of organic molecules that assemble into structures with new optical properties arising from the inter-molecule interactions. Molecular aggregates are a fascinating and important class of materials, particularly in the context of optical (pigmented) materials. The aim of this thesis is combine these two fields in the meta-analogue approach by replicating aggregate behaviour with metamaterials. In this way aggregate phenomena normally observed on the nm scale can instead be probed in great detail at the mm scale of a metamaterial. Simultaneously, new metamaterials can be created that are inspired by the study of aggregates.

Passive resonant metamaterials are limited by the narrow-band nature of the resonances they support. In order to probe the interaction between two resonators more deeply, and guide experimentation with meta-analgoues, I create a tunable Split Ring Resonator (SRR). I show that by incorporating an active component into the structure of the SRR it is possible to tune the resonance frequency of this type of metamaterial atom. I make use of this tuneability to examine the interaction between two resonators, one passive and one active, as the resonance frequency of the active resonator is swept through that of the passive resonator. The resultant modes of this coupled system exhibit an anti-crossing and, by changing the separation between, and relative orientation of, the split-ring resonators, I investigate how the magnetic and electric coupling terms change. I find that the relative orientation of the resonators significantly effects the strength of the coupling. Through both structural and active tuning we are able to alter the relative sizes and signs of the coupling terms.

In the world of researching molecular aggregates it is difficult to precisely examine small numbers of molecules, relying instead on the behaviours of large groups to determine their properties. In the second section I present two meta-analogues of molecular aggregates. A positively dispersive chain of resonators, that couples in a

manner analogous to J-aggregates, and a negatively dispersive chain that couples analogously with H-aggregates. I also present two novel metamaterial chains inspired by the aggregate like structures. In the first a simultaneous negative and positive group velocity is achieved and in the second those counter propagating modes are coupled through the breaking of one of the meta-atom's symmetries, resulting in an anti-crossing and a region of zero group velocity.

In the third results section, in an effort to achieve greater understanding of these systems of aggregate like chains of meta-molecules on the millimeter scale, I exploited the fact that they can be directly probed and rearranged. Using this system I directly observed the effects of various termination and defect types, in the process showing a clear relation between these and those predicted in the SSH model. I intend for this work to open new avenues of interrogation of aggregate structures using metamaterial analogues as well as of direct observation of localised modes.

In the final section I present a meta-analogue of the strong coupling experiment. The formation of polariton modes from the strong coupling of light and matter is an exciting and important field with ramifications from Chemistry to laser physics. It's study is in many ways hampered, however, by the atomic and molecular scale at which interactions take place. In this section I investigate the effects of strong coupling using metamaterial analogues. This allows for the meta-atoms themselves to be directly probed during excitation, and for the nature of hybridised polaritons, and the optically 'dark' states to be shown directly.

Contents

List of Figures

Chapter 1

Introduction

The primary goal of this thesis is to present a novel approach to molecular aggregate study that I will be calling the meta-analogue approach. This approach utilises the parallels in fundamental physics between metamaterials and molecular aggregates to allow for molecular aggregate phenomena to be interrogated in metamaterial form.

Molecular aggregates and metamaterials might not seem like comfortable bed fellows at first glance but they do share some fascinating properties. Both can strongly interact with light, creating hybrids between photon and particle. Both are incredibly sub-wavelength, being made of many discrete parts but interacting with radiation as if they were a contiguous whole, and both have greatly different behaviours in isolation compared to their aggregate/structured form. In many cases where aggregates are used, in both research and application, it is an attractive thought to replace mildly unpredictable organics with highly controlled and uniform metamaterials, however this will almost immediately run into the most apparent difference between the two, scale. The cost and complexity of creating atomic scale metamaterials far outweighs the possible benefits of such a substitution. Far better then to tailor microwave metamaterials, that operate at the centimeter scale, to be analogous to aggregates. The added benefit, of course, being the possibility to find new metamaterial structures as a by-product.

1.1 Thesis Outline

The content of this thesis concerns four broad topics. The first section (chapters 2, 3 and 4) covers the ground work that this thesis builds upon, including the historical context of both fields it seeks to branch, the general theory behind the key physics covered, and the methodologies used throughout. The second section (chapter 5) takes a slight step back from molecular aggregates and focuses on learning what we can from metamaterials in a seemingly simple arrangement, in this case an axially coupled pair. The meta-atoms used throughout this thesis are interrogated thoroughly so as to inform the design decisions made in later chapters.

In the third section (chapters 6 and 7) the meta-analogy is made in earnest. Two metmaterial chains are designed that replicate the coupling dynamics of the two most prominent types of molecular aggregates. These aggregate-like chains also inspire two novel 1D metamaterials that incorporate both types of aggregate coupling; one for simultaneously forwards (positive) and backwards (negative) group velocity waves and the other for mid-brillouin zone anti-crossing.

The aggregate chains are then reconfigured to replicate the Su-Schrieffer-Heeger model. This model was initially created to explain aggregate behaviour that could not be directly probed, and this section concludes by demonstrating meta-analogues that match with those predicted behaviours and can be interrogated in the near field.

The fourth, and final, section (chapter 8) is when the meta-analogy is used to produce a result new to both the fields of metamaterials and molecular aggregates. A classic experiment from the field of molecular strong coupling is that of hybridizing light and matter into a single mode with the character of both. By strongly coupling meta-atoms to a cavity mode we are able to do the same, but take it an extra step and directly probe the form this hybridization takes by mapping electromagnetic fields within the cavity.

Chapter 2

Historical Context

2.1 Metamaterials

Where to start the story of metamaterials is a question entirely dependent on one's definition of them, and such a definition has proven hard to nail down. The first definition I heard was: "A metamaterial is an artificial structure whose properties are dependent on its construction over chemical composition". By this definition, are we to start in the times of prehistory when a stone was first napped to a point, or am I to include the creation of reinforced concrete in my summation? I do not intend to do either, so some pruning is required.

A popular addition is that a metamaterial's properties not be "found in nature", or even "possible in nature", based on the greek definition of 'meta' meaning 'outside of'. A good addition for some, but it still leaves reinforced concrete uncomfortably in my lap while boldly excluding the excellent metamaterial work done replicating the anti-glint features of moth eyes [1]. Discarding the entire metamaterial field of nature-inspired meta-structures also feels self-defeating in a thesis about nature-inspired meta-structures. I could further tinker with my definition, but I think I can be satisfied with one more edit. The properties exhibited result from interaction with waves of significantly longer wavelength than the structure's characteristic spacing. So what is a metamaterial, at least within the bounds of this document? A metamaterial is an artificial structure whose interaction with energy depends on

physical features far smaller than the exciting wavelength rather than its chemical composition.

So, with a definition in hand, where do we start? Human history's full scope could be described as a never-ending drive to wield more energy, more effectively, than we did the day before. It was a Russian named Kardashev who persuasively argued that an alien civilisation, or indeed our own, might be entirely judged by how much energy it could handle [2]. So it is not quite as surprising as it might first seem that the first suggested use of metamaterials was by the Romans, many thousands of years before the term was even coined [3, 4]. Recently, a researcher into microwave materials noted that some ancient structures' foundations reminded him of his work. He found that these architectural placements acted as an acoustic guide that would protect the building in the centre from earthquakes. The pattern has gone on to be found elsewhere in ancient structures, but sadly, there are no writings from the time indicating that their pattern and results were intentional. It may simply be that those buildings still visible in the modern-day will, by architectural natural selection, be those that happen to be capable of weathering earthquakes. However, whether by intent or accident of ancient builders, these buildings, which include the great Colosseum in Rome, have stood the test of time thanks in part to metamaterial designs.

However, we need not travel back so far for the history of metamaterials wielded with documented intent. This thesis is concerned with the part metamaterials have to play in the light-matter interaction, and for that we must start in the relatively recent 1900's and Horace Lamb. In 1904 Lamb presented a circumstance whereby the equations governing a system could produce a backwards group velocity [5]. While the mathematics presented were exciting, it was considered impossible to realise due to the calculations' outlandish material properties. Lamb himself ends the cited paper with a lamentation. "It is hardly to be expected that the notion of a negative group-velocity will have any very important physical application" and concluded that his work serves only as a warning to those working in a dispersive medium and using theorems formulated from waves in air.

In 1968 Veselago calculated the dynamics of a system with simultaneously negative values of permeability (μ) and permittivity (ϵ) [6]. He then went on to show how such a system would exhibit a negative refractive index. However, Veselago notes in his work that no isotropic material exists with a negative μ and work at the time, on gyrotropic materials and ferrites, was yet to achieve the desired features [7, 8]. Even then, he shows how a negative index will only be possible when μ and ϵ have a frequency dependence, foreshadowing perhaps the importance of resonant metamaterials. In 1987 Eli Yablonovitch pioneered the theory of photonic crystals [9], which some now consider a kind of metamaterial [10]. To these researchers, the mathematics offered up possibilities that their materials could not match, but it is in replicating the features they predicted that the first "modern" metamaterial was conceived.

In 1994 John Pendry published his paper on photonic bandgaps in metallic structures that are structured on a scale comparable with that of the exciting wavelength [12]. He expanded on this theme in multiple works [13, 14], examining structures far smaller than the exciting wavelength and showing how a non-magnetic material could still be coaxed into producing an effective permeability. The realisation, and why I specified earlier that a meta-material be dependent on features smaller than the exciting wavelength, was that a non-continuous structure could be treated as a continuous effective medium to the light of a suitably long wavelength. It was not long after, in 2000, that Veselago's negative refractive index medium was experimentally realised by Smith *et al.* [11], acknowledging the use of unpublished research by Pendry. I have duplicated in Figure 2.1 the key result from Smith's work. Using a periodically arranged combination of straight wires and elements known as a split-ring resonators Smith was able to achieve the desired parameters over a narrow bandwidth. That same year the first conference proceeding to use the term metamaterial directly was published by Eli Yablonovitch [15], and the field was, essentially, born.

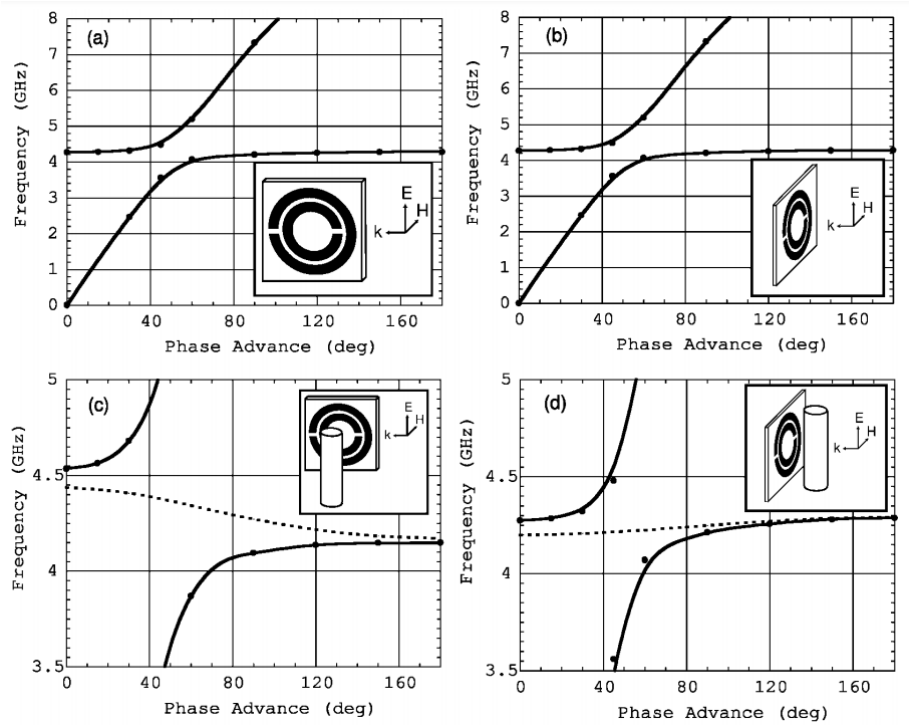

Figure 2.1: Duplicated from [11]. (a) Dispersion curve for the parallel polarisation H. The lines with the solid circles correspond to the split-ring resonators only. The inset shows the orientation of the split-ring with respect to the incident radiation. The horizontal axis is the phase advance per unit cell, or kd, where k is the wavenumber. (b) Dispersion curve for the perpendicular polarisation H. The lines with the solid circles correspond to the split-ring resonators only. The inset shows the orientation of the split-ring with respect to the incident radiation. (c) Expanded view of the dispersion curve shown in (a). The dashed line corresponds to the split-ring resonators with wires placed uniformly between split-rings. (d) Expanded view of the dispersion curve shown in (b). The dashed line corresponds to the split-ring resonators with wires placed uniformly between split-rings. The insets to (c) and (d) show the split-rings' orientations with respect to the wires. Of particular interest is the negative dispersion curve of the dashed line, indicating a negative group velocity, in panel (c).

Of particular interest to this report (Chapters 6 and 7), in 2003 Shamonina, Solymar *et al.* analytically formulated and practically displayed [16–18] a new type of wave inside of metamaterial structures. Magneto-inductive waves, as they termed them, were a result of magnetic coupling in chains of resonators inducing a varying voltage in those resonators. This was followed in 2006 when Beruete and Falcone [19] designed a complementary structure with a corresponding Electro-inductive wave being supported.

With its unique waves and material properties, metamaterial research has progressed leaps and bounds since its nascence, covering a wide range of topics and

applications [20–22]. From superlenses to miniature antennas and city planning projects [23–25]. They are a powerful tool for achieving the novel, increasing efficiency and, I believe, if furthering our understanding of phenomena that typically we cannot directly probe.

2.2 Molecular Aggregates and Strong Coupling

A molecular aggregate is a collection of molecules that, when brought to a high enough concentration, will assemble, or 'aggregate', into a structure with notably different optical properties to those of the individual molecules. These new properties are due to the inter-molecular interactions within the stack and are dependent on what kind of arrangement is formed (the most simple two being side by side or end to end). They were first observed in a 1936 letter to the editor of Nature in which Edwin Jelley reported the presence of a resonant mode in an aqueous solution of dye molecules [26]. The original results that Jelley published are duplicated in figure 2.2. A sharp absorption band appeared in his measurements at a wavelength of 575 nm when the solution was transitioning and disappeared when the crystalline state was reached. This band was notably red-shifted in frequency compared to the dye's typical (monomer) absorption spectrum. It was also strongly dependent on the solution's concentration, the feature disappearing at low concentrations, which violated the Beer-Lambert law (that the absorption of a solution will be linearly dependent on concentration) [27]. He had discovered the phenomenom of molecular aggregation, though he misattributed the feature as intrinsic to the dye itself rather than the aggregates it was forming. It was a German researcher named Scheibe, who had coincidentally made the same observation as Jelley in the same year [28], but was published later and in German, who correctly identified the source of the feature in 1938 [29]. The molecular chromophores in the solution where aggregating themselves into chains, head to tail, via the coulomb interaction and their coupled response was creating the new absorption band. That type of aggregate where head to tail, or equivalent, structures are formed would become known as a Jelley, or J-, type aggregate for its discoverer. J-aggregates quickly became of great practical

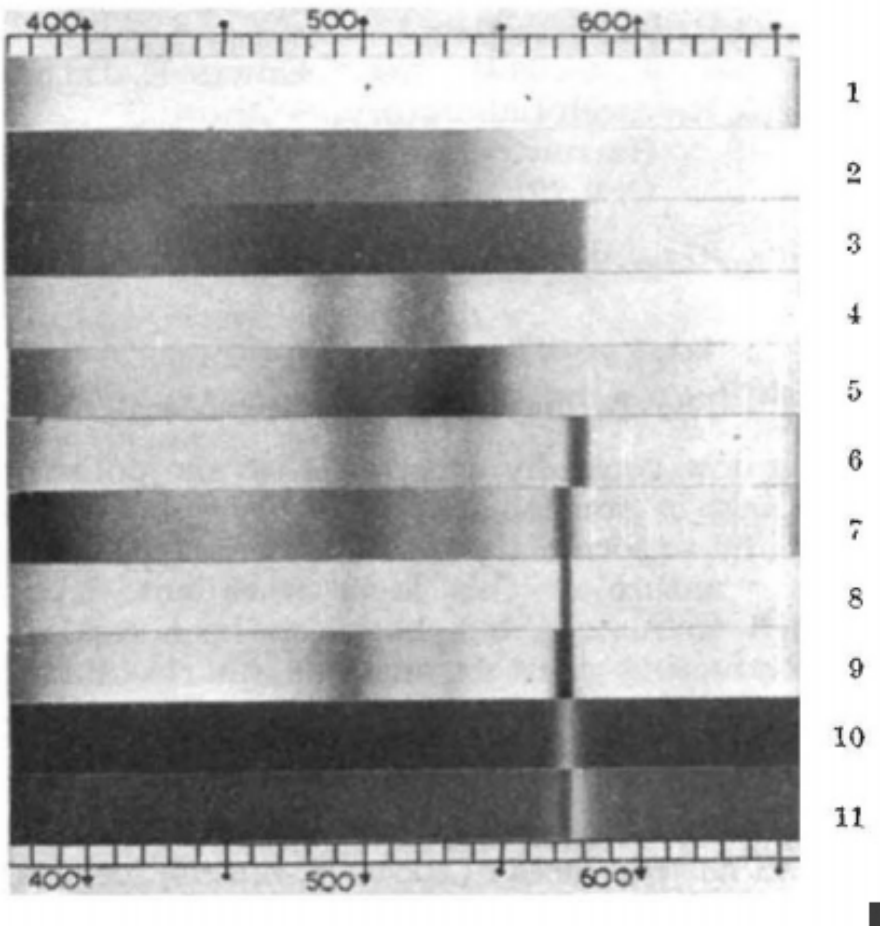

Figure 2.2: Duplication of Edwin Jelley's results, published in 1936 by Nature [26]. 1. Spectrum of a Tungsten lamp, 2-3. absorptions of the crystal state in X and Y, respectively, 4-5. Absorptions of methyl alcohol and nitrobenzene 6-9. Absorption of the dye as a suspension in toluene, dispersed in benzophenone crystals, and a solution with sodium chloride at two different dye concentrations, 10-11. Fluorescence of the dye in sodium chloride solution and the same after passing through an un-illuminated solution to superimpose the absorption.

import when it was found they could be used in the development of film as a chemical sensitiser, transferring the energy they absorbed to other molecules instead of re-releasing it as luminescence [30].

Interest in the field of aggregate chemistry grew steadily. Many different dyes were found and synthesised that exhibited the J-aggregate features of a very sharp red-shifted absorption peak. There was also found a second type of aggregate that exhibited the reverse feature: a blue-shifted absorption peak. In this case, rather than assembling end to end, the molecules aggregate into side by side structure. These were called H-type aggregates after their Hypsochromic shift in absorption (the red-shift of a J-aggregate is Barochromic). Some molecules can even exhibit

both under differing circumstances [31]. The effect depends on how the molecules aggregate rather than something intrinsic to the monomer.

Concurrently with work on aggregate molecules, researchers were pushing the bounds of what could be achieved through the light/matter interaction. As early as 1946, Purcell noted that spontaneous emission rates, which many had considered near constant for a given atom, were greatly enhanced inside a cavity compared to the same atom outside of the cavity [32]. This observation, known now as the Purcell effect, where spontaneous emission is affected by an emitter's environment, opened the door to more adventurous investigations in the 1960s where mirrors and cavities could manipulate atoms' chemical properties in their proximity.

In 1992, by confining a series of quantum wells [33], or atoms [34], within an optical cavity, researchers were able to couple the exciton (molecular) modes of the wells/atoms to the photon mode of the cavity. Significantly, this interaction could be pushed into the strong coupling regime where the exchange of energy between the excitonic and photonic modes is faster than the rate of the system's losses, and a photon may be absorbed and released multiple times before escaping the cavity [35–37]. In the strong coupling regime, the two modes hybridise into an exciton-photon quasi-particle. Part light, part matter, these states are known as polaritons, and they can be used to fundamentally change the transition energies of semiconductors confined within a cavity. The methodology offered new ways to examine and exploit exciton-based processes, and in 1998 Lidzey *et al.* were the first to push an organic aggregate into the strong coupling regime [38].

This new field, known as 'polaritonic chemistry', arose from the opportunities such hybridisation offered to explore and exploit new phenomena and new materials [39–44]. When this light is hybridised with excitonic resonances, exciton-polaritons are formed [45]; when molecular vibrational or lattice phonon resonances are involved, then vibro-polariton [46, 47] and phonon-polaritons [48, 49] are formed. The attraction of this mixing of light and matter led to developments such as polariton lasers [50] and Bose-Einstein condensation [51–53], whilst with the rapid rise of interest in polaritonic chemistry strong coupling has been reported to lead

to modified chemical reaction rates [54–56], modified inter-molecular energy transfer [57–59], modified exciton transport [60, 61], altered phase transitions [62], and a potential re-ordering of singlet-triplet energies [37, 63, 64]. Whilst a great deal has been done in this area, much of it sparked by the pioneering work of the Ebbesen group over the past decade [39], much still remains to be understood [65].

The visible and infrared wavelengths of the light involved in these fascinating phenomena mean that the spatial scale of the structures used in these experiments is necessarily small. Consequently, whilst one would ideally probe these systems at the molecular level so as to probe the precise nature of the light-matter hybridisation, this is not really feasible [66].

2.3 Summary

Both the fields of polaritonic chemistry and metamaterials have, and continue to, generate much excitement within their respective communities and beyond. They both seek to exploit the resonant interaction between light and matter. Both are arguably, less than forty years old, having produced their first dedicated publication in 1998 and 1999, respectively. Both are governed by dipole interactions between elements far smaller than the exciting wavelength. In combining them into a new meta-analogue approach, which I will describe in this thesis, I hope to facilitate advancement in both. Analogue inspired metamaterials may provide effects or efficiencies not currently achieved, whilst meta-analogue structures can offer insights into aggregate interactions not probeable at the atomic scale.

Chapter 3

Theory

3.1 Coupled Oscillators

Coupled oscillator physics is integral to the behaviour of both molecular aggregates and metamaterials. The basic idea of coupled oscillators is that a number of separate resonators, when coupled together by some interaction, will act as a single oscillatory system. This interaction might be the overlap of field profiles or chemical bonds between molecules. One of the most basic forms is the classical, or Newtonian, case of masses coupled together by springs which can be seen represented in Figure 3.1. For ease of understanding it is the physics of this case that I will cover first.

3.1.1 Newtonian

Coupled Pair

A mass, m, connected to a fixed point via a spring of constant k will harmonically oscillate at a resonance frequency given by $\omega_1 = \sqrt{\frac{k_1}{m}}$. Introducing a second oscillator with identical parameters will not change this behaviour, and considered as a complete system these oscillators can be said to have two degenerate modes. Irrespective of the relative displacements between the masses the frequency of oscillation will remain the same.

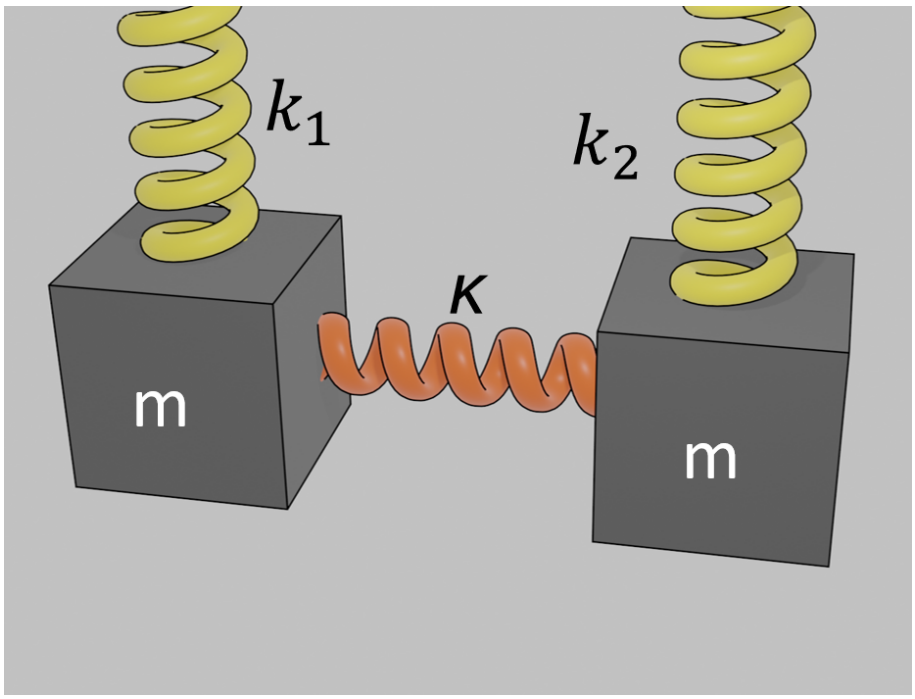

(a)

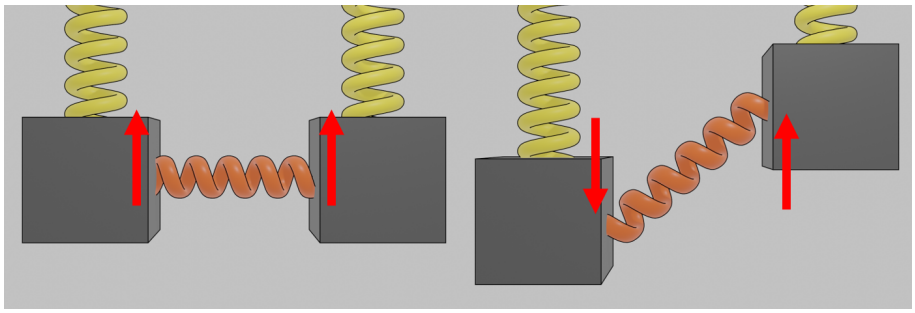

(b) (c)

Figure 3.1: (a) schematic of two spring mass harmonic oscillators, with mass m and spring constant k_1 and k_2, coupled together by a spring of spring constant κ. (b) Lowest energy mode of oscillation where both oscillate in sync and apply no torsion to the coupling spring. (c) The highest energy mode where both oscillate fully out of phase and applying the maximum distention to the coupling spring allowed by their displacement

In order to display coupled behaviour our oscillators need some kind of interaction through which the displacement of one can apply some force to the other. A connecting spring, constant κ, can provide this interaction. Without doing any mathematics there are two obvious ways for this system to behave, that is with both masses moving in phase and completely out of phase. For the in phase case the connecting spring experiences no tension as the relative displacement of each mass remains the same, whilst the out of phase case applies a sinusoidal tension to that same spring. Intuitively, more energy is required to deform the spring. From

this alone, then, we can see that our coupled system will have two modes at different frequencies. This splitting of modes is an indicative feature of coupling in a system.

The nature of this splitting can be found by considering our oscillators mathematically. From the Newtonian equations of motion $F = ma(t) = -kx(t)$ and using the harmonic solution $x_n(t) = e^{i\omega_n t}$ we get for one of the oscillators:

$$-m\omega_{\pm}^2 x_1 = x_2\kappa - x_1(k_1 + \kappa) \tag{3.1}$$

where $\omega_{\pm}$ could be either the upper or lower of the system's resonant frequencies. When combined with the equivalent equation for the second oscillator the system can be fully represented by the following matrix equation:

$$\omega_{\pm}^2 \begin{bmatrix} x_1 \\ x_2 \end{bmatrix} = \begin{bmatrix} \omega_1^2 & -\frac{\kappa}{m} \\ -\frac{\kappa}{m} & \omega_2^2 \end{bmatrix} \begin{bmatrix} x_1 \\ x_2 \end{bmatrix} \tag{3.2}$$

We want to find what the possible values of $\omega_{\pm}$ are that satisfy equation 3.2 as they will correspond to the resonances of the system. Rearranging to make one side of the equation zero gives,

$$0 = \begin{bmatrix} -\omega_1^2 - \omega_{\pm}^2 & \frac{\kappa}{m} \\ \frac{\kappa}{m} & -\omega_2^2 - \omega_{\pm}^2 \end{bmatrix} \begin{bmatrix} x_1 \\ x_2 \end{bmatrix} \tag{3.3}$$

which can be solved by finding the determinant of the central matrix, the equation for which becomes 3.4,

$$\omega_{\pm}^2 = \frac{1}{2}\left(\omega_1^2 + \omega_2^2 \pm \sqrt{(\omega_1^2 - \omega_2^2)^2 + 4\Gamma^2\omega_1\omega_2}\right) \tag{3.4}$$

where $\Gamma = \frac{\kappa}{m\sqrt{\omega_1\omega_2}}$. Γ is used because in experiment the values of κ and m, or their equivalents in a non-Newtonian oscillator, may be unknown with only the frequency of oscillation being directly measurable. Γ also shows an interesting feature when $\omega_1 = \omega_2$ in equation 3.4.

$$\omega_{\pm} = \sqrt{\omega^2 \pm \Gamma\omega} \tag{3.5}$$

The value of Γ, which can be considered as the coupling frequency, can be determined from data by assuming that $\omega \gg \Gamma$ and performing a Taylor expansion on equation 3.5, the first two terms of which give $\omega_\pm = \omega \pm \frac{\Gamma}{2}$ and thus that $\omega_+ - \omega_- = \Gamma$. In other words, Γ represents the magnitude of the splitting due to the coupling between two identical oscillators. The more energy that is exchanged between oscillators via coupling, the greater the difference between the frequencies of coupled resonances.

From these simple observations we can easily intuit a very important coupling result for coupled systems where the resonators no longer all have the same resonance frequency. Consider a system where two resonators are again coupled, but $\omega_1 \gg \omega_2$. Then equation 3.4 simplifies to give $\omega_+ = \omega_1$ and $\omega_- = \omega_2$. In this regime there is no notable change in the resonance frequency of each oscillator despite their coupling. If, through some arbitrary tuning parameter, one of the oscillators is shifted back to $\omega_1 = \omega_2$ and then out of it again the modes, plotted against that parameter, would appear as in Figure 3.2. This feature is commonly referred to as an anti-crossing (depending on what each line represents it might also be called a mode or level repulsion) and is important to the experimental identification of coupling. Measuring the frequency separation between the anti-symmetric and symmetric modes at the tuning parameter where the uncoupled modes would cross will give the value for Γ. If they do not in fact cross then the coupling term can still be derived from fitting to the coupled modes if enough is known about the constituent elements of the system.

We can even check our initial intuition on what the coupled modes might physically look like by solving equation 3.4 for the vector $\left(\begin{smallmatrix} x_1 \\ x_2 \end{smallmatrix}\right)$. By factoring our solutions into equation 3.5 we find that there are two displacement vectors that satisfy the equation which are $\left(\begin{smallmatrix} 1 \\ 1 \end{smallmatrix}\right)$ for the ω_- solution and $\left(\begin{smallmatrix} 1 \\ -1 \end{smallmatrix}\right)$ for the ω_+ solution. These correspond to the in phase and out of phase displacement cases. These vectors and the two values given by equation 3.4 are the eigenvectors and eigenvalues of the matrix $\left(\begin{smallmatrix} \omega_1^2 & -\frac{\kappa}{m} \\ -\frac{\kappa}{m} & \omega_2^2 \end{smallmatrix}\right)$.

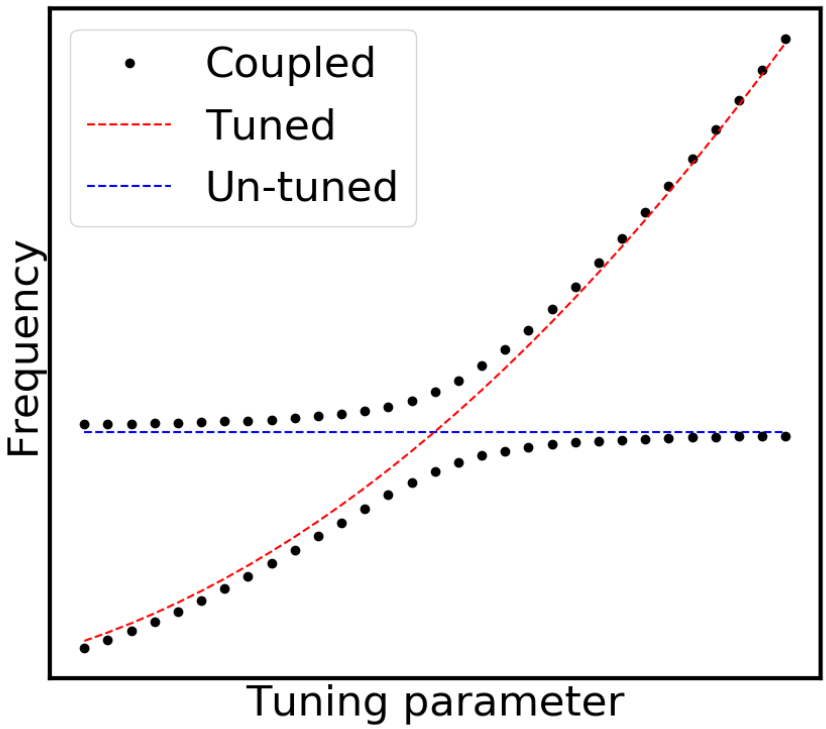

Figure 3.2: Plot of upper and lower resonant modes in a two oscillator system as the frequency of one is tuned through the frequency of the other in both the uncoupled (dashes) and coupled cases (dotted). Modes in the coupled case exhibit an anti-crossing which is proportional to the coupling frequency Γ.

Coupled Chain

Having examined the coupled pair we should ask how further additions of coupled oscillators will affect the system. Consider N identical oscillators arranged in a circle. Each oscillator consists of a mass, m, attached to a fixed point by a spring with constant k. Each individual oscillator has a resonance frequency of $\omega_n = \sqrt{\frac{k_n}{m_n}}$ and is connected to its nearest neighbour by a spring with constant κ_n. As with the coupled pair we can first see that intuitively there will be N modes with a lowest energy mode matching the in phase case where minimum tension is applied to the coupling springs, a highest energy mode where each spring reaches maximum tension and N-2 arrangements that will lie in between. These new coupled modes can be derived exactly again from the equation of motion for a single resonator n:

$$m_n \frac{\mathrm{d}^2 x_n}{\mathrm{d}t^2} = x_{n-1}\kappa_{n-1} - x_n(\kappa_n + \kappa_{n-1} + k_n) + x_{n+1}\kappa_n \tag{3.6}$$

where m_n is the oscillating mass n, x_n is the displacement of mass n at time t, k_n is the spring constant of the spring only connected to mass n and κ_n is the spring constant of the spring connecting m_n to m_{n+1}. By assuming that the oscillation is still harmonic as it was for the coupled pair we can write out the whole system as a matrix for N coupled oscillators.

$$\begin{bmatrix} \omega_1^2 & -\frac{\kappa_1}{m} & 0 & \cdots & -\frac{\kappa_N}{m} \\ -\frac{\kappa_1}{m} & \omega_2^2 & -\frac{\kappa_2}{m} & \cdots & 0 \\ 0 & -\frac{\kappa_2}{m} & \omega_3^2 & \cdots & 0 \\ & & & & \vdots \\ \vdots & \vdots & \vdots & \ddots & -\frac{\kappa_{N-1}}{m} \\ -\frac{\kappa_N}{m} & 0 & 0 & -\frac{\kappa_{N-1}}{m} & \omega_N^2 \end{bmatrix} \tag{3.7}$$

So far so similar to the coupled pair, though with the addition of non-zero elements at the top right and bottom left of the matrix to show the closed loop nature of the chain. It can even be solved in the same manner, though this time requiring computational methods as N very quickly becomes too large to be reasonably solved by hand. Since an N x N matrix will have N eigenvalues we can see that a system of N masses will have N modes of oscillation.

As N approaches infinity these modes will become a continuum between lowest and highest resonances. These represent not just modes of the entire chain, but frequencies that, when excited within the chain, can propagate along it. The representation of these continuous 'bands' of modes is called a dispersion plot and the relevant methods and use of these dispersion plots in experiment are covered in section 4.4.2.

3.1.2 Hamiltonian

In the previous discussion of coupled oscillators I focused on the Newtonian forces applied to each oscillator to calculate their movements and derive their coupled behaviour. Whilst I will make use in later chapters of analogies to the Newtonian mass-spring system, as its behaviour is clearly comparable and it is easier to visualise, for molecular aggregates and metamaterials it is not a perfect mirror. Or, more accurately, whilst the mathematics might be the same it is not always simple to find direct substitutes for both mass and spring.

In these cases the modes of a system can be instead considered in terms of their energy, with an added bonus that frequency and energy have the relationship, $E = \bar{h}\omega$, so are trivial to interchange. In an electromagnetic case there may not be any motion in the system from which to derive the forces required for equation 3.6 and so a method rooted entirely in terms of resonant frequencies is valuable. The Hamiltonian, an equation representing the energy of a system, of the oscillators can be used for this purpose. To show how the electromagnetic and the classical can still be analogous, however, I will continue to make use of the two coupled masses on springs example. The Hamiltonian for a single mass would be of the form given in equation 3.8.

$$\begin{gathered} H = T + V \\ H = \frac{p_1^2}{2m} + \frac{1}{2}kx_1^2 + \frac{1}{2}\kappa(x_1 - x_2)^2 \end{gathered} \tag{3.8}$$

where T is the energy of an uncoupled oscillator, V is the energy exchanged between the coupled oscillators, and p_1 is the momentum of the oscillator. This Hamiltonian consists of two parts. The uncoupled Hamiltonian of the oscillator, $\frac{p_1^2}{2m} + \frac{1}{2}kx_1^2$, which should be equal to $\bar{h}\omega$, and the energy exchanged with the second oscillator due to the coupling spring, $\frac{1}{2}\kappa(x_1 - x_2)^2$, or the interaction energy. Since each oscillator will contribute the same interaction energy to the total value of Γ the interaction energy of a single oscillator is $\frac{\Gamma}{2}$. The full system can then be written as a Hamiltonian matrix 3.9, with eigenvalues corresponding to the energies of the normal modes.

$$\begin{bmatrix} \bar{h}\omega_1 - H & \frac{\Gamma}{2} \\ \\ \frac{\Gamma}{2} & \bar{h}\omega_2 - H \end{bmatrix}_{det} \qquad H_{\pm} = \frac{1}{2}\left(\bar{h}\omega_1 + \bar{h}\omega_2 \pm \sqrt{\bar{h}^2(\omega_1 - \omega_2)^2 + \Gamma^2}\right) \quad (3.9)$$

This can be again simplified by assuming identical oscillators to $H_{\pm} = \bar{h}\omega \pm \frac{\Gamma}{2}$ which gives the same splitting of Γ between upper and lower modes that was found with the Newtonian equation of motion and only requires that the resonance frequencies of the uncoupled oscillators be known for measurement.

3.1.3 Mode Width and Shape

It is mathematically convenient to a assign a resonant mode with a single value for frequency. It implies, however, that the appearance of such a mode, when measured, would be that of a dirac delta function at that assigned frequency alone. The fact that this is not the case, that a resonant mode in truth takes on the appearance of a Gaussian or Lorentzian distribution when measured is not, in all cases, the fault of unreliable measuring equipment. A mode's width and shape can be determined from the resonator alone and represented mathematically in the equations used above.

Returning again to a single mass and spring oscillator we know that, in the real world, it will not oscillate forever without some driving force. This is because the system contains vectors for energy to be lost, be they by sound, heat or friction, which damp its motion and bring it to an eventual halt. This can be represented mathematically by incorporating an imaginary part into the mode frequency. In measurements of a resonant mode, damping manifests in a broadening of that mode into an approximately Lorentzian shape when plotted against frequency [67]. The degree of the broadening is determined by a decay constant $\frac{1}{\tau}$. This decay constant incorporates all sources of decay and marks the time at which a passive oscillator will reach $\frac{1}{\mathrm{e}}$ (where e is Euler's number) of its starting energy. The full width of the mode at its half maximum value (FWHM) of the mode's line shape will then be $\frac{1}{2\pi\tau}$

In a microwave metamaterial structure, losses are not necessarily entirely linked

to material losses. Elements at resonance can be highly scattering, and in an unbounded system there will be losses to free-space radiation. In fact the easier a mode is to excite, i.e. the better it couples to radiation, the broader the mode will be as it then scatters more easily out into free space. This radiative load can be used to find the Q-factor of a given resonator with the following equation:

$$Q = \frac{1}{R_0}\sqrt{\frac{L}{C}} \tag{3.10}$$

where L is the inductance of the resonator, C the capacitance and R_0 the total losses of the system, calculated as the sum of material losses, radiative load, and any other loss vector. Q factor can also be defined as the central frequency (ω_0) of a resonant feature divided by the FWHM of the feature , and thus be found without knowledge of the precise inductive and capacitive components of a resonance.

Finally, a mode of an ensemble system of uncoupled or weakly coupled resonators, such as some molecular aggregates, might also be broadened by random disorder between its constituent resonators. This is not due to any increase of loss in a disordered system, but simply that if the constituent resonators cover a broader range of resonances, the resulting ensemble response will inevitably also be broader. This kind of broadening, known as inhomogeneous broadening, doesn't offer any information as to losses in the system that may be useful to a study. Fortunately, it also has an indicative feature; the broadening it causes in the mode is Gaussian in nature. This allows it to be distinguished from the Lorentzian (homogeneous) broadening caused by losses. In a real world system there is likely to be both randomness and loss, in which case the resulting mode will be a combination of the two types, but if inhomogeneous broadening is small enough, smaller in effect than the losses, it can be separated out from the mode's homogeneous character with a suitably sophisticated fitting algorithm [68].

3.2 Meta-atoms

As the spring and mass is to a resonant chain, and a true atom to a molecule, so a meta-atom is to a metamaterial. If the definition of a metamaterial is loosely defined then that of a meta-atom is looser still but they are, in general, the unit building blocks of a metamaterial. This is not to confuse them with a unit cell. In a periodic metamaterial array, such as Smith's negative refractive index structure pictured in figure 2.1 or the system examined in Chapter 7, the unit cells of the structure may contain multiple meta-atoms. Understanding the properties and behaviours of meta-atoms and their interactions is an integral first step to designing the collective responses of useful metamaterials. In this thesis I also refer to meta-molecules which should be considered interchangeable in purpose with meta-atoms. Meta-molecule is simply used to maintain the clarity of the aggregate analogy. In this section I will describe the physics behind a commonly exploited meta-atom, the Split-Ring Resonator, and how these properties affect its design and application both in general and in its uses in this thesis.

3.2.1 Split-ring Resonators

A split-ring resonator (SRR) is a sub-wavelength component that consists of a ring of metal with a split cut into the ring. It has played an enduring part in metamaterial research since John Pendry *et al.* [14] made use of them for his 'invisibility cloak', and not merely because of its brush with celebrity. The devices used by Pendry *et al.* [14] also incorporated a central split-ring within the first and rotated 180° in the plane, but for the basics of the SRRs function to be understood this needn't be included. When current is passed through the ring it induces two dipole moments. A magnetic dipole normal to the plane of the ring and an electric dipole across the gap that is parallel to the plane. A schematic of these dipoles and the inducing current can be seen in Figure 3.3.

Vitally for their use in microwave and radio frequency applications, such a response can also be initiated by the impinging of electromagnetic fields that excite one or more of the resonator's dipoles and in turn a harmonically oscillating current. When the excitation is at a frequency that matches the resonance frequency of the SRR, these oscillations become greatly enhanced, scattering the incident radiation to a degree that might be expected from a far larger component.

A section of wire has resonance frequencies that are almost entirely governed by its length (L). Each mode represents a spatially varying current density within the wire with the wavelength of its n^{th} resonant mode being $\lambda_n = \frac{2L}{n}$. The lowest frequency mode, where n=1, is only twice the scale of the element it excites. A more complex design is required to become further subwavelength.

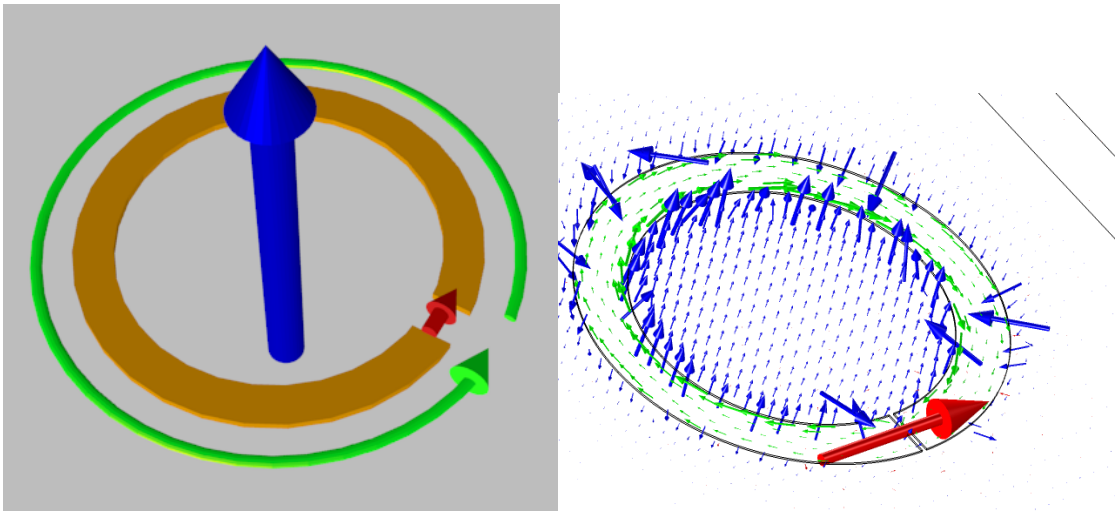

(a) (b)

Figure 3.3: (a) Schematic to illustrate the dipole moments associated with a split-ring resonator. The magnetic (blue) and electric (red) dipole moments of a split-ring resonator are shown, along with the direction of the instantaneous current around the ring (green). Note that the electric dipole moment is localised around the split region where there is maximal charge accumulation, whilst the magnetic dipole moment passes through the centre of the ring due to the circulating currents. (b) Simulated arrow plots of the electric (red) and magnetic (blue) fields, along with the induced current (green), around an SRR. In comparison to the simplified schematic, it should be noted that rather than being focused in the centre of the ring the magnetic fields hug the copper edge, this is important to consider when predicting the near-field interactions involving SRRs. Simulation performed with COMSOL

A SRR has a significant capacitance, partly from the proximity of the two oppositely charged ends and partly from opposite charges on the edge of the ring, to go along with the wire's inductance. This is what allows it to resonate at wavelengths much greater than a simple analysis of its length would suggest. The SRR behaves instead as a resonant LC circuit [69] with an inductance L granted by the ring acting as a single loop inductor and a capacitance (C) from the parallel plates created by the gap. Thus it has a resonance frequency, given in equation 3.11.

$$\omega_0 = \frac{1}{\sqrt{LC}} \tag{3.11}$$

The values for L and C are dependent upon the SRR's physical dimensions of wire width (w), ring inner radius (R), metal height (h) and gap width (g). A SRR's inductance can be closely estimated by simply ignoring the split and finding the inductance of a closed ring, the formula for which is shown in equation 3.12 where $R_m = R + \frac{(w)}{2}$, or the average radius, and μ is the permeability of the medium surrounding the ring.

$$L = R_m \mu \left(\ln \left(\frac{8R_m}{h+w} \right) - \frac{1}{2} \right) \tag{3.12}$$

The capacitance of the ring is more complex to find as it incorporates far more components. Sydoruk *et al.* [69] showed that the contribution of across ring capacitance is too great to be disregarded from calculations and acts in parallel to the capacitance of the gap. Equation 3.13 shows the terms needed to calculate a ring's total capacitance.

$$C_{tot} = C_{gap} + C_{edge} \tag{3.13}$$

The equivalent circuit of the SRR thus has the form shown in Figure 3.4b. To find the total capacitance of the ring and calculate equation 3.11 both C_{gap} and C_{edge} must be derived.

The value of C_{gap} is found by treating the split in the ring as a parallel plate capacitor and using equation 3.14 with the addition of a C_0 factor.

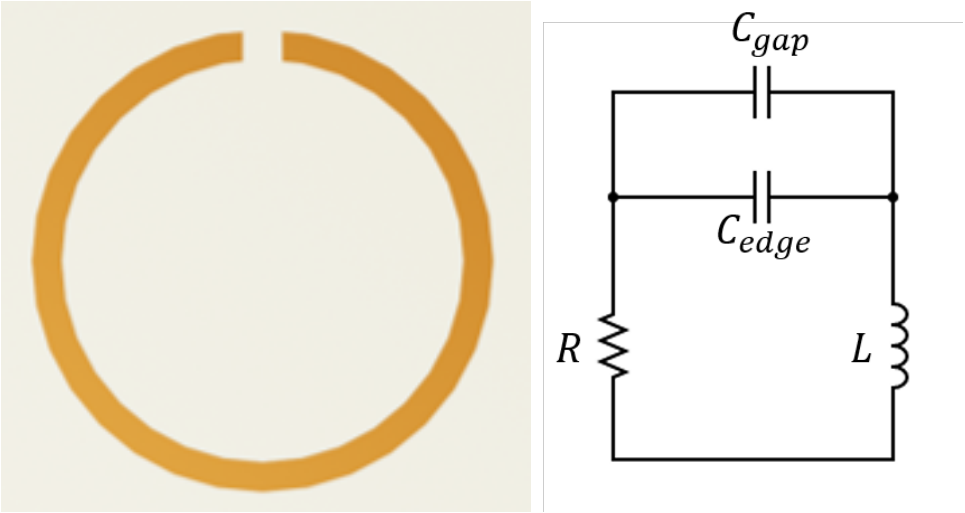

(a) (b)

Figure 3.4: a) A split-ring resonator b) The equivalent circuit of a split-ring resonator with a gap capacitance C_{gap}, an edge capacitance C_{edge} an inductance L and a resistance R.

$$C_{gap} = \epsilon\left(\frac{hw}{g}\right) + C_0 \tag{3.14}$$

In a standard capacitor the fields would be largely contained directly between the two plates making the contribution of fringing fields negligible. However, as has been discovered frequently in attempts to numerically calculate SRR resonances, the fringing fields component C_0 can cause disagreements of around 10% between final value for frequency and experiment [70, 71]. The precise form of C_0 has not yet been rigorously derived in literature but the correction used by Sydoruk *et al.*, shown in equation 3.15 offers good accuracy in this case of circular ring with a narrow wire width compared to the radius.

$$C_0 = \epsilon(h + w + g) \tag{3.15}$$

It should be noted that the value of ϵ may be different between equations 3.14 and 3.15. If a SRR is between two substrates then its fringing field will be within a high permittivity medium while its contained fields will be within air. The SRR may also not be symmetrically surrounded, for example if it was printed onto substrate on one side but open to air on the other, as those used in this thesis are. In this case C_0 could be calculated using the average of the material permittivities. This

takes into account that half of the fringing fields will be in an alternative medium to the other. This correction will only work in the case where $h << w$. Beyond this case fields fringed in the plane of the ring also become a significant consideration, so much so that they can be used for material imaging [72].

C_{edge} between two symmetrically positioned points can be found by taking the ratio of surface charge, σ, and voltage between two points, V. This can then be integrated over half of the ring to find the full edge capacitance (equation 3.16. By taking 0 radians as being the central position of the gap the integral is symmetric but cannot start at 0 since at that point there is no metal to hold a surface charge. For this reason the ring is integrated from θ_g where $\theta_g \approx \frac{g}{2R}$ in the small gap regime.

$$C_{edge} = (h + w) \int_{\theta_g}^{\pi} \frac{\sigma(\theta) R}{V(\theta)} \mathrm{d}\theta \tag{3.16}$$

The values of σ and V are obtainable entirely from the electric fields. While the SRR is generally made of very thin metal relative to its other dimensions it is still technically a split cylinder. Assuming the equations for σ and V [73] in the split cylinder geometry hold in the $h << w$ regime we can enter equations 3.17 and 3.18 into 3.16 to get the full integral 3.19,

$$\sigma = \frac{\epsilon V_0}{\pi R} \cot \frac{\theta}{2} \tag{3.17}$$

$$V = \frac{V_0}{\pi} (\pi - \theta) \tag{3.18}$$

where V_0 is the voltage across the gap of the ring.

$$C_{edge} = \epsilon (h + w) \int_{\theta_g}^{\pi} \frac{\cot \frac{\theta}{2}}{(\pi - \theta)} \mathrm{d}\theta \tag{3.19}$$

This integral, while possible to calculate, is not analytically solvable. To get an approximate analytical solution we can note that $\cot\frac{\theta}{2}$ approaches infinity as θ approaches 0 and thus that removing θ from the denominator should not significantly change our result when integrating at a very low θ_g. This change still holds at π since the integral of $\cot\theta$ at $\frac{\pi}{2}$ is 0. We can therefore approximate our edge capacitance in equation 3.20

$$C_{edge} \approx \epsilon(h+w)\int_{\theta_g}^{\pi}\frac{\cot\frac{\theta}{2}}{\pi}\mathrm{d}\theta = \frac{2\epsilon(h+w)}{\pi}\ln\frac{4R}{g} \tag{3.20}$$

3.2.2 Anisotropy and Bianisotropy

An isotropic material is one that is the same in every direction. For a resonant meta-atom, it could be considered isotropic if it's resonance could be excited by any polarisation of wave. Conversely then, an anisotropic material is one that is different in a given direction and an anisotropic meta-atom will behave differently when excited with different polarisations of light. For the example of a SRR, an exciting field of the resonance wavelength that is polarised to be orthogonal to the dipoles of the resonator will not excite a resonance whilst one parallel to at least one of the dipoles will, so a SRR is anisotropic.

Additionally, many meta-atoms exhibit bianisotropy, where the excitation of the resonator via the electric dipole causes a magnetic dipole to be excited and vice versa. In an SRR, current flow around the ring causes both dipoles and can be initiated via either of the meta-atom's dipoles, so a simple SRR is bianisotropic as well. This feature can be hugely beneficial, as it allows a metamaterial with no ferromagnetic components to interact with magnetic fields, but might need to be suppressed (as in chapters 6 and 7 of this thesis). This can be done by structurally arranging the resonator such that, at resonance, each of the dipoles of a given type that are excited cancel each other out [74]. Such a design is effectively non-bianisotropic in the far field, but is still bianisotropic in the nearfield.

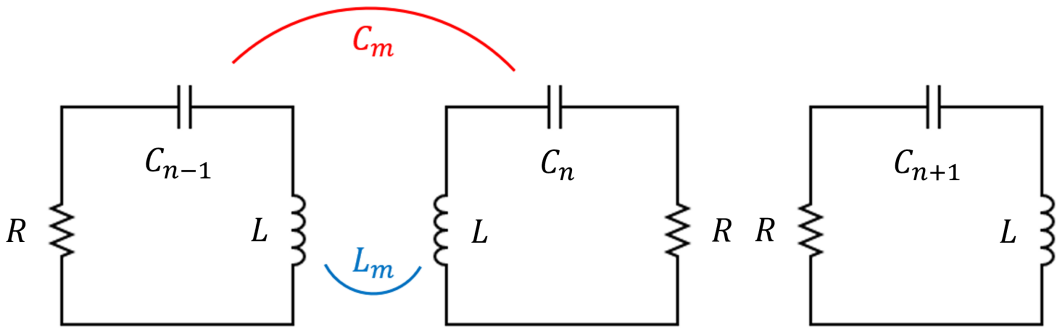

Figure 3.5: Equivalent LCR circuits of a chain of N coupled SRRs with mutual inductance L_m and capacitance C_m between each element (only marked for first two).

3.3 Electromagnetic Coupling

In section 3.1 I covered, mathematically, the effects of a coupling force between oscillators. For ease of visualisation I used the classical mass-spring image for oscillators, with the coupling force being just another spring in the system that connects the two oscillators. However, coupling in microwave metamaterials is more complex and, unfortunately, harder to directly visualise. This being the case I will present a little more discussion here. Though I will limit myself to the interactions between identical SRRs, the theory discussed here is applicable to other microwave resonators.

3.3.1 Equivalent Circuit approach

Coupling between two SRRs can be initially understood by reverting to the equivalent circuit approximation, where each resonator is represented as an LCR circuit [69, 75]. As discussed previously in section 3.2, a SRR at resonance has two dipole moments, an electric moment and a magnetic moment. We can intuitively guess therefore that it will couple to another SRR via one of those forces (as it does not come up in this thesis I will disregard the situation of two resonators in contact i.e. conductive coupling). In our equivalent circuit, then, there must be some relation between the capacitive (electric) and inductive (magnetic) elements. Figure 3.5 shows the equivalent circuits for coupled SRRs, each with an uncoupled resonance of $\omega_0 n^2 = \frac{1}{LC_n}$, coupled to each other with interactions indicated as the mutual

inductance, L_m, and mutual capacitance,C_m, of the coupled circuit. These mutual values represent the fact that an alternating voltage, in the case of C_m, or current, for L_m, in one will induce a proportional voltage in the other. Mutual values in a coupled system with only one source of coupling, either C_m or L_m, can be calculated by exciting one element (1) and monitoring the current (J) and voltage (V) of the unexcited element (2).

$$C_m = \frac{J_2}{dV_1/dt} \tag{3.21}$$

$$L_m = \frac{V_2}{dJ_1/dt} \tag{3.22}$$

Our goal here, however, is to find K_E, K_H or, in the case of system that is capacitively and inductively coupled, the total coupling K_T ($K_T = K_H - K_E$) the magnetic and electric coupling terms respectively; they are the direct analogue between the Electromagnetic and Newtonian coupling cases. First, in the circuit shown in Figure 3.5, let us set $C_n = C_{n+1} = C$ and find the coupling from the wave propagation. We can represent this relationship mathematically by using Kirchhoff's voltage law, that the voltage over all components in a closed circuit loop must be equal to the source voltage for that loop, as in equation 3.23:

$$J_n(i\omega L + R - i\frac{1}{\omega C} + (J_{n+1} + J_{n-1})(i\omega L_m - i\frac{1}{\omega C_m}) = 0 \tag{3.23}$$

where J_n is the current in resonator n and ω is the coupled mode frequency. Shamonina [16] found the dispersion relation (see section 4.4.2 for details on how dispersion relationships are used) of such a chain to be:

$$K_T\cos(ka) = 1 - \frac{\omega_0^2}{\omega^2} - \frac{iR}{\omega L} \tag{3.24}$$

where k is the wavevector of the propagating wave and a is the spacing between resonators. By choosing a harmonic solution for current of $J_n = J_0 e^{i\omega t} e^{ika}$ and factoring into equation 3.23 we find it can be rearranged into equation 3.25:

$$(\frac{2L_m}{L} - \frac{\omega_0^2 C}{\omega^2 C_m}) \cos(ka) = 1 - \frac{\omega_0^2}{\omega^2} - \frac{R}{i\omega L} \tag{3.25}$$

and by comparing equations 3.24 and 3.25 we can extract our values for coupling terms:

$$K_E = \frac{\omega_0^2}{\omega^2} \frac{2C}{C_m} \tag{3.26}$$

$$K_H = \frac{2L_m}{L} \tag{3.27}$$

$$K_{total} = K_H - K_E \tag{3.28}$$

Both of the coupling terms can be complex, if there is retardation between the elements, and negative, depending on the relative orientations of the elements and whether their mutual interactions induce opposing or complementary fields. This allows for the possibility of opposing coupling terms, which is explored more thoroughly in chapter 5. Also of note is the frequency dependence of electrical coupling; coupling decreases with rising frequency. This is often ignored in the narrow-band approximation where it is assumed that $\omega_0 \approx \omega$.

Unfortunately, equations 3.21 and 3.22 are only applicable in isolation. When a system with both magnetic and electric coupling is examined, only the total coupling can be derived rather than the individual electric and magnetic contributions, at least for identical resonators. Chapter 5 shows how the introduction of a tunable dependence to the coupling terms allows the individual coupling terms to be extracted from frequency data.

3.3.2 Dipole Interaction

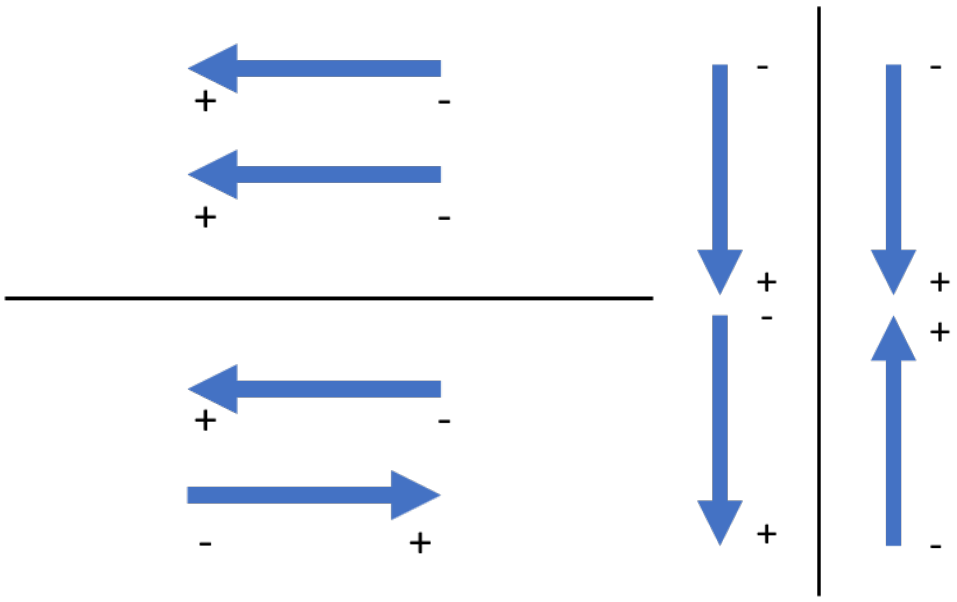

Figure 3.6: Schematics for the relative arrangements and orientations of transversely (a) and longitudinally (b) coupled dipoles. In (a) the symmetric case puts the two positively charged ends of the dipole in proximity, making in the higher energy orientation to when the dipoles are anti-aligned. In (b), conversely, the anti-aligned state is higher energy than the aligned state.

The inductive and capacitive parts of the SRR each create a respective magnetic and electric dipole moment. The relative orientation and position of these dipoles determines much of the coupling dynamics between two SRRs. Figure 3.6 shows 2 possible dipole arrangements, transversely in Fig 3.6a and longitudinally in Fig 3.6b. Each arrangement also has a high and low energy solution in which the two dipoles can be oriented, with two alike ends in proximity being the high energy orientation and vice versa. While, of course, any arbitrary orientation of the dipoles is possible, we would only need consider those components that were parallel when considering how they might interact. If two dipoles were represented as vectors $\vec{d_1}$ and $\vec{d_2}$ with the unit vector $\hat{r}$ being the direction between them, then their interaction would be proportional to an orientational factor, Γ_θ, given by equation 3.29.

$$\Gamma_\theta = 3(\vec{d_1} \cdot \hat{r})(\vec{d_2} \cdot \hat{r}) - \vec{d_1} \cdot \vec{d_2} \tag{3.29}$$

The sign chosen is here is chosen by convention. The transverse arrangement ($\vec{d_1} \cdot \hat{r} = \vec{d_2} \cdot \hat{r} = 0$) of dipoles in Fig 3.6a is said to provide negative coupling, as its lowest energy orientation is the asymmetric case, and the longitudinal arrangement ($\vec{d_1} \cdot \hat{r} = |\vec{d_1}|$ and $\vec{d_2} \cdot \hat{r} = |\vec{d_2}|$) a positive coupling term. Of particular interest in SRRs is that, when coupled axially, their bianisotropic nature means that the electric dipoles will couple negatively whilst the magnetic dipoles couple positively. This can lead to a value of $K_{total} = 0$ when the two individual coupling terms are equal and opposite even if they are themselves large, as is the case in chapter 5.4.

3.3.3 Field Interaction

While the dipole moments are often depicted as two arrows, going across and through the plane of the SRR respectively, this is a convenient fancy. In actuality, a SRR is surrounded by a web of vector fields, decreasing in intensity as they radiate out. Where this web is strongest for each field, and the direction it has greatest magnitude, determines where the dipole moment arrow is drawn. These fields can be used to determine how efficiently two resonators will couple by examining the field overlap [76]:

$$K_E = \frac{\int\int\int E_1 \cdot E_2 \mathrm{d}V}{\sqrt{\int\int\int |E_1|^2 \mathrm{d}V \times \int\int\int |E_2|^2 \mathrm{d}V}} \tag{3.30}$$

where O is the overlap integral, E_n is a vector field (magnetic or electric) of element n (n=1,2) and dV is an element of volume. This value determines how efficiently two resonators will couple together. It will be 0, no coupling, in cases where the fields are orthogonal to each other or when they are too far apart and there is no overlap. Unfortunately, this is not an overly useful equation, requiring as it does the full calculation of both fields. A more direct approach is to consider only the mutual energy exchanged between resonators. The mutual magnetic energy (W_H) between two SRRs is the extra field energy stored between the resonators as a result of their coupling. It is given by:

$$W_H = \frac{1}{2}\int (\vec{A_1}\cdot\vec{J_2} + \vec{A_2}\cdot\vec{J_1})dV \tag{3.31}$$

where $\vec{A_n}$ is the magnetic vector potential, $\vec{J_n}$ is the current. As $\vec{A_n}$ is dependent on $\vec{J_n}$, as per equation 3.32, and $\int \vec{A_1}\cdot\vec{J_2}dV = \int \vec{A_2}\cdot\vec{J_1}dV$, then mutual magnetic energy can be represented by the double integral 3.33.

$$\vec{A}(\vec{r}) = \frac{\mu_0}{4\pi}\int \frac{\vec{J}(\vec{r'})}{|\vec{r}-\vec{r'}|}dV' \tag{3.32}$$

$$W_H = \frac{\mu_0}{4\pi}\int\int \frac{\vec{J_1}(\vec{r_1})\cdot\vec{J_2}(\vec{r_2})}{|\vec{r_1}-\vec{r_2}|}dV_1dV_2 \tag{3.33}$$

where $\vec{r}$ is the position vector, $\vec{r_n}$ is a point on ring n and V_n is the volume of element n. A further simplification can be found if the rings are suitably thin, such that the current doesn't vary significantly across its width, as they can then be treated as a filament and the integral in 3.33 need only be performed over the line elements of s_n, which is the line along the circumference of element n. This allows the mutual energy to be considered by measuring only the distance between, and current at, points along the circumference of the resonators. To find the mutual electric energy, W_E, we need only draw an equivalency between charge line density, ρ_n, with current and the scalar potential with vector potential to get equation 3.34.

$$W_E = \frac{1}{4\pi\epsilon_0}\int\int \frac{\rho_1(\vec{r_1})\rho_2(\vec{r_2})}{|\vec{r_1}-\vec{r_2}|}dl_1dl_2 \tag{3.34}$$

We can see from the equation 3.33 that orthogonal currents, where $\vec{J_1}(\vec{r_1})\cdot\vec{J_2}(\vec{r_2}) = 0$, will not interact, and also that the mutual energy might be negative between two parts of the SRRs with oppositely flowing currents, which matches with the more rudimentary analysis allowed by examining their dipole moments. The coupling terms from the circuit analysis can even be found through the following equations:

$$K_H = \frac{W_H}{I_1 I_2} \tag{3.35}$$

$$K_E = \frac{W_E}{Q_1 Q_2} \tag{3.36}$$

where I_n is the total current and Q_n is the charge on half the ring (total charge would be 0).

3.4 Molecular Aggregates

In this section I will detail those elements of theory relating to molecular aggregates that will be important in my efforts to analogously replicate them with metamaterials. Of noticeable omission is my lack of discussion on vibrational modes and phonons. It is not beyond the scope of metamaterials to replicate these features, or indeed to couple into them from microwave excitation [77], but as the focus of this thesis is microwave metamaterials I will disregard them for now. If a reader would like to learn more about the current state of vibrational coupling research I recommend [55].

3.4.1 J and H aggregates

When a dye molecule aggregates it forms chains of molecules that couple to each other in a dipole-dipole manner [78]. The optical properties of the two common types of molecular aggregates, known as J- and H-aggregates [79], are shown in figure 3.7. Interaction energies between the electric dipole moments associated with excitonic transitions in neighbouring dye/pigment molecules in an aggregate depend on the relative orientation of the dipole moments, see panels (a), (b), (d), (e) in figure 3.7. The dispersion of the allowed states of chains of dipoles are shown in panels (c) and (f). Also shown, in panel (g), are absorption spectra of a well-studied dye molecule, TDBC (5,5',6,6'-tetrachloro-1,1'-diethyl-3,3'-di(4- sulfobutyl)-benzimidazole carbocyanine) [80]. In methanol TDBC exists as a monomer (blue curve); however in water the TDBC molecules aggregate to form linear chains that

display J-aggregation behaviour, there is a dramatic red-shift and sharpening of the absorption (red curve). In J-aggregates the molecular dipole moments are coupled longitudinally, in H-aggregates the coupling is transverse. The changes brought about by aggregation can be dramatic, sufficient to produce a negative real part of the permittivity, allowing aggregated films to support surface waves similar to those found in plasmonic materials [81–84].

Looking at panel (f) one might expect a continuum of features to be seen in the absorption of J-aggregates for different combinations of dipole orientations, rather than just one, as seen for TDBC in panel (g). However, for J-aggregates only the lowest energy state has a significantly non-zero net dipole moment and it is only this state that is visible (bright), the other states have by comparison very small dipole moments and are not seen in far-field spectroscopy, they are dark. For H-aggregates the situation is reversed and it is the upper state that is bright, i.e. only this state has a significantly non-zero net dipole moment. The remaining modes make up a the so called 'dark' states, which do not absorb radiation but are by no means a forbidden arrangement for the aggregate dipoles. Their presence has significant implications for the aggregates behaviour, but they are not directly probeable by their very nature [85].

3.4.2 Quasi-Particles

Quasi-particles may well be the most important things to never exist. When a system reacts to a phenomenon like plasmonic or vibrational oscillations as if it was reacting to a particle, those non-particle elements can be mathematically and conceptually compressed into an effective particle, known as a quasi-particle. For the two oscillations I just mentioned, their respective quasi-particles are plasmons and phonons. As in many areas of condensed matter physics quasi-particles play a key role in understanding molecular aggregates. Here I will detail the ones important to this thesis, which is far from an exhaustive list.

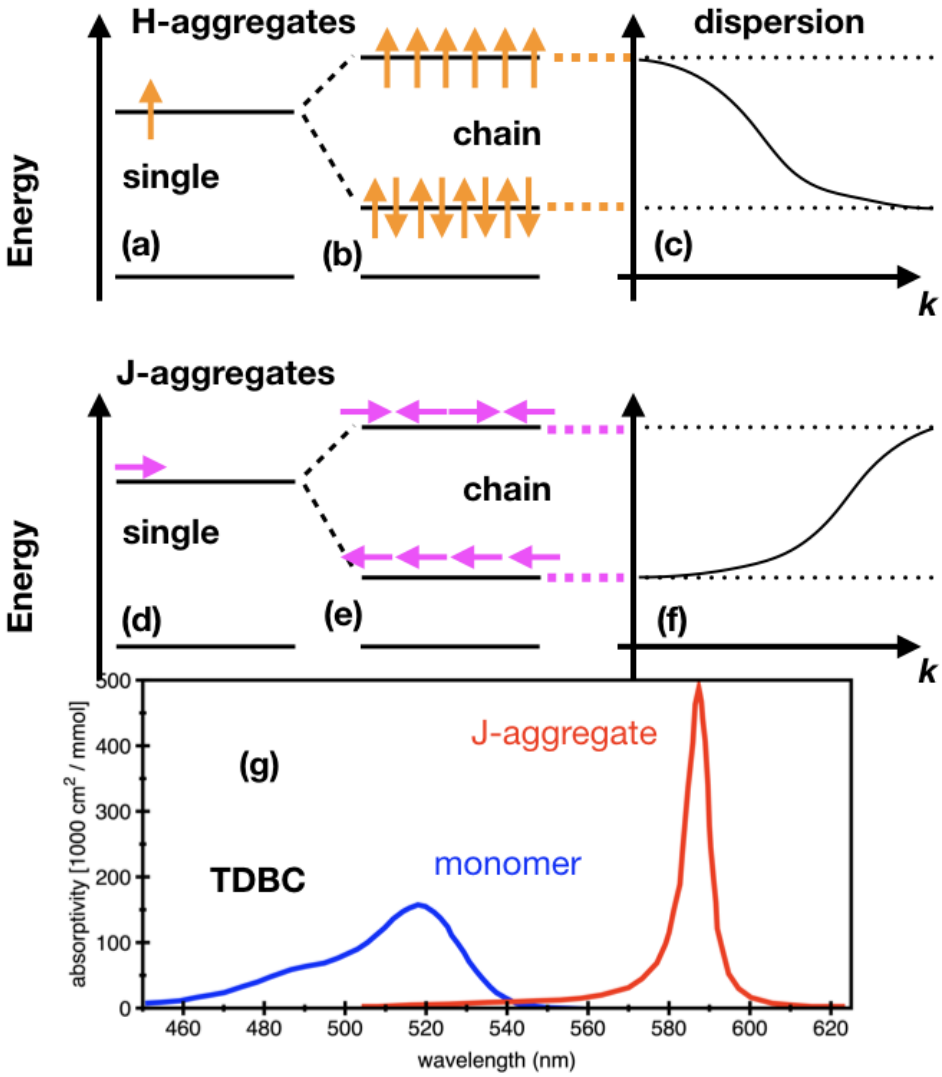

Figure 3.7: Two types of aggregate may be distinguished by the nature of the coupling between the individual molecular dipole moments. Panels (b) and (e) show the configurations and relative energies of H- and J-aggregates respectively. H-aggregates (a-c) involve transverse coupling, the highest energy state occurs when all N molecules have their dipole moments aligned, this corresponds to a zero wavenumber state; the highest wavenumber state occurs when adjacent molecules are anti-aligned, panel (c). J-aggregates (d-f) involve longitudinal coupling. The highest energy state occurs when all N molecules have their dipole moments anti-aligned, this corresponds to the highest wavenumber state; the zero wavenumber state occurs when adjacent molecules are all aligned, panel (f). Panel (g) shows the absorption spectra for TDBC dye molecules in two solutions. In methanol (blue curve) the molecules are in the monomer form, and the absorption peak occurs at $\sim 520\ nm$. In water the molecules behave very differently and form J-aggregates, the absorption peak red-shifts, occurring at $\sim 585\ nm$. Panel (g) is adapted from [80].

Excitons

An exciton is a current-less electron excitation that acts in a particle-like manner. When an electron is suitably excited it may jump across a bandgap in its material, leaving behind a vacancy with a positive charge called a hole. This electron-hole pair can transport energy through a solid via the de-localised electron without a corresponding movement of charge and for this reason play an important role in many natural processes. Their are a few different types of exciton but the only one relevant to this thesis is the Frenkel exciton, distinguished as an exciton where both the electron and the hole remain on the same molecule due to strong interactions between them and thus do not change that molecule's charge. The Frenkel exciton is best used to model the actions of electron-hole pairs in organic systems like J-aggregates [86], hence its value here, and can be conceptualised as an excitation moving from site to site on a molecule [87].

As the exciton has a positive and negative element, from its electron-hole pair, it has a corresponding electric transition dipole, and as a result two molecules with Frenkel excitons will couple together in a dipole-dipole manner that can be entirely calculated using the same methods as discussed for coupled oscillators in section 3.1 earlier in this chapter [88]. The same applies for linear chains of excitons. This is a critical observation for the meta-analogue approach presented here.

Solitons

A soliton, or solitary wave, is a wave packet that maintains its shape in translation. A relatively poorly defined quasi-particle (not all things called a soliton have all the following features), the soliton has the features of being constant in form, localised within a region, and able to interact with other solitons that leaves both unchanged after the collision beyond a phase shift. Solitons' consistency make them attractive for long distance energy transference applications [89], and indeed they play an important role in some organic phenomena [90].

Polaritons

The polariton could be fancifully considered a quasi-particle squared, as it describes the resulting modes that form between an excitation, a quasi-particle itself, and electromagnetic radiation [91] (photons). Of interest to this thesis is the exciton-polariton where the excitation in question is itself of exciton character. From this interaction there are two polaritons, the upper and lower branches of the level repulsion, where the character of each is determined by the photon and Exciton oscillations being in phase or anti-phase respectively.

Polaritons are of particular interest because they inherit properties from both of their parent resonators. For example a polariton has a small effective mass inherited from the photon component which allows it to form a Bose-Einstein condensate at room temperature [92, 93]. Exciton-polaritons do not form in every system where excitons can couple with radiation. For the formation of a polariton the system must be in what is known as the strong coupling regime.

3.4.3 Strong Coupling

When two oscillators couple together they exchange energy with each other. At the same time, if they have lossy elements, they will also be losing energy via those loss processes. In a system with a high degree of loss relative to the interaction energy of the resonators, a packet of energy will most likely be lost before it is exchanged (when all energy is lost before any can be exchanged, the elements aren't coupled at all). In this regime, the weak coupling regime, there will be a slight level repulsion between the coupled resonators but this will be smaller than the width of the modes themselves. If each of the resonators are of a fundamentally different character, as is the case with the light-matter interaction, the lack of consistent exchange will mean that neither mode is significantly altered from its uncoupled character.

In the strong coupling regime the interaction energy is much greater than the loss vectors of the system and a single energy packet will often be exchanged back and forth multiple times, imparting the character of each onto the other [94]. Figure 3.8 shows the absorption of two coupled systems with the same interaction energies but

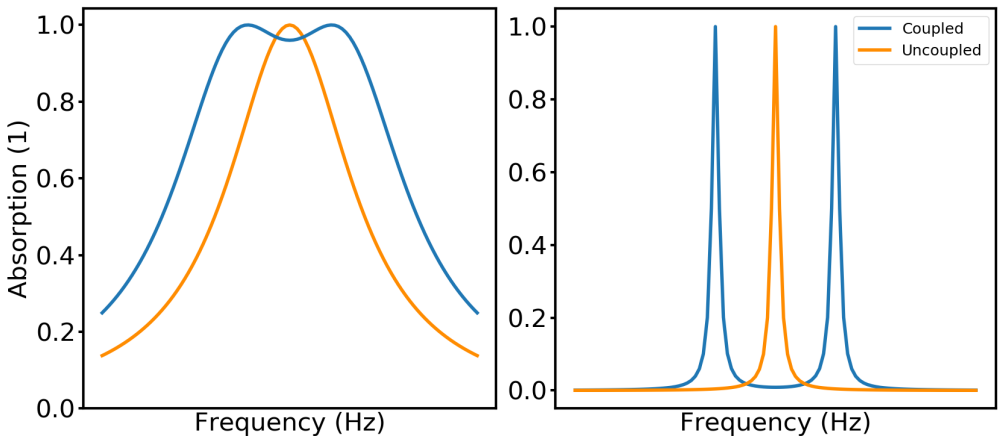

(a) (b)

Figure 3.8: Plots of simulated absorption (normalised to the max absorption) of two identical resonators when they are uncoupled (orange) and coupled (blue) in the a) weak and b) strong coupling regimes. The system is transitioned from the weak to the strong coupling regime by reducing the loss of the resonators and thus narrowing their absorption peaks.

differing degrees of loss. In Figure 3.8a the repulsion is not enough to overcome the loss vectors; the two absorption peaks are nearly indistinguishable and it is in the weak coupling regime. By contrast Figure 3.8b shows the same system where the loss vectors have been reduced. Each peak is clearly distinguishable and we are in the strong coupling regime despite the fact that we have, perhaps counter intuitively, not increased the coupling strength (mode splitting) between the resonators.

Chapter 4

Methods

4.1 Introduction

This chapter will present the various methodologies used to collect and analyse the data presented in later chapters. It will start by outlining the fabrication procedures used to create samples, followed by a description of how the data was collected and end with the analysis and modelling techniques that have been applied. This chapter will cover the broad techniques applied throughout this thesis. Where a method is specific to a single chapter the details of that method will be included within that chapter, rather than here. Additionally, the specific applications of the following techniques will also be covered in more detail within their relevant chapters.

4.2 Fabrication

4.2.1 Laser Lithography

Lithography, literally "stone writing" in the original Greek, refers to a printing process in which a negative of the design in question is used to recreate the original. In laser lithography, a laser on an XYZ motorised stage is loaded with the coordinates for a design, or the negative thereof depending on the technique. By exposing those coordinates to the beam, the original design will remain. Another common lithography technique is to use a stencil and expose a sample all at once. This

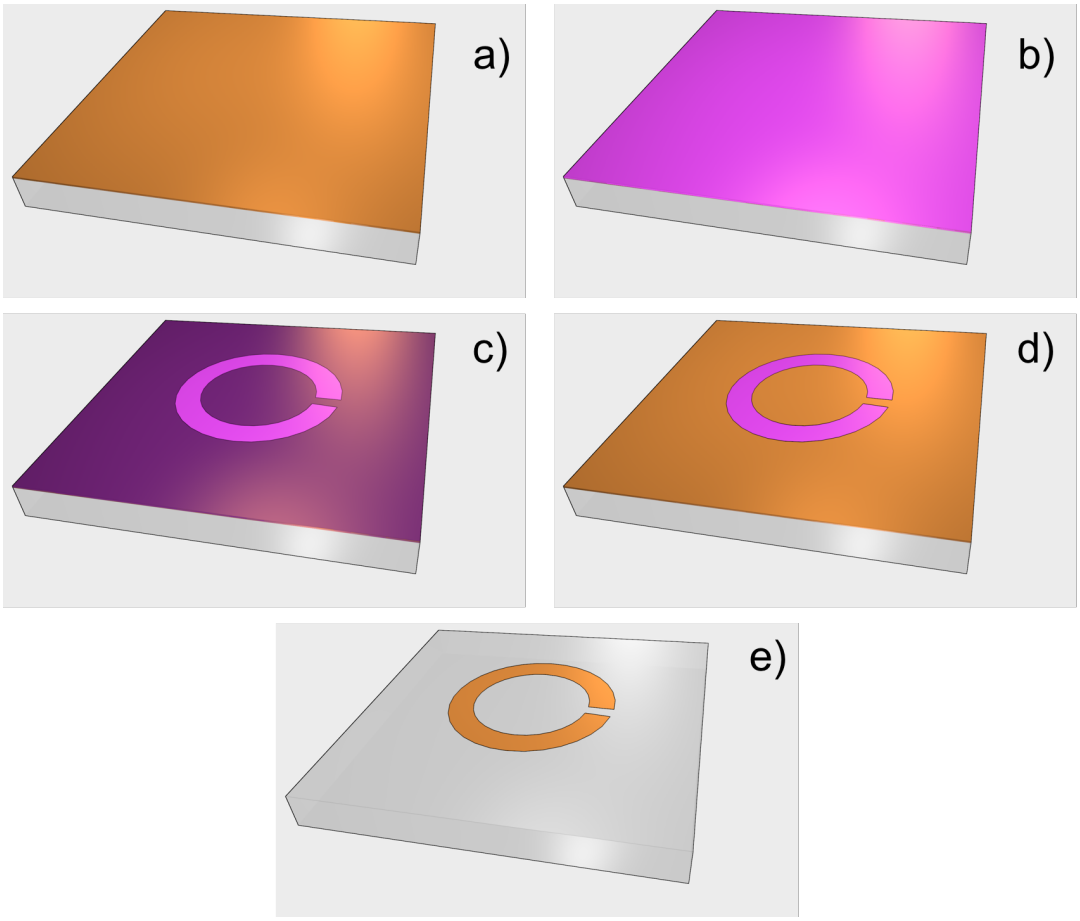

Figure 4.1: The steps involved in creating a planar metallic structure using wet etching and laser lithography techniques. First, a blank of copper and substrate (a) is coated in a layer of photoresist (b). The photoresist is then exposed to a laser which draws a negative of the design (c). The exposed photoresist is removed using a developing fluid leaving behind the design on the copper (d). Finally, the sample is immersed in ferric chloride to etch away all the exposed copper. After cleaning the design in copper remains on the substrate (e).

technique excels when multiple samples with the same design are required, but is not worth the additional hassle of creating a mask when each sample is intended to be unique.

4.2.2 Wet Etching

All the samples presented in this thesis were created, if not in part then in their entirety, using the wet etching technique. Wet etching is ideal for creating planar structures and is used widely in the industrial manufacture of printed circuit boards. In order to make use of the improved accuracy provided by industrial methods the samples used in chapters 6, 7 and 8 were all created by commercial PCB manu-

facturers. The precise details of their techniques are unknown beyond that they used a wet etch method. This section will cover the methodology used to create the samples in chapter 5.

Wet etching refers to the practice of using a corrosive chemical, such as Ferric chloride which rapidly dissolves copper, to remove unwanted material from a sample. In most cases, a design should remain after etching; some form of protective layer is required to preserve some of the material. This protective layer is referred to as a resist. In this case, a light-sensitive photoresist was used.

Starting with a copper blank consisting of 30 μm thick copper on a 1.55 mm thick substrate, a layer of photoresist was applied evenly over the whole sample. This photoresist was then exposed, using the laser lithography technique described in section 4.2.1, which applied a negative of the desired design onto the sample. When exposed to the ultra-violet light of the laser, photoresist becomes soluble in developing fluid. A one minute soak in this chemical removes all exposed photoresist and leaves behind the intended design printed in resist on top of the copper. This prepared sample can then immersed in Ferric Chloride for an amount of time dependent on the amount of copper that needs to be removed. The Ferric Chloride will dissolve all the copper not protected by the remaining resist, etching the design into the metal, and leaving behind a finished sample. A graphic presentation of the above process can be seen in Figure 4.1

Whilst versatile and cheap, in a laboratory setting wet etching suffers from inconsistency due to the moderately unpredictable nature of the chemical etchants used. It is not cost effective to discard etchant after only a single use, nor to precisely control the temperature of an open bath, when working at such small scales. The two primary sources of error are referred to as under and over-etching. Each describes a case where the time a sample needs to spend in etchant has been miscalculated. While generally tiny, about 10-20 microns on a 6 mm diameter sample, they still must be taken into account when considering inconsistencies between modelled and measured results. Examples of over and under-etching are shown in Figure 4.2.

Figure 4.2: Examples of over (a) and under (b) etching errors from a side-on perspective. In both cases the sample has been left in the etchant for an improper amount of time, leaving behind too much or too little copper. Whilst generally small, some designs with low ratios of copper to empty space can fail completely as sections near the edge of the design begin to over-etch and sections near the middle remain under etched.

4.3 Experimental Methods

4.3.1 Vector Network Analysler

The primary experimental tool used in this thesis is the Vector Network Analyser (VNA). It is a highly versatile device used in the field of RF research, able to rapidly characterise the amplitude and phase of a system's wave parameters from kHz up to high GHz frequencies. A VNA can have several ports, and the amount used in a single measurement depends on the requirements of a study.

The purest form of study would be an analysis of a single port network. Take, for example, an unknown component attached to a single port of the VNA by a 50 Ω impedance coaxial cable. In this case, there will be two waves: the incident wave (i) and the reflected wave (r). The values of i and r are what are known as the system's wave quantities with units of $\sqrt{Watts}$.

The system will also have a reflection coefficient R which is given by equation 4.1.

$$R = \frac{r}{i} \tag{4.1}$$

R will be a complex quantity that will depend on the complex impedance of the system's unknown component (Z). R contains information on both the amplitude and phase difference in its modulus and exponential argument, respectively. We can use our measured value of R to calculate Z.

$$R = \frac{z-1}{z+1} \tag{4.2}$$

where z is the normalised impedance, $z = \frac{Z}{Z_0}$, and Z_0 is the impedance of the 50 Ω coaxial line. A setup like this would allow us to test the impedance of a resistor, for example. It should also be noted that if the component is known, then a single port arrangement like this can be used to characterise the transmission properties of the 50 Ω coaxial line as part of a pre-measurement calibration.

In a two-port measurement there are now two ports that can both transmit and receive into and out of the system under test, resulting in wave quantities of i_1, r_1, i_2 and r_2. Along with there now being two reflection coefficients, R_1 and R_2 there will now also be two transmission coefficients, the transmission from port 1 to port 2, T_1, and the transmission for port 2 to port 1, T_2. These are commonly known as the system's scattering, or S, parameters and can be written as a matrix:

$$\begin{bmatrix} R_1 & T_2 \\ \\ T_1 & R_2 \end{bmatrix} = \begin{bmatrix} S_{11} & S_{12} \\ \\ S_{21} & S_{22} \end{bmatrix} \tag{4.3}$$

By measuring these S parameters at different frequencies, we can build a data set that shows the frequency dependent response of our system.

In order for this data to give usable results, a calibration procedure must be performed to remove artefacts from the measured data due to impedance mismatches within the cables and adapters required to connect VNA and sample. An understanding of the process by which a VNA can rapidly characterise a system at frequencies in the RF range is valuable for correctly choosing a calibration method for the system in question. Additionally, the measurement technique used will determine which calibration types are preferable and/or possible.

While the generation of high frequency waves is relatively simple, the direct measurement of the relative amplitude and phases requires a more complex method within the VNA; the use a frequency mixer. The frequency mixer accepts two signals, x_1 and x_2, as inputs and produces a single signal as its output that is a combination

of the original set, called X. X has a lower frequency component, $f_1 - f_2$, and a higher frequency component, $f_1 + f_2$. The form of these signals is given in equations 4.4 and 4.5.

$$\begin{aligned} x_1 &= A_1 \cos(2\pi f_1 t) \\ x_2 &= A_2 \cos(2\pi f_2 t) \end{aligned} \tag{4.4}$$

$$X = \frac{1}{2} A_1 A_2 \big(\cos(2\pi(f_1 - f_2)t) + \cos(2\pi(f_1 + f_2)t) \big) \tag{4.5}$$

In a VNA, f_1 will be a fixed frequency given by a local oscillator and f_2 will be the variable component such that $f_1 + f_2$ is the frequency desired to probe the network. Using a high pass filter on signal X ensures only the high-frequency components will be sent out of the relevant port and, in the case of a two-port test, return through both the receiving and exciting ports modulated in some way by the tested system. The modulated returning signal, X_R, is then remixed with x_2 to produce a new signal that has the same frequency as x_1 but contains information about the phase and amplitude modulations caused by the system under test. This signal is called X_{mod} and has the form given in equation 4.6.

$$X_{mod}(t) = A_{mod} \cos(2\pi f_1 t + \phi_{mod}) \tag{4.6}$$

Finally the signal X_{mod} is mixed with x_1 and a 90° phase shifted form of x_1 to produce two signals, X_{re} and X_{im} respectively, given in equation 4.7.

$$\begin{aligned} X_{re} &= \frac{1}{2} A_{mod} A_1 (\cos(\phi_{mod}) + \cos(4\pi f_1 t + \phi_{mod})) \\ X_{im} &= \frac{1}{2} A_{mod} A_1 (\sin(\phi_{mod}) - \sin(4\pi f_1 t + \phi_{mod})) \end{aligned} \tag{4.7}$$

Applying a low pass filter to these two signals removes the high frequency $f \neq 0$ components, producing two DC signals from X_{re} and X_{im} called the in-phase and quadrature components respectively.

The amplitude and phase changes caused by the tested system's modulation can then be extracted using the known value of A_1 as a normalising factor. Calibrating for this process requires the setting of reference planes before which modulations

are compensated for and ignored from the final data set. As mentioned previously, this is done using devices with known properties. The calibration used in chapter 5 was the SOLT method. In the SOLT technique, three types of cable termination are used at the reference plane of the experiment. The Short and Open terminations will reflect the entire signal but with different phase changes at the termination. A phase change of the voltage wave by 180° due to 0 impedance at a short termination and 0° due to infinite impedance at an open termination. The Load termination reflects nothing by attaching a load that matches the impedance of the cable being tested. Finally, the Through calibration is perfectly transmissive and is achieved by attaching the two cables together at their reference plane. Deviations from perfect reflection, absorption and transmission are recorded during the calibration and compensated for in the experiment.

4.3.2 Near-field measurements

In chapters 6 and 7 1D resonant metamaterial chains are used to replicate molecular aggregates. In order to map the dispersive properties of the chains, it is necessary to probe each individual meta-molecule's fields.

One of the defining features of metamaterials is that they operate at a scale far smaller than the wavelengths that excite them. This sub-wavelength property inevitably leads to a great deal of field confinement in operating metamaterials. The precise locations and effects of these confinements can be almost impossible to discern from a metamaterial's far-field radiation. For example, the case of non-bianisotropy described in section 3.2 requires that electric dipoles caused by field confinement in the splits be cancelled out in the far field. The nature of this interaction would be hidden without near-field probing.

Two antennas were used in this thesis, one acting as a launch antenna that excites modes at the end of the chain and the other as the probe antenna which is scanned along the length of the chain using an XYZ motorised stage. In order to minimise the direct radiative transmission between antennas, they are designed to have different operating frequencies. The probe measures how much signal it is

receiving from the launch antenna and provides a spatial field map of the modes that are supported by the chain. Applying a Fourier transform to this data, explained in section 4.4.2, reveals the velocities and propagation directions of modes in the system.

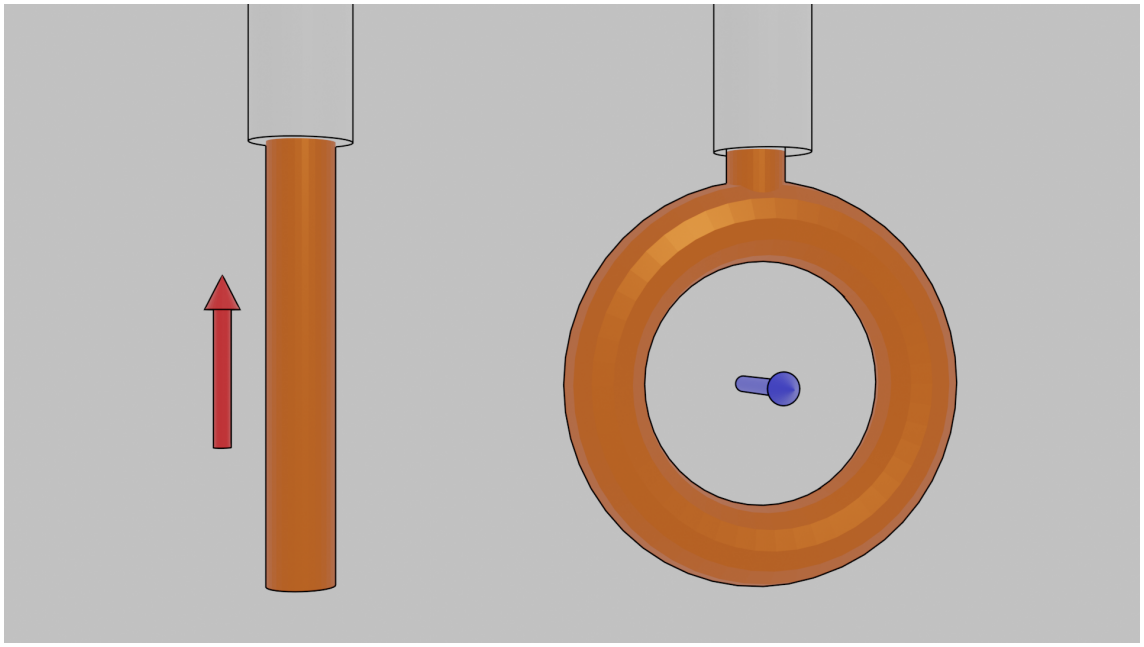

Figure 4.3: A magnetic loop antenna with the orientation of its magnetic dipole (blue) labeled and an electric rod antenna with the orientation of is electric (red) dipole.

One of the primary issues with near-field measurements is the influence of the probe used. For all the near-field results presented in this thesis, either a magnetic loop antenna or an electric rod antenna was used, pictured in Figure 4.3. Each antenna generates a magnetic or electric dipole respectively, which can excite resonances within samples. These antennas are designed with two factors in mind: the antenna's resonance relative to the sample's, and the amount of metal in the antenna. Perhaps counter intuitively, a near field antenna should have a resonant frequency which is a great spectral distance away from the resonance of the sample it is to measure. By design, antennas couple well to metamaterials and if the resonance frequency of the antenna is close to that of a mode supported by the metamaterial, there would be spectral repulsion, a coupling phenomenon explained further in section 3.1.

Even when designed to resonate significantly beyond the spectral range of interest, it is also important that an antenna minimises the amount of metallic material used. An 'antenna' made of an infinite sheet of metal would have a low resonant frequency but would still undoubtedly perturb the resonances of any system in its proximity. The antennas used in this thesis are thus designed to be physically small, with lowest order resonances between 30 and 50 GHz, approximately an order of magnitude higher than the resonance frequencies of the system being probed, depending on the sample being measured.

4.4 Analysis

4.4.1 Finite Element Modelling

In all chapters of this thesis, the data presented is supported by the results from computational models. These modelled results were collected from a software package called COMSOL Multiphysics that uses a technique called finite element modelling (FEM) to accurately and rapidly calculate the behaviours of complex systems. It can be used to examine interactions too confined to be probed experimentally as well as for rapid and inexpensive prototyping of designs before manufacture.

The FEM method works by taking a system and breaking it up into spatial elements, then solves the relevant physical equations for the system at the boundaries between these elements. As an example of how it works, a simple one-dimensional electromagnetic system will be presented and solved using the FEM technique, see figure 4.4 for graphics of each of the steps. The electric field in this system fluctuates along its length, which is the final solution that needs to be calculated from boundary conditions and material properties alone.

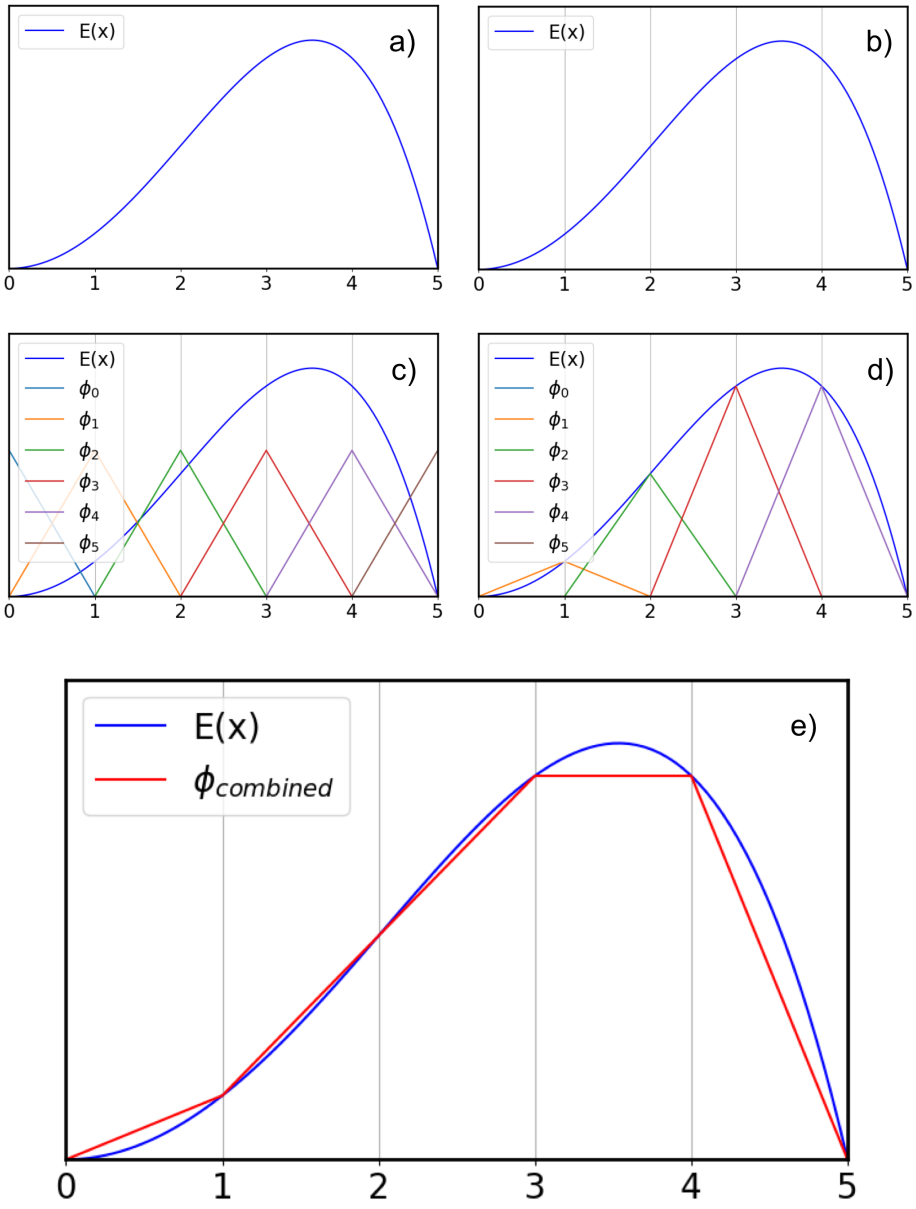

Figure 4.4: The process of approximating a real system's electric fields, E(x), using the finite element method: a) The system to be modelled. b) Break the system into mesh elements. c) Add shape functions ϕ_n within those elements. d) Applying the physical laws of the system found the values of E(x) at the mesh element boundaries and adjust the shape elements with suitable coefficients so as to match at the boundaries. e) The real full system has been closely approximated from just fitting 6 points by summing fitted shape functions. This approximation can be further improved by using quadratic shape functions as COMSOL does in its full calculations

Using both Gauss's law and the laws of energy conservation for the electrostatic case (current is 0), it can be stated that, in a case where there is no external source of energy, the following two equations will apply:

$$\frac{\partial E(x)}{\partial x} = \frac{\rho(x)}{\epsilon_0} \tag{4.8}$$

$$\frac{\partial \rho(x)}{\partial x} = 0 \tag{4.9}$$

These are the two equations that must be solved in order to find the system's field profile. Unfortunately, in real systems with hard boundaries $\rho(x)$ will be discontinuous, which will cause computation problems when trying to solve a second-order derivative. This problem can be avoided by using what is known as the "weak formulation".

In the weak formulation differential problems are solved by converting them into lower order integral problems, so equation 4.9 becomes the following integral:

$$\int_0^5 \partial_x \rho(x) \mathrm{d}x = 0 \tag{4.10}$$

The addition of an arbitrary test function, $T(x)$ that is 0 across most of x allows for integration by parts to reduce the differential order of the equation:

$$\int_0^5 \partial_x \rho(x) T(x) \mathrm{d}x = \rho(0)T(0) - \rho(5)T(5) - \int_0^5 \rho(x) \partial_x T(x) \mathrm{d}x = 0 \tag{4.11}$$

The charge density of the system is unknown, but it is only necessary to know the charge density at the system's extreme edges. The application of boundary conditions fixes the charge density at a certain value. By applying the simplest case of natural boundary conditions $\rho(0) = \rho(5) = 0$. For more complex boundary conditions where energy enters and leaves the system, boundaries called Ports are included. These are covered later in the chapter.

This equation can now be solved by dividing the system into a number of mesh

elements. The more mesh elements used, the greater the accuracy of the model, but also more computing power is required. For this case, the system can be easily divided into five elements. Each of these elements contains two shape functions, which can be reduced to six shape functions, $\phi_n(x)$, when it is assumed that the fields will be continuous over element boundaries. Any function can be approximated by a linear combination of shape functions with coefficients a_n, so it is assumed that the final solution of E can be represented as:

$$E(x) = \phi_1(x)a_1 + \phi_2(x)a_2 + ... + \phi_6(x)a_6 \tag{4.12}$$

Equation 4.12 can be factored back into the weak form, equation 4.11, to give equation 4.13 with the shape function coefficients as the six unknowns, or six degrees of freedom in COMSOL's terminology, which can be solved using six simultaneous equations.

$$a_1 \int_0^5 \partial_x \phi_1(x) \partial_x T(x) \mathrm{d}x + ... + a_6 \int_0^5 \partial_x \phi_6(x) \partial_x T(x) \mathrm{d}x = 0 \tag{4.13}$$

These equations come from each using six different substitutions for the shape function $T(x)$. These substitutions can be chosen in such a way to make all but a few parts of 4.13 0 by using the fact that the integral product of two shape functions is only non-zero when they overlap. For example setting $T(x) = \phi_1(x)$ simplifies the first of the simultaneous equations to $a_1 - a_2 = 0$. Repeating this five more times gives the matrix in equation 4.14 which can be solved to find the original field profile.

$$\begin{bmatrix} 1 & -1 & 0 & 0 & 0 & 0 \\ -1 & 2 & -1 & 0 & 0 & 0 \\ 0 & -1 & 2 & -1 & 0 & 0 \\ 0 & 0 & -1 & 2 & -1 & 0 \\ 0 & 0 & 0 & -1 & 2 & -1 \\ 0 & 0 & 0 & 0 & -1 & 1 \end{bmatrix} \begin{bmatrix} a_1 \\ a_2 \\ a_3 \\ a_4 \\ a_5 \\ a_6 \end{bmatrix} = \begin{bmatrix} 0 \\ 0 \\ 0 \\ 0 \\ 0 \\ 0 \end{bmatrix} \tag{4.14}$$

The important thing to notice in equation 4.14 is the high percentage of the

matrix, which is 0. Problems like this are easy for computers to rapidly solve even when the number of mesh elements is in the thousands.

This example covers the solving of a small one-dimensional system with no time dependence, but it should be noted that all the FEM presented in this thesis are of three-dimensional structures modelled using the COMSOL Multiphysics' RF package. This package, when added to the base COMSOL software, solves the following time dependent equation, 4.15, rather than the simple 4.8.

$$\bigtriangledown \times \mu_r^{-1}(\bigtriangledown \times \mathbf{E}) - \omega^2 \epsilon_0 \mu_0 (\epsilon_r - \frac{i\sigma}{\omega \epsilon_0})\mathbf{E} = 0 \tag{4.15}$$

Despite this, the ideas presented in the above description still apply but with far more complicated mathematics involved. In short, the weak formulation converts a differential problem to an integral one. Adding test functions and integration by parts reduces the order of differentiation to prevent discontinuities and provide for the incorporation of boundary conditions. In a three dimensional system, the boundary is the closed surface enclosing the domain. The divergence theorem is then applied to convert the volume integration to surface integration at the boundary.

Model Simplification

The FEM technique as described above does hugely simplify the task of computationally modelling a structure, but it also far from trivialises it. In this section, the methods used to design models will be described.

The primary goal in creating a model in COMSOL is to minimise the number of mesh elements without sacrificing accuracy. Figure 4.4 shows how a series shape functions within mesh elements are used to match the true form of what is being modelled. Values are chosen for the two boundaries of the mesh element, and it is assumed that the transition from one value to the other is linear within the domain. For this reason, large areas of a model that display only linear behaviour can be modelled with very few mesh elements. As a minimum, there should be at least five quadratic elements per wavelength so as to realise the behaviour. In contrast, mesh elements should be concentrated in parts of the structure where behaviour

is expected to be highly non-linear. When a structure is fully meshed, there are further techniques for reducing complexity.

Lines of symmetry within a system can be used to reduce the complexity of the model by using boundary conditions as mirrors. In cases where both sides of the structure are expected to behave identically, such as the CPW described in section 5.3, this technique can halve the computational load of a model. The boundary condition used is either a perfect electric or magnetic conductor (PEC and PMC, respectively) depending on the expected field polarisation. If electric fields passing across the line of symmetry only cross perpendicularly to it, then a PEC can replace half of the structure without altering its behaviour. The same is true for magnetic fields and the application of a PMC. Two examples of models being simplified in this way can be seen in figure 4.5.

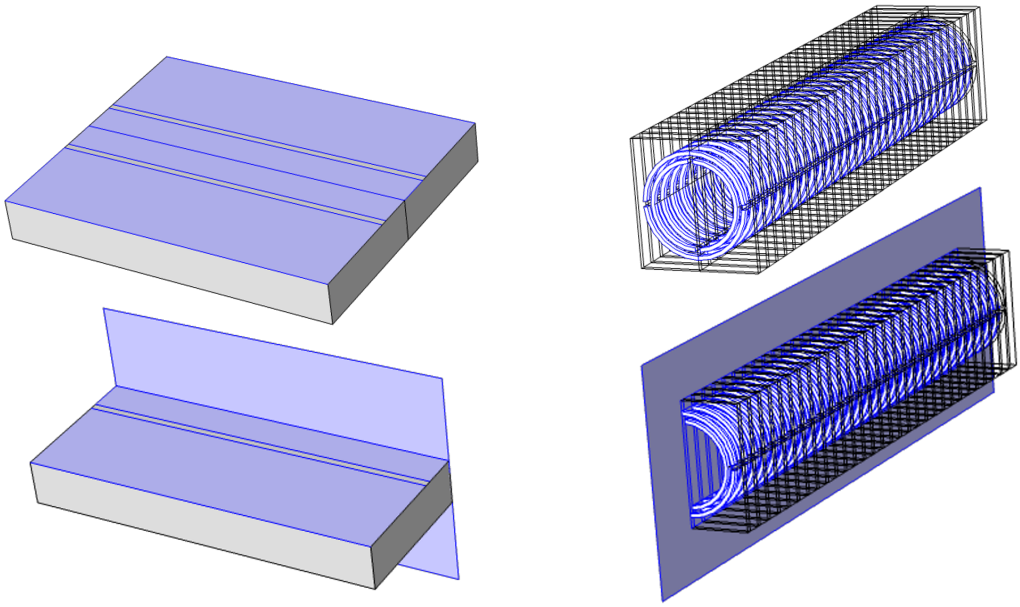

Figure 4.5: Shown are the geometries for two COMSOL models: a co-planar waveguide (Left) and a meta-atom chain (Right). The top two images show the full geometries while the bottom two images show how a PEC boundary condition can halve the structure's computation complexity. PEC boundary conditions in the models are highlighted in blue.

Along with reflected patterns, repeated patterns can be exploited when simplifying a model by applying periodic boundary conditions where the pattern repeats. In chapters 6 and 8 this was used to reduce the complexity of the repeating structure down to a single unit cell that needs to be modelled. To achieve this, Floquet periodic boundaries are placed on either side of a unit cell. Bloch wave theory is

then used to apply a phase difference between the two periodic boundaries that is determined by the model's pre-determined wavevector. In this manner, an infinitely repeating structure can be modelled from just the unit cell and the $\omega(k)$ relationship can be determined from the single cell. Further details on this relationship are given below.

4.4.2 Dispersion Relations

In chapters 6, 7 and 8 I will be probing the modes of various metamaterial structures by taking spatial field scans, an example of which can be seen in figure 4.6a. In order to fully characterise these modes it is useful to determine their dispersion relations and construct a band structure for the system. For this, a mathematical transform, known as a Fourier transform ($\hat{F}$), was applied to spatial field data to convert it to momentum space. In momentum space data can be plotted against angular frequency ($\omega = 2\pi f$) and wavenumber ($k = \frac{2\pi}{\lambda}$). Momentum space is also commonly referred to as k space since $k\hbar = p$ (where p is momentum and $\hbar$ is the reduced Planck constant). The relation between a mode's angular frequency and wavenumber is commonly known as its dispersion relation, so these are known as dispersion plots. The equation for the transformation of a function in terms of space (x) to a function in momentum space in terms of the in plane wavenumber (k_x) is equation 4.16

$$\hat{F}(k_x) = \int_{-\infty}^{\infty} f(x) e^{-2\pi i k_x x} \mathrm{d}x \tag{4.16}$$

The Fourier transform will extract the wavelength data from $f(x)$. If $f(x) = \cos(k_x x)$ then $\hat{F}(k) = \frac{\delta(k-k_x)}{2} + \frac{\delta(k+k_x)}{2}$. This is useful for two reasons: a system may support multiple modes that appear at the same frequency but do not interact with each other or travel with the same momentum. In spatial data, these modes overlap with one another and are near impossible to distinguish, but when the same results are plotted in momentum space, the two modes become clear. An example data set of such a system from chapter 6 is presented in figure 4.6. The second reason to use dispersion plots to analyse systems is that they allow for the group velocity of the

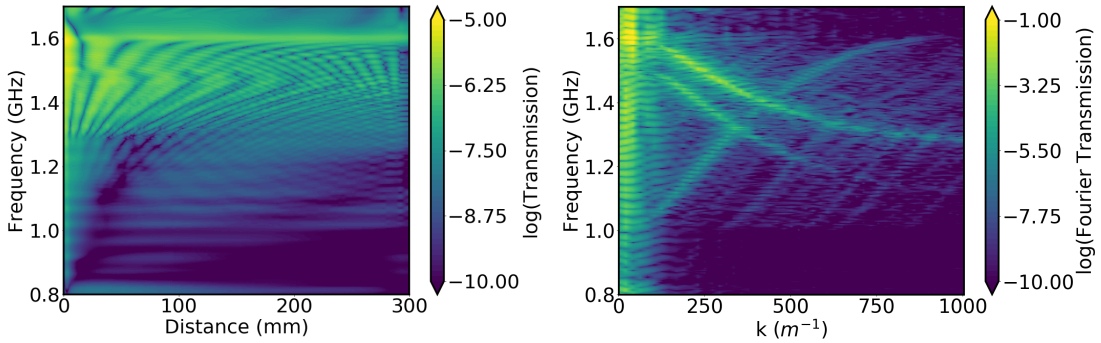

(a) (b)

Figure 4.6: (a) A plot of the transmission between one end of a resonator chain and a distance along that chain against frequency and the distance. (b) A plot of the data from the (a) that has been Fourier transformed. The two curves on this plot are the two modes supported by the chain. When the data is presented in this form, we can see that they are non-interacting as there is no anti-crossing between them and that they propagate in opposite directions. This data is discussed in detail in chapter 6

system's modes to be determined at a glance. Group velocity is defined as $v_g = \frac{\partial \omega}{\partial k}$ and so the gradient of a curve in an ω against k plot will give the group velocity.

It should be noted that while equation 4.16 is the definition for the Fourier transform, it was not the calculation performed in this thesis. Rather than fit a continuous function to the data to serve as $f(x)$, since this would amount to finding the component wavelengths in any case, a different formula is required that replaces the continuous $f(x)$ with a series of points. This Discrete Fourier Transform (DFT) is far better suited to analysing the collected data which already comes as a series of discrete points. The DFT is defined in equation 4.17,

$$X_k = \sum_{n=0}^{N-1} x_n e^{\frac{-i2kn\pi}{N}} \tag{4.17}$$

where x_n and X_k are each a series of discrete complex numbers of length N. The algorithm used to perform this calculation in the relevant chapters is the scipy fast Fourier transform (FFT) function. This algorithm can rapidly perform a DFT calculation for even large data sets, but in doing so it makes assumptions that can lead to artefacts in the transformed data if not properly accounted for by pre-processing.

One of the clearest disparities between the true system and the system assumed by an FFT algorithm is that for the FFT to function the system must be infinite. Since no true data set is actually infinite the algorithm will 'loop' the data, assuming that the final data point is immediately followed by the first, easily visualised as a sheet of paper with that data plotted upon it being rolled up so that the two ends touch. This leads to artefacts when there is a large disparity between the first and final values which the algorithm interprets as a series of sharp spikes in the 'infinite' data. To reduce this effect a window is applied to the data that matches the two ends. Some information is lost in this process so measurements taken in this thesis exceeded the ends of the sample so that those parts windowed out were not of importance. Additionally, the resultant Fourier transform of a windowed signal will be convolution of the window and the signal's Fourier Transforms. This has a minimal effect on the resultant data due to the sharp shape of the window's Fourier Transform by design. The windowing process is shown in figure 4.7.

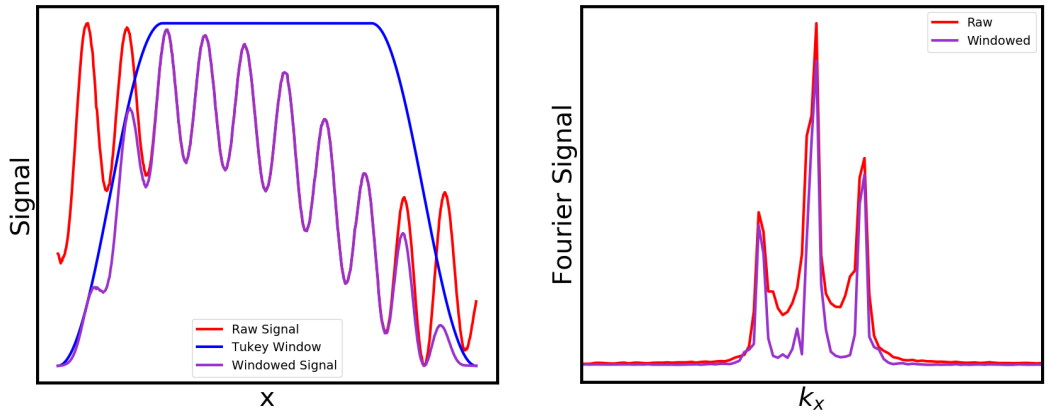

(a) (b)

Figure 4.7: (a) A plot showing an example data set that hasn't been windowed, a tukey window and the processed data set.(b) The DFT of the unwindowed and windowed data showing how the features of the windowed data are now much sharper and clearer after the transform than the unwindowed data.

Dispersion relations need not only be presented from transformed results. In a free-space far-field measurement, as described in section 8.4.1, momentum space can be probed by controlling the momentum of the exciting radiation. This can be achieved by sweeping the angle of incidence (θ) and then plotting the transmission against frequency and angle. Due to the relation $k_x = k(\omega)\sin(\theta)$, where $k(\omega)$ is

the wavenumber of light in free space at frequency ω, it is simple axis conversion to see the dispersion relation. While a less computationally taxing method to obtain dispersion data, this method cannot probe beyond any values of k greater than their free-space value. This line, at $\omega = ck$, is known as the light line and corresponds to a grazing wave or direct transmission. The light line often appears very bright in dispersion diagrams, it is the cause of the large central spike in figure 4.7b, if there is a significant amount of direct transmission between measuring antennas.

4.4.3 Numerical Modelling

Numerical analysis for the data in Chapters 5, 7 and 8 was performed using the python coding language [95] and the numpy module [96]. Within numpy is a linear algebra sub-module. By representing the coupled system to be modelled in matrix form, see section 3.1 for numerous examples, and entering that into the numpy.linalg.eig() function, the eigenvalues and eigenvectors are calculated and returned.

Chapter 5

Investigating the Dynamics of Strong Coupling Between two Microwave Resonators using Active Tuning.

The coupled oscillator model is a powerful tool for understanding strong coupling in both meta-materials and molecular nanophotonics. This power comes despite, or perhaps because of, its apparent simplicity. Many seemingly complex problems can be reduced, mathematically, to the level of masses on springs. In all the following chapters, the coupled oscillator model is used to some degree, and it has been detailed in its more general case previously in Section 3.1. This chapter will focus on one such coupled oscillator interaction and may seem, at first glance, the most basic one covered in this thesis as it entails the use of only two resonators. Two SRRs of differing dimensions are positioned adjacent to each other, one is loaded with a tunable component that allows its resonance frequency to be tuned through the resonance of the other, and their coupling terms are determined as the frequency is dynamically swept. This setup allows for an analysis of the interactions between them not previously studied with similar rigour, the results of which will guide many of the later decisions in this thesis.

5.1 Introduction

Before making comparisons between split-ring resonator based metamaterials and molecular nanophotonic structures, it is important to understand the SRR as rigorously as possible. SRRs are already an attractive option for metamaterial designs that require well-studied components due to the high degree of research focus they have garnered from the scientific community. SRRs, even in their most basic form of a single ring and a single split, offer a great degree of control over their resonant properties from relatively minor changes in structure. Additionally, they lend themselves well to endeavours that require more intricate behaviours and many variations on the basic model have been proposed and exploited. Finally, their inclusion in Pendry's famous work in 1999 [14], which many consider to have been the birth of the metamaterial field, has kept them near the forefront of research ever since, providing an abundant well of knowledge for any wishing to walk a similar path [17, 97–107].

However, in common with many metamaterial elements, SRRs have a limited frequency range over which they are resonant. Whilst work has been undertaken to fabricate metamaterials with a broad-band response [108, 109], the structures used are still fixed at manufacture and sacrifice the ability to modify their operating frequency dynamically. This attribute would be of considerable value in filter and antenna applications. More particularly, dynamical tuning would allow for functionality over a range of frequencies without sacrificing the benefits of selectivity offered by a narrow-band response. Such tuning has been achieved structurally [110, 111] by using the relationship between near field interactions of the rings and their relative positions to tune the resonant response.

It is the goal of this chapter to analyse how the coupling between two SRR's changes with relative resonant frequency. It might seem simple to achieve this by slightly altering some physical element of the SRR, as mentioned in section 3.2 many structural aspects of the design can affect the resulting resonances, but such a method fails on two fronts. First, by changing a ring's structure changes not only its resonance but also the field profile of that resonance. In such a case, the

change in coupling cannot be ascribed to frequency alone. Second, the number of rings that would need to be fabricated in order to achieve a workable resolution for conclusions is prohibitive. By making no structural changes to achieve tunability, the dynamic method presented here makes it possible to draw conclusions from the effect of resonance frequency in isolation.

This chapter will investigate the coupling between an actively tunable SRR and an adjacent passive SRR as a function of their separation and relative orientation as one has its frequency tuned through the other. It is shown that, by altering these two parameters, the strength of the interaction between the SRRs can be altered dramatically, allowing a range of coupling regimes to be explored in a single system.

5.2 Active Tuning

It is first relevant to come upon a method to achieve active tuning in an SRR. SRRs behave as resonant LC circuits and, at their simplest, may be understood as a parallel plate capacitor (the split) connected in series with a single loop inductor (the ring). The subject of SRR resonance is covered in more detail in Section 3.2, but for these purposes, it serves to repeat the formulation for the fundamental resonance frequency of an SRR, as given by equation 5.1, where L is the effective inductance of the ring and C is the effective capacitance [69],

$$\omega_0 = \frac{1}{\sqrt{LC}}. \tag{5.1}$$

Active tuning can thus be achieved via any method that might change either L or C as a function of some externally applied element. Changing the permittivity of the substrate around the resonator is one such method [112] but has a similar failing to structural methods in that such a change would also alter coupling independently of frequency. Alternatively, some lumped element might be added to the structure that has its properties tied to a biasing voltage (V). A variable capacitor (varactor) has been shown to serve such a purpose previously in the creation of tunable meta-atoms [113, 114].

A varactor consists of two layers of doped silicon, P-type and N-type (which are positively and negatively charged respectively). At the boundary between these layers, a depletion region develops. The thickness of this depletion region, and hence the capacitance of the device, can be altered by applying an external voltage; the higher the voltage, the more charge is driven across the depletion region, causing it to widen and the capacitance to fall [115].

By incorporating a varactor into a SRR (a schematic of the SRR showing the position of the varactor can be seen in Figure 5.1) the total capacitance can be altered. Since the capacitance of the varactor ($C_v(V)$) connects in series to the gap capacitance (C_g) the total is now dependent on the reciprocal addition of these terms. The smaller of the two contributions to the total capacitance dominates, making the effective capacitance:

$$\frac{1}{C(V)} = \frac{1}{C_v(V)} + \frac{1}{C_g}. \tag{5.2}$$

With this in mind, the SRR can be designed to make the best use of the varactor's tuning range. With a narrow gap of 0.1 mm and a relatively thick ring width of 1 mm and an inner radius of 3 mm, the design used in this chapter was chosen to maximise the capacitive over the inductive contribution to the resonance frequency, thereby increasing the tuning range of the SRR. An Infineon BB 857-02V H7902 varactor, which allows the capacitance to be varied between 0.5±0.05 pF at a bias of 28 V, and 5±1 pF at a bias of 0 V (taken from the manufacturer's specifications) was used as the loaded element.

In order to apply a reverse voltage across the varactor it was connected to a 30V power supply by wires soldered to each of its ports. In order to reduce the effect these wires had on the resonance of the SRR each one was coiled into loops part way along its length to create an in series inductance. This prevents high frequencies from travelling up the wire by acting as a low-pass filter but allows the DC tuning voltage to still be applied.

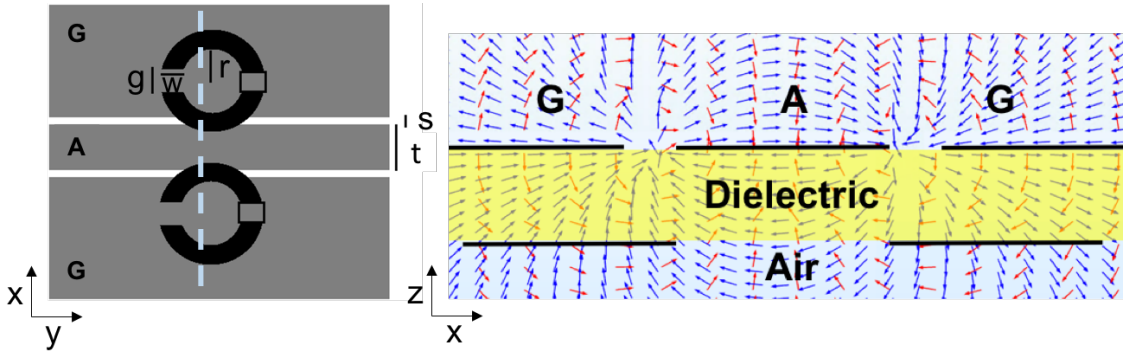

Figure 5.1: (Left) A schematic of the CPW loaded with active SRRs. The CPW channel width (s) is 0.5 mm, the active track width (t) is 5 mm, the gap size of the ring (g) is 0.1 mm, the width of the ring (w) is 1 mm and the inner radius of the ring (r) is 3 mm. The blue dotted line marks the cross-section taken to produce the right figure. (Right) A model of the magnetic (blue arrows) and electric fields (red arrows) around a transmitting CPW with no rings loaded. The position where the rings would go is marked as a black line beneath the substrate and is included to draw attention to the necessity of offsetting the rings for optimal coupling to the CPW. The scale of the arrows have been normalised and is not representative of field strength.

5.3 Coplanar Waveguide

With the active element considered, it becomes necessary to probe the SRR. A rectangular waveguide, enclosed on all sides, provides a controlled environment but offers no exact route to introducing the biasing voltage required for tuning. A Coplanar Waveguide (CPW) is a planar transmission line consisting of three separate plates of copper called the active (central), and ground (left and right) tracks separated by two narrow channels and printed onto a dielectric substrate. Electric excitation on the active track is transmitted along the CPW by fields oscillating in the two bare strips.

The electric and magnetic fields around a CPW are shown in 5.1. Unlike contained transmission lines, like rectangular waveguides or coaxial cables, the fields in a CPW extend beyond the transmission line itself. The fringing of the fields means that the introduction of a resonant component to the vicinity of a transmitting CPW will significantly modulate its S parameters, allowing the study of the component's properties. The open nature of the CPW allowed for the incorporation of circuitry without perturbing its transmissive properties off-resonance.

When designing the CPW used in this work, the primary concern was its in-

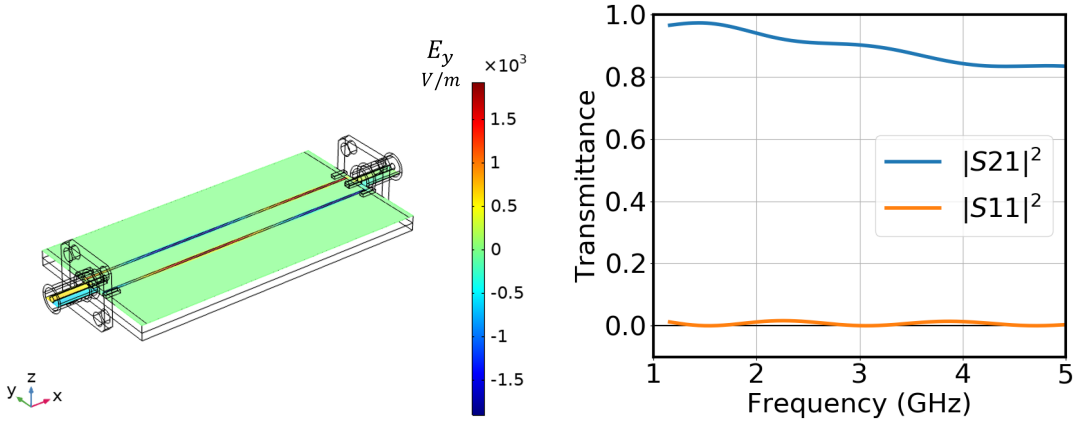

(a) (b)

Figure 5.2: a) Image of the model used to calculate CPW transmission with the electric field in the y direction plotted at the conducting plane at 3 GHz. b) The simulated reflected ($|S11|^2$) and transmitted ($|S21|^2$) power from the modelled CPW over the frequency range of interest.

put impedance (Z_0). In order to accept signal from a VNA it had to match the internal impedance of 50 Ω. The parameters that could be freely changed were the active track (t) and the channel widths (s), with the copper thickness and substrate thickness being set by the manufacturer. Parameters were initially chosen using the approximation for an infinite substrate in equation 5.6 [116]:

$$k_0 = \frac{t}{t+2s} \tag{5.3}$$

$$k_0' = \sqrt{1-k_0^2} \tag{5.4}$$

$$K(k) = \int_0^{\frac{\pi}{2}} \frac{\mathrm{d}\theta}{1-k^2 sin^2\theta} \tag{5.5}$$

$$Z_0 = \frac{30\pi}{\sqrt{\epsilon_{eff}}} \frac{K(k_0)}{K(k_0')} \tag{5.6}$$

where the effective permittivity (ϵ_{eff}) is estimated as the average between the relative permittivities of air and the substrate, as the fields occupy both equally, the infinite substrate assumption is used because only a negligible amount of the fields will fringe beyond the substrate. From these initial parameters, the design was finalised iteratively using finite element modelling software to match the 50 Ω impedance.

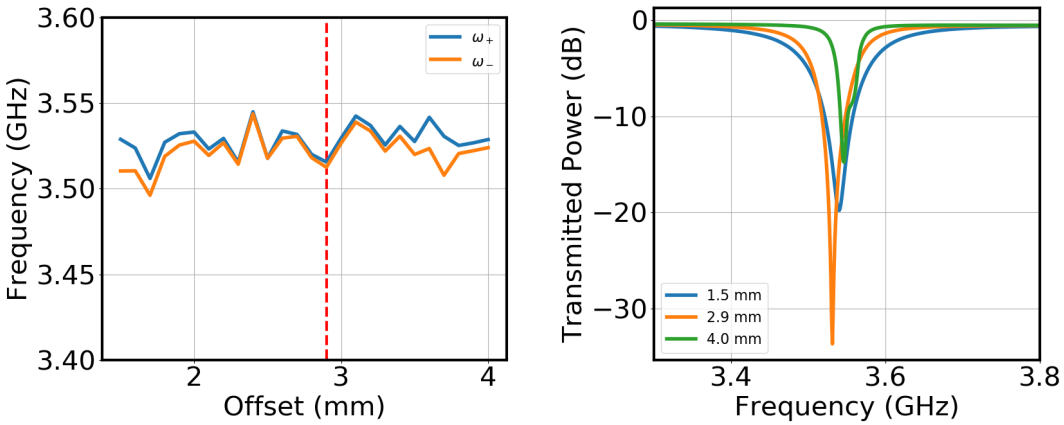

(a) (b)

Figure 5.3: (a) Plot of the two simulated eigenfrequencies, calculated for the active SRR using FEM, as their offset from the CPW channels increases. The red dashed line marks the separation between the rings chosen for experiment at 2.9 mm. (b) Plot of the simulated transmissions through a CPW loaded with an SRR beneath each track at different SRR offsets. A value of 0 mm would correspond to the center of each SRR being directly beneath the CPW channel of its corresponding side. 2.9 mm was chosen as the offset for experiments.

The resulting CPW used the dimensions t=5 mm and s= 0.5 mm. The modelled S parameters of the final CPW are shown in Figure 5.2 alongside a plot of the electric fields across the channels.

5.4 Active Tuning of an Individual SRR

When a signal is transmitted along a CPW, electric fields oscillate between the central 'signal' track and two grounded sheets on either side, marked A and G respectively in Figure 5.1. There is often an additional ground plane on the underside of a CPW to further improve transmission by confining the fields, but this is omitted here and replaced instead with a pair of SRRs printed (one beneath each track to maintain symmetry with the CPW) onto the underside of a substrate using standard PCB lithography and etching techniques.

The SRRs are excited via the fields of the guided mode of the CPW, with the distance between the plane of the CPW and the plane containing the SRRs, and the offset of the pair of SRRs from the mid-line of the CPW, both determining

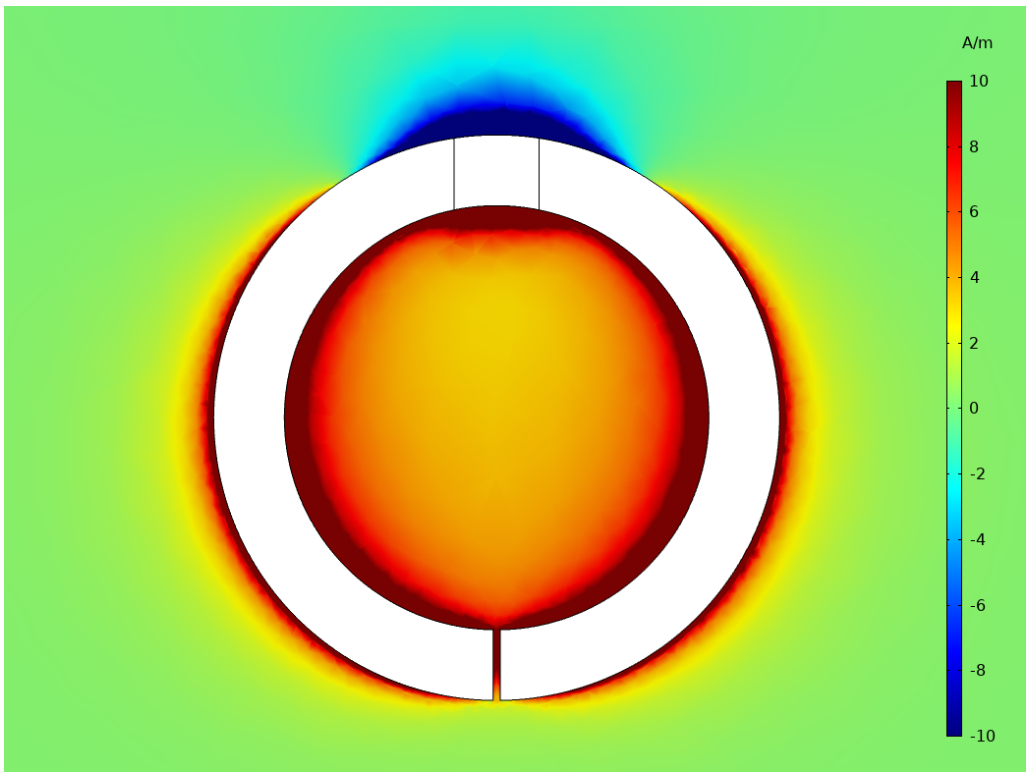

Figure 5.4: COMSOL simulation of a SRR loaded with a varactor. Colour plot shows the change in the magnetic field around an actively tunable SRR between being tuned to 6 pF loaded capacitance and 0.45 pF loaded capacitance. The magnetic field grows around the arms of the ring and in the center but decreases on its edge opposite the split. This change in field profile is responsible for the tuning dependence of the SRR's magnetic coupling.

the strength of the excitation. An offset of the SRR's position from the mid-line is required for maximum coupling to the guided mode due to the field curvature around the co-planar waveguide tracks. This is clear from Figure 5.1 which shows the electric and magnetic fields around a CPW.

By placing an SRR beneath both tracks of the CPW the coupling between the SRRs and the radiation guided along the CPW, and thus the clarity of the results, is increased. Finite element modelling was used to confirm that any interaction between the two rings beneath each track was small and would have a negligible effect on their resonant frequency. Figure 5.3a shows how the modes of the rings beneath each track change with and offset from being aligned with the channels. Whilst there is a splitting between the two SRR modes at 2.9 mm of 6 MHz it is far smaller than the simulated mode width of 74 MHz shown in the figure 5.3b. For a more detailed exploration of the interactions of SRRs and CPWs, the reader is directed to Baena's *et al.* work [117].

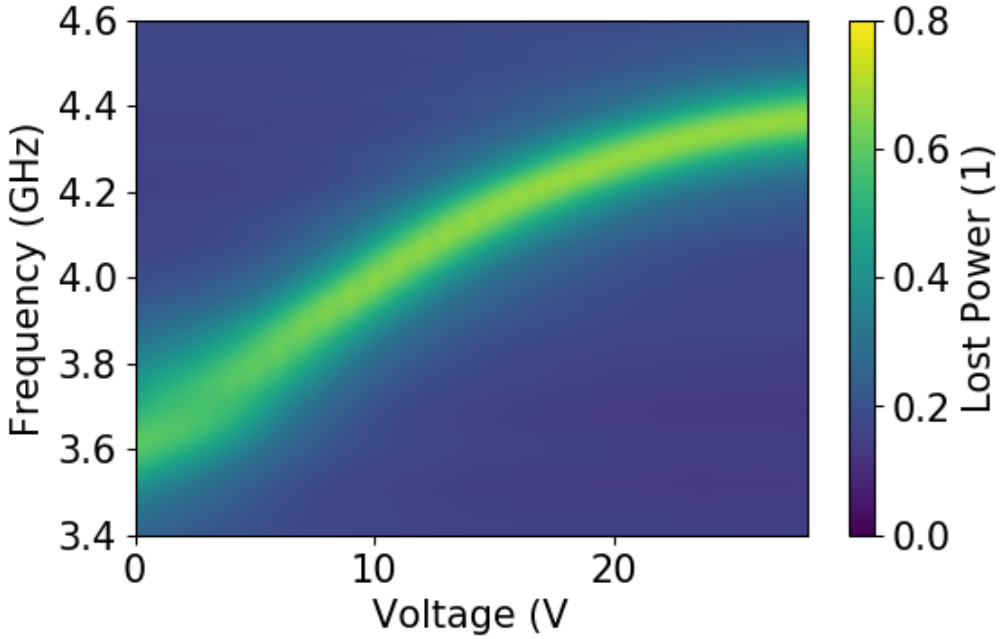

(a)

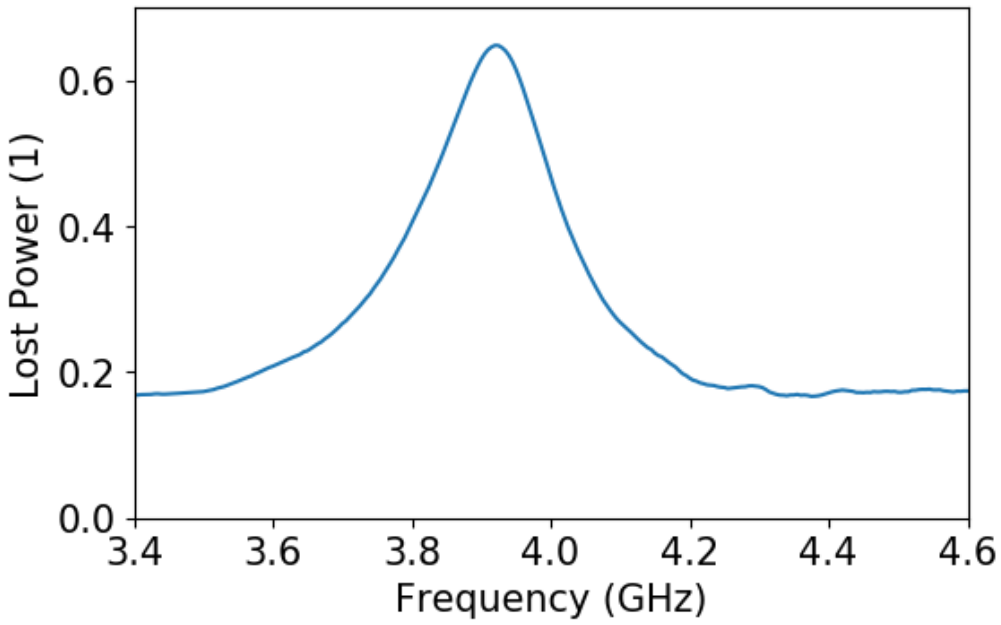

(b)

Figure 5.5: a) Experimentally measured power lost through a CPW coupled to two SRRs (one beneath each channel as in the left panel of figure 5.1), each loaded with a variable capacitor (varactor), as a function of frequency and biasing voltage across the varactor. The peak in loss, indicating a resonance of the SRR, is tuned from 3.61GHz to 4.46GHz. b) Cross section of the lost power at a bias voltage of 8 V.

Figure 5.4 shows a COMSOL model of an actively tunable the SRR with a colour plot of the change in magnetic field as the ring is tuned from minimum to maximum bias voltage (maximum to minimum variable capacitance). Of note in this plot is how the change is not spatially uniform, indicating that there is not simply a magnitude change in magnetic field. Rather, there is a region of decreasing magnetic field at the outer edge of the ring opposite of the split and an increasing of magnetic field everywhere else. This change in magnetic field profile will result in a change in the strength of magnetic coupling as the ring is tuned in frequency.

To characterise the response of the SRRs the power reflected from, and transmitted through, a 3 cm length of the CPW + SRRs system as a function of frequency was measured using an Anritsu MS46122B Vectorstar vector network analyser (calibrated using a standard SOLT procedure). We subsequently calculated the power lost from the system, which is a combination of absorption and radiation scattered into free space, as 1−Transmission−Reflection. This lost power was measured as the varactor was tuned across its full functional range of 0 to 28 volts, see Figure 5.5, yielding a tuning range of 3.61 to 4.36 GHz for the resonance of the SRR.

The Q factor also shows a dependence on the tuning voltage, with the Q of the tuned mode increasing as it increases in frequency. This broadening is an inhomogenous effect and is due to the voltage put across the varactor by the resonance of the ring. Though the resonating currents will always apply a changing voltage of their own, at low biasing voltage, and high tunable capacitance, the oscillating fields in the ring will forwards bias the varactor half of the time. This is a quite non-linear effect which changes the rings resonance. When the VNA averages these fluctuations it results in a broader and less intense mode. As the varactor is reverse biased by the tuning voltage it moves out of the region where the lowest applied voltage on the ring is enough to apply a net forward bias.

5.5 Coupled SRRs

Two SRRs, when excited in close proximity to each other, exchange energy through their overlapping electric and magnetic fields. The pair of resonators act as coupled

harmonic oscillators, allowing an analysis similar to that of a classical system of masses on springs [118]. For such a system of two coupled resonators there exist two hybridised modes; a higher frequency mode (ω_+) and a lower frequency mode (ω_-). However, unlike simple mechanical resonators, since SRRs exhibit bianisotopy (an exciting electric field induces a magnetic dipole moment as well as an electric dipole moment - and vice versa), one must consider the interaction between the SRRs via both the electric and magnetic dipole moments. Recall from section 3.2 and Figure 3.3, one can see that the magnetic dipole moments of a pair of axially oriented SRRs will couple longitudinally, whilst the electric dipole moments will couple transversely. In addition, depending upon the relative rotation of the SRRs, the coupling via the electric and magnetic dipole moments can either be in conflict or in concert, allowing the strength of the coupling to be controlled via rotation of one of the SRRs. A full description of the coupling mechanisms between dipoles can be found in Section 3.3.

The complexity of these interactions requires an analysis similar to that of Liu *et al.* [119] where the modes of the two coupled rings can be derived from a Lagrangian analysis of the charges moving inside the rings. Equation 5.7 gives the frequency for the coupled modes, ω_+ and ω_-:

$$\omega_\pm^2 = \frac{1}{2(1-K_H^2)}\Bigg(\omega_a^2+\omega_p^2-2K_EK_H\omega_a\omega_p \pm \sqrt{(\omega_a^2+\omega_p^2-2K_EK_H\omega_a\omega_p)^2-4\omega_a^2\omega_p^2(1-K_H^2)(1-K_E^2)}\Bigg) \tag{5.7}$$

where ω_a is the isolated resonance frequency of the tunable SRR, ω_p is the isolated resonance frequency of the passive SRR and K_E and K_H are the dimensionless electrical and magnetic coupling terms respectively. Equation 5.7 can be solved by treating ω_+ and ω_- as simultaneous equations,

$$\omega_+ + \omega_- = \frac{1}{1-K_H^2}(\omega_a^2+\omega_p^2-2K_EK_H\omega_a\omega_p) \tag{5.8}$$

$$\omega_+\omega_- = \omega_a^2\omega_p^2\frac{(1-K_E^2)}{(1-K_H^2)} \tag{5.9}$$

which can in turn be combined to determine K_H^2

$$K_H^2 = \frac{1}{\left(\omega_+^2-\omega_-^2\right)^2}\left(\begin{array}{l}\omega_+^4+\omega_-^4-\left(\omega_1^2+\omega_2^2\right)\left(\omega_+^2+\omega_-^2\right)+2\omega_1^2\omega_2^2 \\ \pm\sqrt{\begin{array}{l}\left(\omega_+^4+\omega_-^4-\left(\omega_1^2+\omega_2^2\right)\left(\omega_+^2+\omega_-^2\right)+2\omega_1^2\omega_2^2\right)^2 \\ +\left(\omega_+^2-\omega_-^2\right)^2\left(2\left(\omega_1^2+\omega_2^2\right)\left(\omega_+^2+\omega_-^2\right)\right. \\ \left.-\left(\omega_1^2+\omega_2^2\right)^2-\left(\omega_+^2+\omega_-^2\right)^2\right.\end{array}}\end{array}\right) \tag{5.10}$$

before finally factoring equation 5.10 back into equation 5.7 to find K_E^2.

5.6 The Coupled Modes of a Passive and Tunable Split-Ring Resonator Pair

To examine the coupled SRR interaction I used a similar setup to that described in section 5.4, but with the addition of a passive SRR placed between the CPW and the tunable SRR (see figure 5.6). The passive SRR was designed such that its resonance frequency was mid-way between the upper and lower frequency limits of the tunable SRR (approximately 4 GHz), thus allowing the resonance of the tunable SRR to be "tuned through" that of the passive SRR. To this end the passive SRR was designed with the following dimensions: $r = 2.4$ mm, $g = 0.8$ mm, $w = 0.9$ mm.

Whilst the tunable SRR was kept at a fixed distance from the CPW, the separation between the tunable and non-tunable SRRs could be altered through the use of additional spacer layers from 0.8 mm to 2.0 mm at 0.4 mm intervals. Altering this separation changes the coupling strength between the resonators since coupling arises from near-field interactions between the fields of the individual SRRs. In addition, the non-tunable SRRs can be rotated relative to the tunable SRRs, giving an additional avenue for controlling the coupling strength as orientation controls whether the dipoles act in concert or conflict. This rotation by angle θ is marked by the green arrow in Figure 5.6. Recall Figure 3.6 and the orthogonality of dipoles

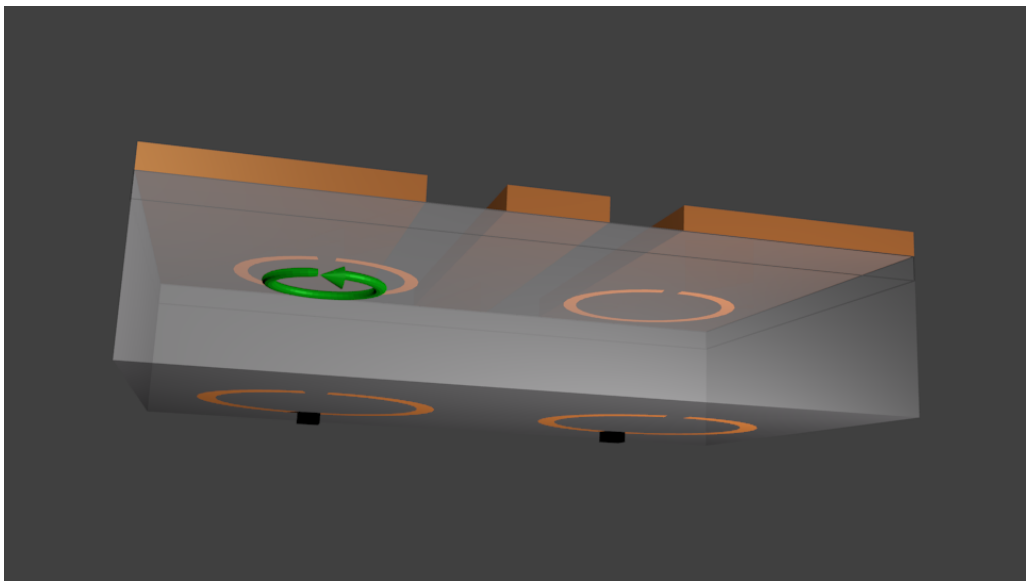

Figure 5.6: 3D schematic of a CPW with split-ring resonators stacked beneath it. The lower rings are loaded with varactors (black regions) to make them actively tunable via an applied voltage. A pair of resonators are coupled to each track of the CPW to maintain symmetry. Shown in green is the angle of rotation, θ, used to re-orientate the rings.

in an SRR, at 0° the electric dipoles will be in their high energy orientation whilst the magnetic dipoles will be in their low energy orientation. In this case they are in conflict but a rotation of 180° reverses the electric dipoles and allows the two coupling effects to act in concert.

The loss from the system was measured to find the positions of ω_+ and ω_- as a function of the tuning bias voltage for relative SRR rotations of 0°, 90° and 180° and SRR separations of 0.8 mm, 1.2 mm, 1.6 mm and 2.0 mm. A plot of the loss spectra in the 90° case is shown in Figure 5.7. The mode positions were extracted from these spectra using a peak fitting algorithm. In some cases, the modes did not couple well to the CPW and were not directly observable in the loss spectra. In these cases, estimates were made through a combination of matching to finite element models and keeping the calculated coupling terms continuous. Figure 5.8 shows theses extracted mode positions for all measured separations and angles.

The resonance frequency of the passive ring is slightly different for each data set as their orientation and proximity to the CPW has a small effect on their resonance frequency. Using the values for the mode positions extracted from the loss data sets, K_E and K_H where calculated, as described above, and are plotted in Figure

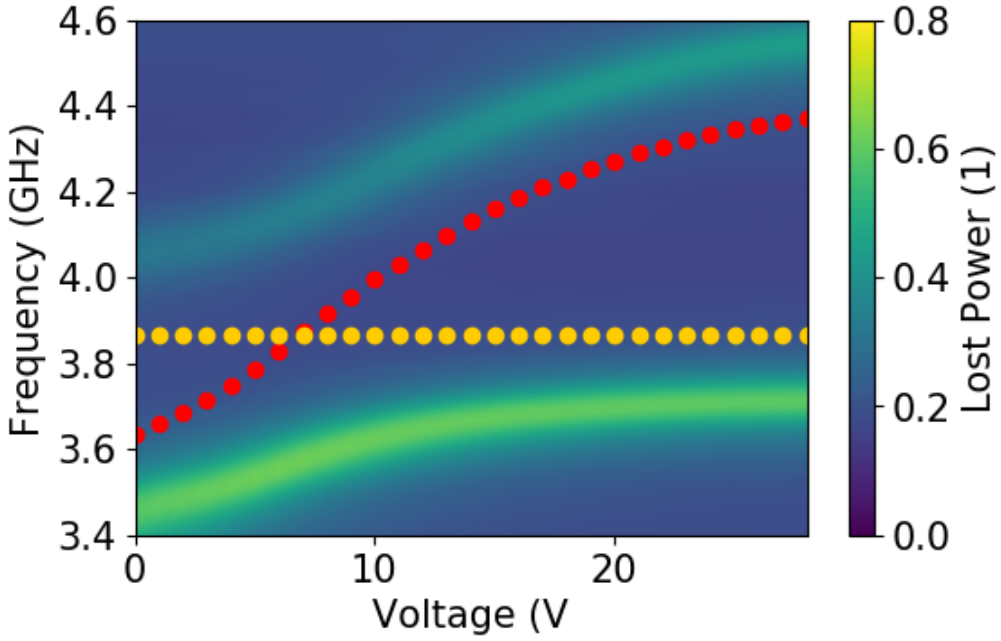

(a)

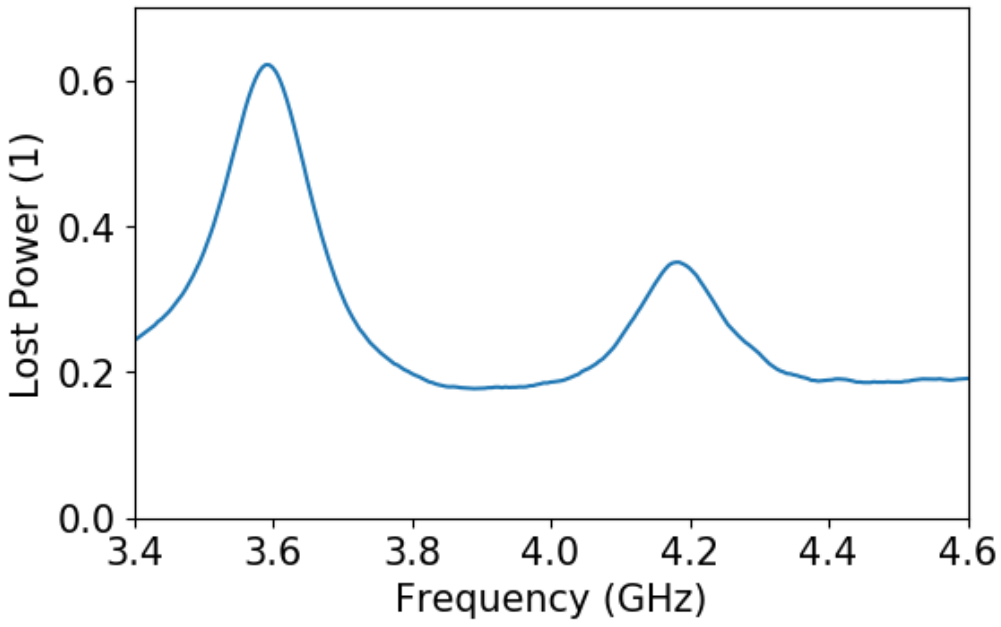

(b)

Figure 5.7: (a) Plot of experimentally measured loss (normalised to the input power) of the CPW coupled to an SRR pair as one ring is tuned through the resonant frequency of the other. The resonance frequencies of the individual active and passive SRR's are plotted as red and orange dotted lines respectively. (b) Cross-section of lost power at a bias voltage of 8 V.

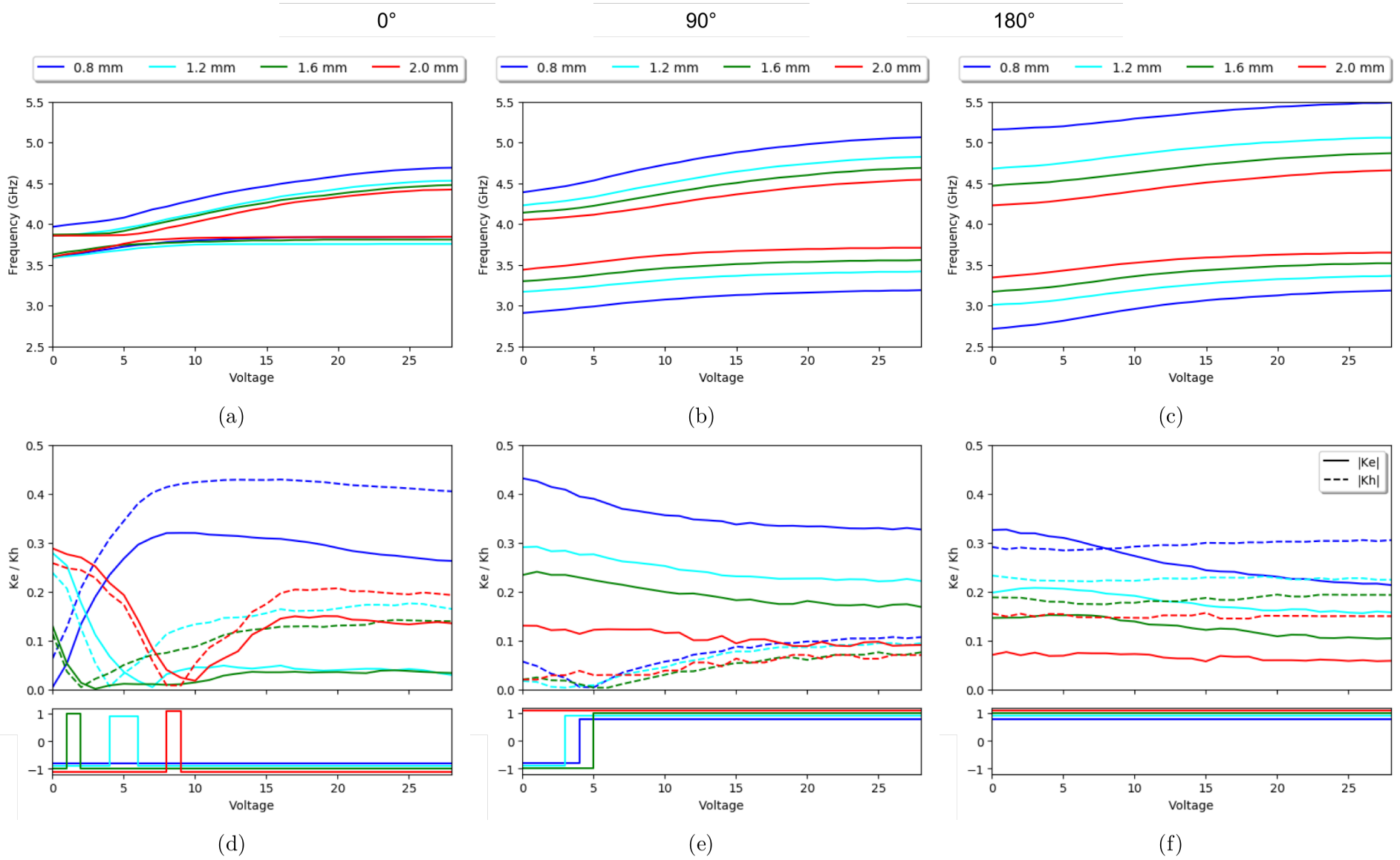

Figure 5.8: Plots of upper and lower mode frequencies (a-c) and coupling terms K_E, solid, and K_H, dashed, (d-f) for systems of two coupled SRRs at separations 0.8, 1.2, 1.6 and 2.0 mm (different colours) and relative orientations of 0° (a and d), 90° (b and e) and 180° (c and f) as a function of the bias voltage applied to the varactors. The bottom segments of d-f show whether the electric and magnetic coupling terms are in conflict, -1, or in concert, 1, but have been slightly offset for legibility.

5.8 using solid and dashed lines respectively.

Starting with subfigures 5.8a and 5.8d we see that, in the 0° case, while the frequency splitting between the modes is relatively small, the magnitude of the coupling terms, and hence the interaction strengths via the electric and magnetic dipole moments, is relatively large. However, because the two coupling terms are in opposition with each other, the net effect is a small splitting despite the strong interactions. Also notable is that K_E and K_H change which is of most significant magnitude as the tuning voltage is traversed for the 1.2 mm, 1.6 mm and 2.0 mm separations. This indicates that by tuning the varactor, one can determine whether the higher energy mode of the system is the symmetric or anti-symmetric of the coupled modes. Recall Figure 5.4 as to why the K_H term is also varying with tuning voltage, not just K_E.

In the 90° case, subfigures 5.8b and 5.8e, the frequency splitting is strong. However, the coupling appears to be dominated by K_E while the K_H term is minimal, even though the electric dipoles are orthogonal to each other. This is due to the rotational asymmetry of the ring; when the SRR is rotated, the electric dipoles are not only rotated, they are also offset from each other. This allows for a strong electrical interaction between the dipoles where theories that only take account of the angle predict none [119]. Also notable in this case is the fact that the magnetic terms, while small, go through a transition near the uncoupled crossing point where they change from being in opposition to the electric terms to be being in concert with them.

Finally, the 180° case displays the greatest splitting of the three rotations, but has coupling terms that are no bigger, and if anything are smaller, in some cases than the others. The small values are because the 180° case leads to the largest horizontal offset, and hence smallest interaction strength between the electric dipole moments, of the three rotations. However, this doesn't result in a smaller splitting because K_E and K_H work in concert for this orientation. Also notable in this plot is the crossing between K_E and K_H in the 0.8 mm separation case. Since K_E and K_H act in concert, this does not result in a change in dipole symmetry of the modes,

as was the case for 0°. Instead, whether the asymmetric splitting is weighted to be above or below the passive frequency, is governed by the relative magnitude of K_E and K_H.

Even though I am predominantly interested in the strength of the coupling between the SRRs, for completeness I should also comment on the strength of the coupling of my CPW to the different modes, as determined from the width and depth of the transmission minima in my data. These features can be readily understood by considering the net electric and magnetic dipole moments of the SRR pairs, and the orientation of the fields of the guided mode of the CPW; the coupling is strong when a large net dipole aligns with the CPW fields [120].

Firstly we refer back to Figure 3.3 and note that the net electric dipole moments will be in the plane of the SRRs, whilst the net magnetic dipole moments will be orthogonal to the plane of the SRRs. Secondly, we refer back to the field plot of Figure 5.1 and note that the electric field at the position of the upper SRR, where it is strongest, is largely in the plane of the SRR and polarised perpendicular to the tracks of the CPW (so can couple to the net electric dipole moment of the SRR pair *depending upon the orientation of the net electric dipole moment relative to the electric field direction*, whilst the magnetic field has a component orthogonal to the plane of the SRRs (so can always couple to the net magnetic dipole moment of the SRR pair).

Finite element modelling of the eigenmodes for the coupled ring pair indicates that the lower frequency modes for all systems correspond to the mode with parallel magnetic dipole moments in each ring, and hence a large net magnetic dipole moment. As such, the low-frequency modes are always strongly coupled to by the CPW, with the variation in the coupling between the three relative rotations coming from the different strength of the net electric dipole moments for each case. Since the magnetic dipole moments of the higher frequency modes correspond to the SRRs having anti-parallel magnetic dipole moments, the coupling to these is dominated by the interaction of the fields of the CPW with the net electric dipole moments of the SRR pairs.

In the case of a 0° relative rotation of the SRRs the higher frequency mode has anti-parallel electric dipole moments, and hence a small net electric dipole moment, and is weakly coupled to (even though the net dipole moment is co-linear to the polarisation of the mode of the CPW). In the case of a 180° relative rotation the electric dipole moments of the individual SRRs for the higher frequency mode are parallel, and co-linear with the polarisation of the mode of the CPW, resulting in this mode being strongly coupled to by the CPW. In the 90° case the electric dipole moments of the individual SRRs are orthogonal, and as such the net moment is somewhat between that of the 0° and 180° cases. However, since it is the SRR closer to the CPW that has been rotated resulting in its electric dipole moment being orthogonal to the polarisation of the electric field of the CPW, and since it is the electric dipole moment of this SRR which will most strongly interact with the fields of the CPW due to its proximity, the coupling to the higher frequency mode for the case of a 90° rotation is also weak.

5.7 Conclusion

I have designed and fabricated a tunable split-ring resonator by incorporating a varactor. Through the application of a bias voltage, the resonance frequency of the fundamental mode of the SRR can be tuned between 3.61 GHz and 4.48 GHz. This range is five times larger than the frequency width of the mode (160 MHz). I have used this tunable SRR to investigate the coupling to a second non-tunable SRR, and have observed an anti-crossing behaviour typical of coupled systems by tuning one ring's resonance frequency through that of the other. By changing the separation between the rings, and their relative rotation, I have been able to modify the strength of the coupling between the SRRs over a wide range. Such investigations into the coupling between meta-atoms in close proximity to each other helps to illuminate the difficulties and opportunities when designing dense metamaterials in later chapters.

The most important result of this chapter is that, where the near-field is concerned, the consideration of an SRR as just two orthogonal dipoles falls apart. This is most apparent in the 90° ring orientation where such an assumption would con-

clude a near zero value for K_E based on the orthogonality of the electric dipoles in this case. Indeed, previous works on SRR orientation have concluded precisely this, the lack of electric coupling at 90°, despite contradictory fluctuations in their coupling data at the 90° orientation [119].

These results guide the decision to utilise non-bianisoropic SRRs in chapters 6 and 7 in order to minimise the effect the conflict/concert dichotomy between the electric and magnetic dipoles. As mentioned in section 3.4, the behaviour of aggregate structures, both J and H, are governed by the single dipole of each molecule and, as seen here, incautiously arranged SRRs are not.

Chapter 6

Anti-crossing Between Counter Propagating modes in an Aggregate-inspired 1D Microwave Waveguide.

The discussion of the previous chapter was of a resonant pair of SRRs, so it seems only suitable to progress to exploring the dynamics of a linear chain. This is more than just a logical development, it is also an important step in drawing my first direct comparison between metamaterials and nanophotonics in this thesis. As covered previously in section 3.4, molecular aggregates, rather predictably, aggregate, and have remarkably different photonic properties from the molecules of which they are comprised when they do so. These aggregated structures take the form of molecular chains, and it is these chains and their properties that the following chapter seeks to emulate with copper and dielectric. In this chapter four different SRR based meta-molecules are proposed and studied in isolation and as a linear chain. Two of the structures replicate the two J and H aggregate types, the third combines them in a simultaneous structure and the final design utilises the control offered by metamaterials to couple the two mode types together in a truly novel composition.

6.1 Introduction

A traditional description of either metamaterials or molecular aggregates is unlikely to provoke in the reader a sense that one is strongly comparable to the other. In scale, construction and applied purpose they differ greatly. Additionally, one of metamaterials' most oft boasted strengths are their ability to produce phenomena beyond those in naturally occurring materials. One could certainly wonder if turning them to the task of replicating the organic, when they might be thought to surpass it, is a worthwhile endeavour. However, it is not in their general character that the strength of this analogy becomes apparent but in their fundamental nature.

Typically inter-molecular separations in aggregates are very much smaller than the wavelengths associated with the optical transitions they support, the interactions between molecules in an aggregate are thus dominated by near-field interactions, typically of a dipole-dipole character. When described in this manner it is hoped the reader can begin to see how very little has changed between the description of interacting molecules, and the discussions of near-field dipole-dipole interactions between meta-atoms (SRRs) in the previous chapter. As to the scientific worth of making such a comparison, consider that optical investigations of molecular aggregates are frequently based on far-field optical spectroscopy techniques [80]. Even near-field techniques cannot probe aggregate spatial structure at the single molecule level [66]. These limitations make the effects of disorder and noise very difficult to investigate in a systematic way [78, 121–124], yet on cm or mm scale metamaterials such measurements are standard. This limitation of aggregate study is unfortunate since such effects may be vital in helping to resolve the mechanisms behind exciton transport in nanowires/filaments [125–128], thereby hindering efforts to develop molecular materials. One interesting approach has been to simulate aggregate behaviour by making use of plasmonic particles as mimics of atoms/molecules, and much insight can be gained in this way [129], however it is still challenging to pack many such molecules within a wavelength. Furthermore, it is important to separate out electric and magnetic interactions if one wishes to mimic molecular aggregates, which is hard to achieve in plasmonic systems.

The relative ease of interrogation that metamaterials display has the same source as the reason they are, as of today's manufacturing techniques, unsuitable to matching aggregates in practical application: their scale. A sensor [130], molecular magnet [131], single photon source [66] or any nanophotonic materials [83, 132] which replaced aggregates for meta-molecules and attempted to retain operating frequency would be prohibitive in either size or cost. Thus, then, to the approach presented here where cm-scale analogues of molecular aggregates are created using microwave-domain metamaterials.

In this chapter I will establish a suitable design for individual meta-molecules, assemble 1D aggregates (chains) of these meta-molecules where the inter-molecular spacing is $\ll \lambda$, demonstrate both J- and H-type aggregation behaviour, show that both electric-dipole and magnetic-dipole coupling can be employed to explore aggregation effects and take a first step in exploring some of the potential benefits of microwave metamaterial analogues that can be further explored in following chapters.

6.2 Meta-molecule Design and Single-Element Response

Though covered previously in section 3.4 in more detail, it serves to repeat the features of molecular aggregates I seek to replicate here for clarity. When a molecule aggregates its absorption spectrum changes. The nature of this change can be discerned by treating the aggregate as a chain of coupled dipoles which, in pigments, is most often dominated by the electronic interaction. In such a chain the dipoles are either oriented transversely (H-type) or longitudinally (J-type) and this can have a significant effect on their combined properties. Most notable being the differences in their dispersion relations demonstrated in figure 6.1. Only one mode of the molecular aggregate is optically "bright" enough (has a large enough net dipole moment) to appear in the aggregate's new spectrum, corresponding to when all dipoles share a direction, as in the highest and lowest energy modes for J and

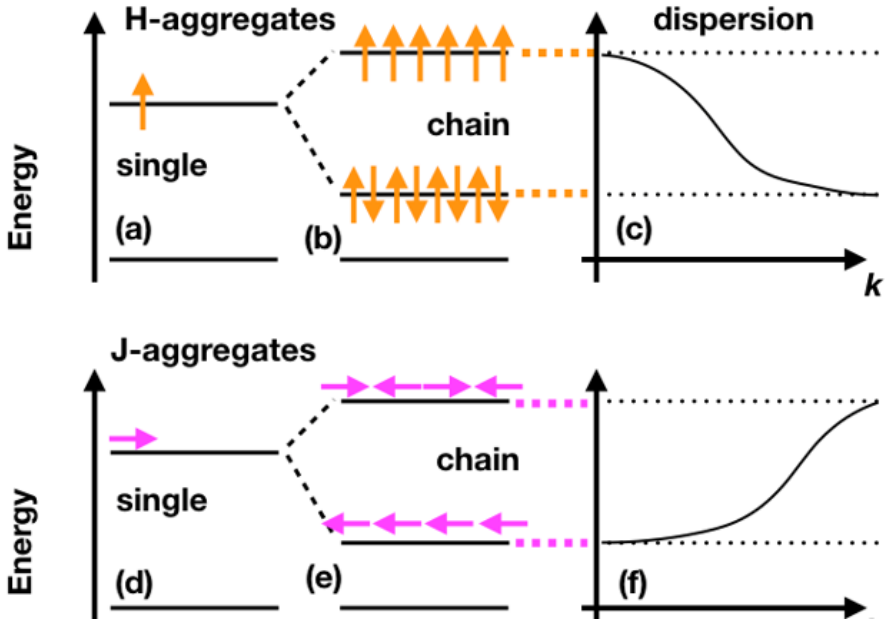

Figure 6.1: Two types of aggregate may be distinguished by the nature of the coupling between the individual molecular dipole moments. Panels (b) and (e) show the configurations and relative energies of H- and J-aggregates respectively. H-aggregates (a-c) involve transverse coupling, the highest energy state occurs when all N molecules have their dipole moments aligned, this corresponds to a zero wavenumber state; the highest wavenumber state occurs when adjacent molecules are anti-aligned, panel (c). J-aggregates (d-f) involve longitudinal coupling. The highest energy state occurs when all N molecules have their dipole moments anti-aligned, this corresponds to the highest wavenumber state; the zero wavenumber state occurs when adjacent molecules are all aligned, panel (f).

H-aggregates respectively. The fact that these features are resultant from electric dipole interactions is a problem when transitioning to the use of SRRs which support both magnetic and electric dipoles in a manner that leaves them intrinsically linked, see section 3.2 for an description of this bianisotropy.

To explore separately the interaction of transversely and longitudinally arranged dipole moments, the electric and magnetic dipole moments of my meta-molecules need to be associated with separate meta-molecule resonances.

I sought to isolate the electric and magnetic responses so as to better mimic molecular systems. A SRR can be made non-bianisotropic through the addition of opposing splits whose dipoles, at the lowest order resonance, cancel out. I therefore selected the system shown in figure 6.2 as my meta-molecule (inspired by taking the negative of the meta-atoms in [74]); it comprises two concentric metallic double-split-ring resonators, I will refer to this as the 'double ring', located inside a metal

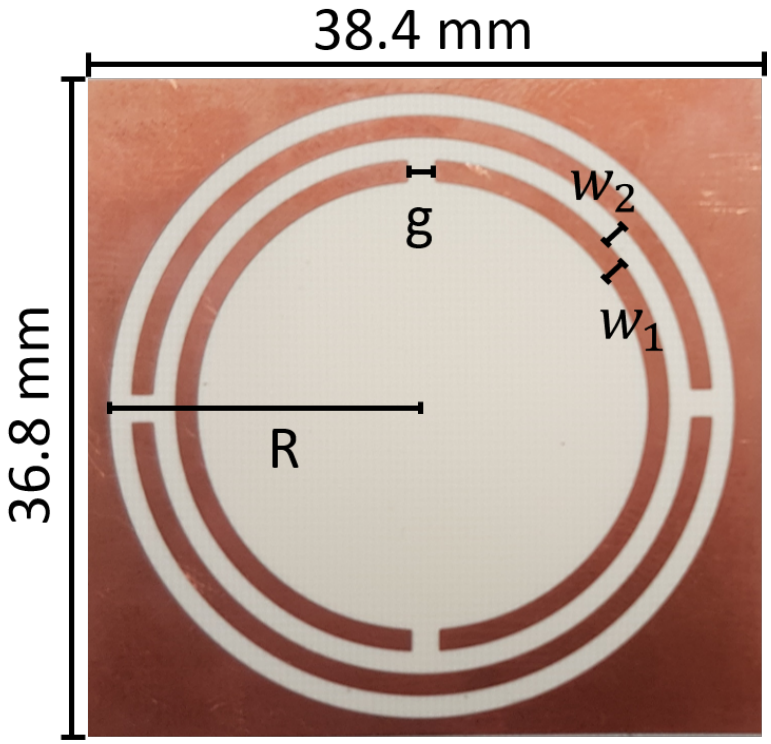

Figure 6.2: Photograph of the combined meta-molecule structure. Brown areas are copper and the white areas are bare substrate. Labeled dimensions are g = 1.5 mm, w1 = 1.2 mm, w2 =1.2 mm and R = 17.2 mm. The structure is 35 μm copper printed on 1.55 mm thick substrate.

sheet into which a circular aperture has been cut, I will refer to this last element as the 'frame'. The reason for two rings rather than one, where the two rings are offset in terms of their splits by 90°, is to further lower the resonance frequency. The inclusion of a metallic frame re-introduces the possibility for an electric dipole moment without upsetting the non-bianisotropy of the double ring. This frame mode is primarily dependent on the side length of the frame, its resonance being $\omega \approx \pi \frac{c_{med}}{x}$ where c_{med} is the speed of light in the dielectric and x is the side length, with a slight decrease in resonant frequency due to capacitance across the hole and the inductance around the thinnest point of the frame. The double ring and frame elements can be separated into their own meta-molecules, each with only a single dipole moment.

We thus have three meta-molecule designs with which to work: the frame, exhibiting as its lowest order mode an electric dipole moment in the plane of the meta-molecule; the double ring, exhibiting an out of plane magnetic moment; and the frame+double ring, which exhibits both modes in an uncoupled manner, I will

refer to this latter element as the 'combined' meta-molecule. All can be seen in figure 6.3 and the dimensions of the combined meta-molecule are shown in figure 6.2. Further details of the design are: g = 1.5 mm, w1 = 1.2 mm, w2 =1.2 mm and R = 17.2 mm where g is the size of all the ring splits, w1 is the width of the rings, w2 is the distance between rings and R is the radius of the frame. The frame has been made intentionally rectangular as it actually supports two modes, one polarised horizontally and the other vertically. Due to their orthogonality these modes would be degenerate in a square framed meta-atom. By making it rectangular these modes appear at different frequencies and can be studied separately.

The meta-molecules were fabricated on printed circuit board (PCB) using standard photolithography techniques as presented in section 4.2. The PCB consisted of 35 μm of copper on a 3.1 mm thick Roger 4350B substrate, which has ϵ_r = 3.66+0.013i in the frequency range 1 GHz to 20 GHz). It is interesting to estimate the resonance frequency of a simple split-ring with dimensions similar to those used in the present work. The inductance and capacitance can be estimated [69, 133, 134] as 10^{-8} H and 10^{-12} F respectively, giving a resonance frequency of order 10 GHz. The meta-molecules are much more complex than the simple SRR, they comprise many different contributions to the overall inductance and capacitance; they are more conveniently modelled numerically.

To establish the resonance properties of my meta-molecules I characterised the individual elements by recording their response to excitation with a near-field probe, as per the methodology of [135]. The resonance frequency of each meta-molecule design was measured using an Anritsu Vectorstar MS4644A vector network analyser. A small loop (dipole) antenna was used to excite the magnetic (electric) modes by placing it in a region of high field (as determined from the finite element modelling) approximately 0.5 mm from the surface of each meta-molecule design. The return loss was then recorded (S11, the power reflected back along the cable of the exciting antenna) for each meta-molecule and the results normalised by measuring the return loss when the exciting antenna was placed in the same position against a blank piece of substrate (all copper removed), so as to remove the frequency dependence of the

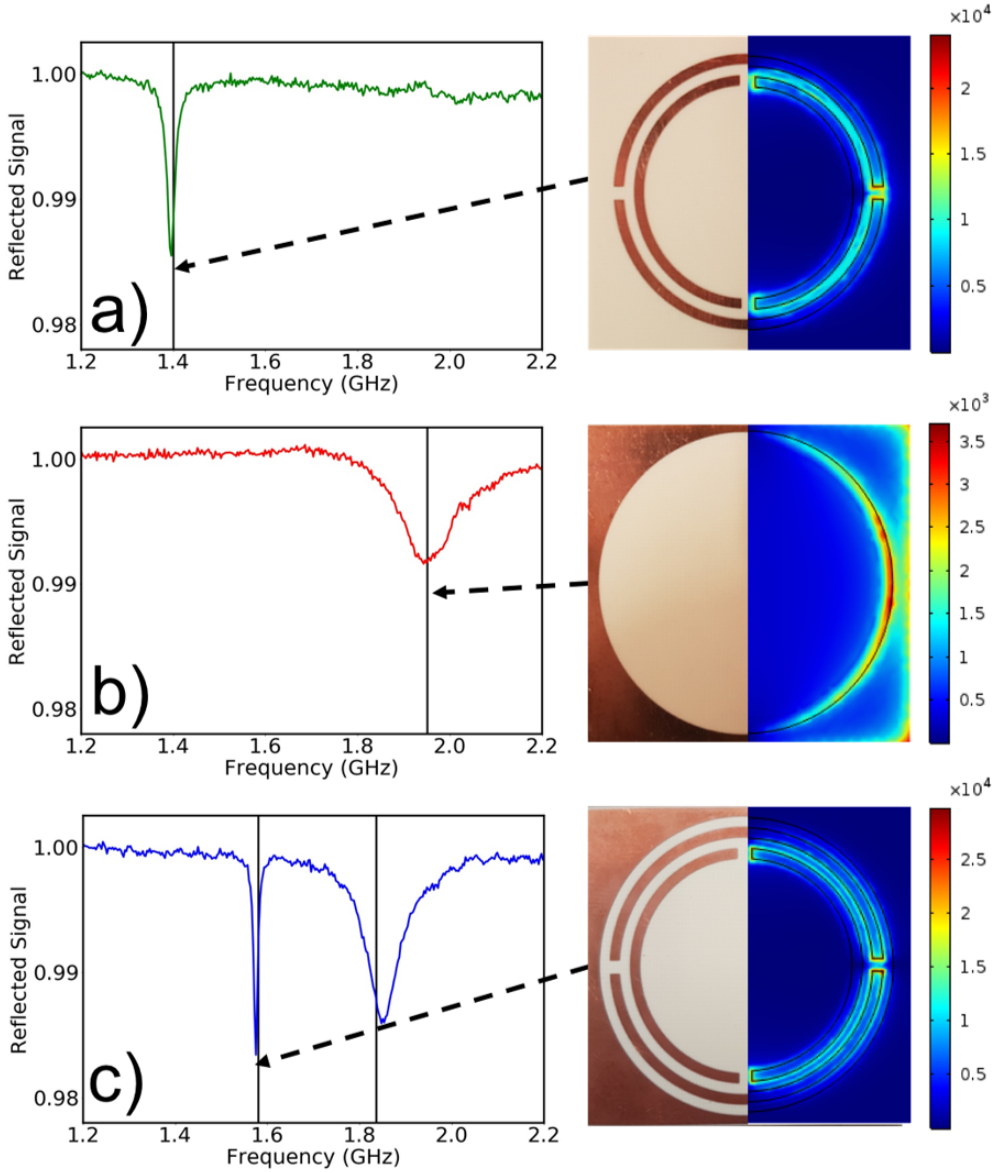

Figure 6.3: Meta-molecule designs are shown on the right hand column, dark regions correspond to copper-coated areas of a dielectric substrate, light regions to bare substrate. The structure comprises two double split-rings within a circular hole cut from a rectangular patch of metal. The rows that follow are: (a) double ring meta-molecule, (b) frame meta-molecule, and (c) combined double ring+frame. The experimental spectra (left column) show the power reflected back into a small antenna as a function of frequency when placed in a region of high field. Black vertical lines mark the eigen-frequencies predicted using finite-element models of the meta-molecules. For the composite figures for each meta-molecule (right column), the left-half of each is a photo of the as-fabricated meta-molecule, the right-half is a colour map (red indicates large magnitude) showing the numerically computed time-average of the magnitude of the electric field for the resonance frequencies predicted for each structure (see vertical lines in plots).

antennas from the data. A dip in the normalised data corresponds to a resonant mode of the meta-molecule. For the double ring, figure 6.3a, and for the frame, figure 6.3b, a single mode is seen as a dip in the reflected signal, due to power being absorbed/scattered. The origin of the modes responsible for these features is confirmed through numerical simulations using finite-element analysis and plotted as vertical black lines.

Figure 6.3c shows the measured response of the combined meta-molecule. Both electric and magnetic resonances are seen, their frequencies shifted somewhat (especially the magnetic (double ring) resonance) from those associated with the isolated structures, due to the change in the local environment of each resonator, i.e. the resonance of the double ring is perturbed by the presence of the frame and *vice-versa*. Comparing the right-hand panel in rows (a) and (c) we see that the presence of the frame does not alter the field pattern of the double-ring mode. This, together with an examination of the surface currents (not shown), indicate that when the frame and the double-ring are combined the magnetic and electric modes do not interact with each other. Instead, the additional metal around each resonator causes the mode of each to become more confined. This confinement of the fields reduces the ring and frame modes coupling to free space, their radiative loss, and thus increases their Q factor. This effect can be seen in Figure 6.3 when comparing all panels.

By tuning the design parameters (track widths, spacings, etc.) I ensured that the resonance frequencies of all the meta-molecule designs were such that, once incorporated into a chain, the J- and H-like dispersions would cover similar frequency bands. Once fabricated the meta-molecule dimensions were measured and the fabrication errors incorporated into the models. An over-etch of 12 μm in all dimensions was found, slightly reducing the size of the meta-molecules. This primarily effects the gap capacitance, but is less than a 2% change resulting in less than a 0.1 GHz shift in the intended operating frequency

6.3 Response of a Linear Chain

With the individual meta-molecule designs established, and their response characterised, I next set out to look at the response of 1D linear chains of such meta-molecules. Ninety meta-molecules were stacked axially as shown in figure 6.4 (upper), the inter-molecular separation being 3.13 mm, approximately $\lambda/20$, where λ is the wavelength in the dielectric material. To determine the collective modes supported by this chain, and their dispersion, I used a near-field probe to couple to them and recorded the response (complex field) on the edge of the sample as a function of distance along the chain. An example of a recorded field distribution is shown in figure 6.4 (lower), where the natural log of the time-averaged field magnitude has been plotted as a function of frequency and spatial position.

Next I acquired data similar to those shown in figure 6.4 (lower) for a range of frequencies, and for each frequency I carried out a fast Fourier transform. By combining such data a plot of Fourier amplitude *vs* both frequency and wavevector, i.e. a dispersion diagram, can be produced; such data are shown in figure 6.5. The double ring only data (a) show a positive gradient, i.e. J-aggregate-like dispersion, due to the longitudinally coupled magnetic dipole moments. The frame only data (b) shows a negative gradient, i.e. an H-aggregate-like dispersion, arising from its transversely coupled electric dipole moments. These data show that my meta-molecules are indeed capable of exhibiting J- and H-like molecular aggregate behaviour, as I had set out to show (see figure 3.7).

Next I used my microwave analogue system to go beyond what has been achieved in real molecular systems by combining J- and H-like behaviour into one system. The dispersion of the modes on a chain of the combined, double-ring+frame meta-molecules is shown in figure 6.6; for these data I used a magnetic (loop) probe antenna because such an antenna is able to pick up fields associated with both electric and magnetic dipole modes.

In this figure both positive (J-like) and negative (H-like) gradient modes are seen. Note that there are two H-like modes, these correspond to the two orthogonal (vertical and horizontal) modes in the frame; the frame is slightly rectangular, see top

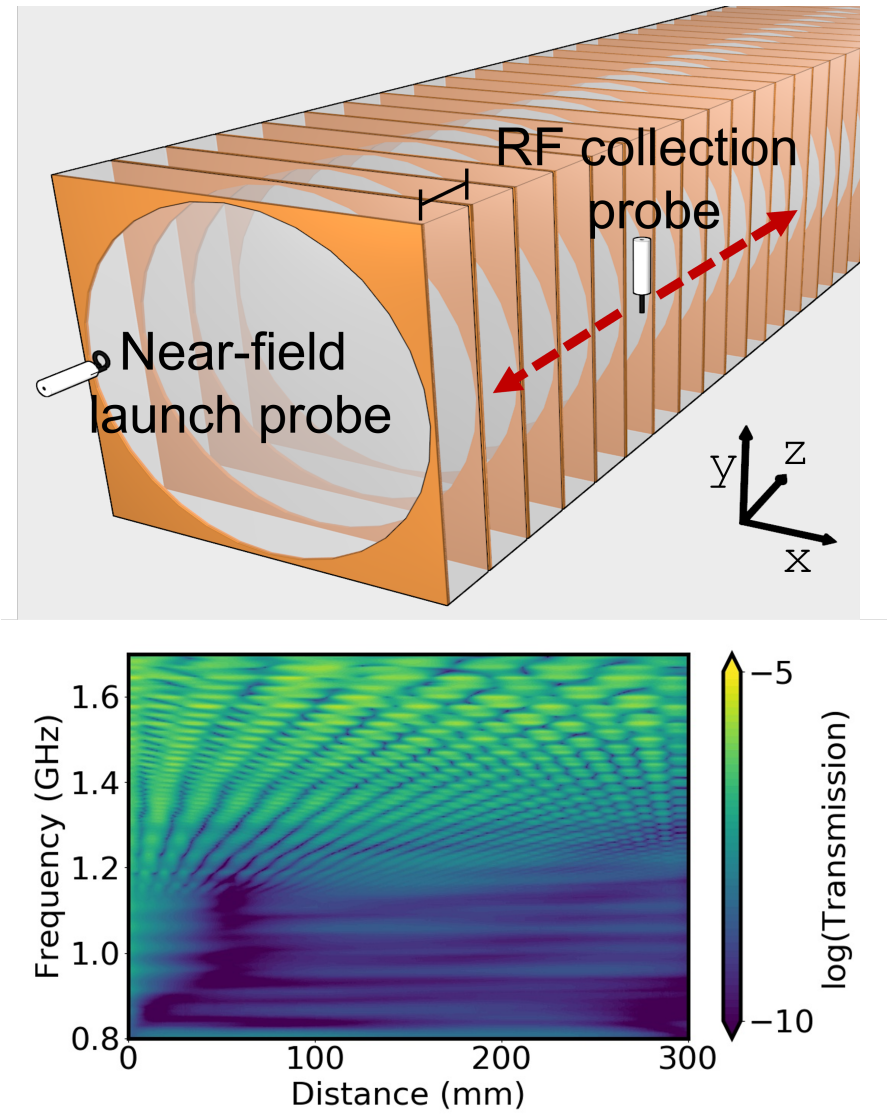

Figure 6.4: (Top) Experimental setup for chain of meta-molecules, the period is 3.13 mm. (Bottom) Plot of the time averaged complex electric field collected by the probe antenna for a system supporting a negative gradient mode from 1.7 to 1.1 GHz. See Figure 6.5b for the Fourier transform of this data into a corresponding dispersion diagram.

right panel of figure 6.3, thus lifting the degeneracy of these two modes. We see both of these modes in figure 6.6 rather than the single mode we saw in figure 6.5b because of the use of a magnetic probe antenna for these measurements. For figure 6.5 I was able to use an electric antenna and by positioning it carefully I was able to record the response from just one of the electric modes. The two mode crossings near 375 m^{-1} and 400 m^{-1} provide clear evidence for an absence of coupling between the counter propagating modes in this configuration. Examination of the structure in the simulation, shown in figure 6.7, reveals the nature of this non-interaction.

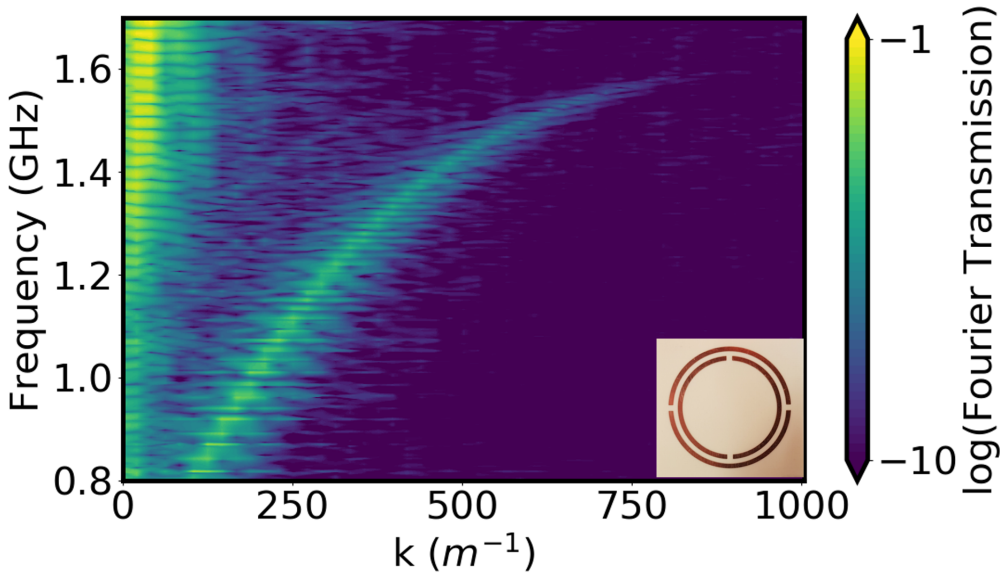

(a)

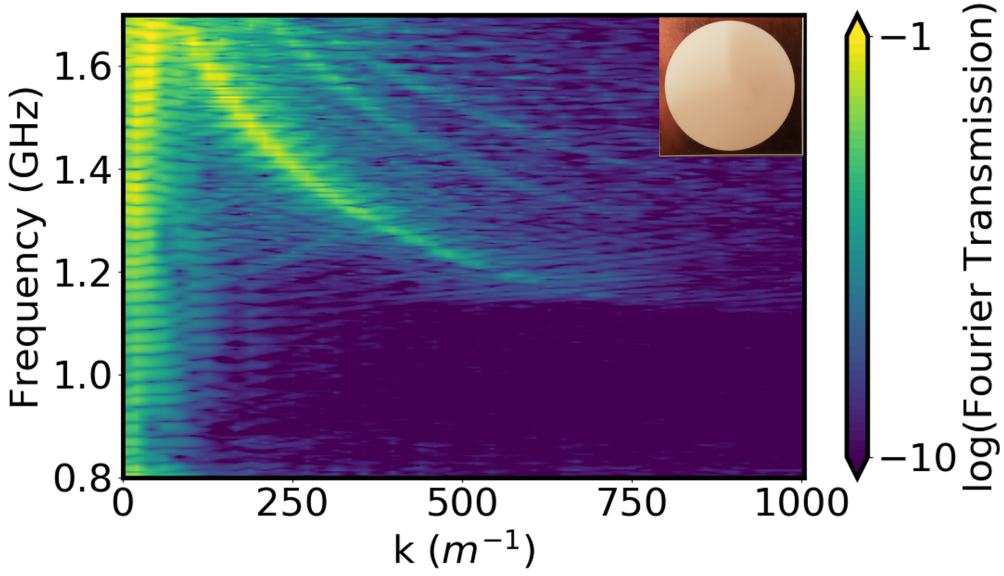

(b)

Figure 6.5: Dispersion for chains of double ring meta-molecules, and for chains of frame meta-molecules with single meta-molecules inset. Colour plots of the Fourier transformed scan data from the double rings sample (a) and the frame sample (b). The weaker, higher k "echoes" in the frame sample (b) are due to reflections from the end of the finite chain. The colour scale represents the Fourier amplitude on a logarithmic scale, yellow indicates large amplitude. The high values (yellow regions) around $k \sim 0$ are due to direct transmission between the launch antenna and the probe antenna.

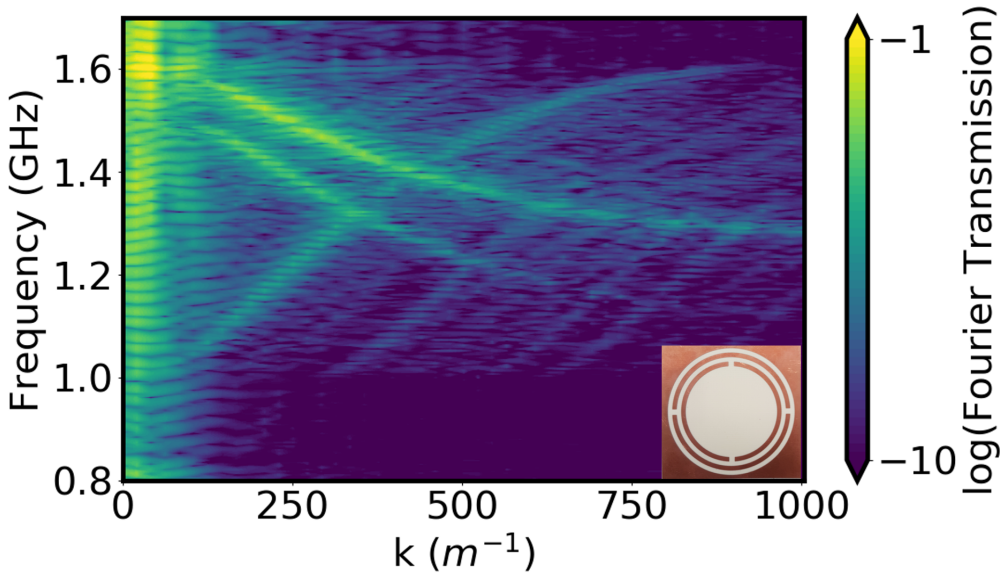

Figure 6.6: Dispersion for chains of double ring + frame meta-molecule with a single meta-molecule inset. Contour plots for the symmetric combined sample. Sample supports a forward and backward propagating mode. The high values (yellow regions) around $k \sim 0$ are due to direct transmission between the launch antenna and the probe antenna.

In figure 6.7a the z component of the magnetic field is plotted for the mode associated with rings, clearly showing high magnetic field around the inner ring. Comparing this to the magnetic field in figure 6.7c we can note two things: First that there is almost no magnetic field between the rings and that there is an anti-symmetry in the magnetic field direction at the top and bottom of the frame. The first point lowers the degree by which the presence of the frame perturbs the ring mode. The effect of the second point is that the localised magnetic fields cancel with each other to produce no net magnetic dipole in much the same way that oppositely orientated splits cancel in the electrical case, shown in figure 6.7b-d.

Lastly, with these in mind, I sought to exploit an advantage of the superb degree of structural control available with metamaterials by introducing a modification intended to break the symmetry of my meta-molecule design. By breaking the symmetry of the double rings along one axis their electric dipoles will no longer cancel. The small net electric dipole remaining will be able to couple to the electric dipole of the frame. As discussed in section 3.1, the coupled modes will no longer be able to be degenerate and an anti-crossing will appear.

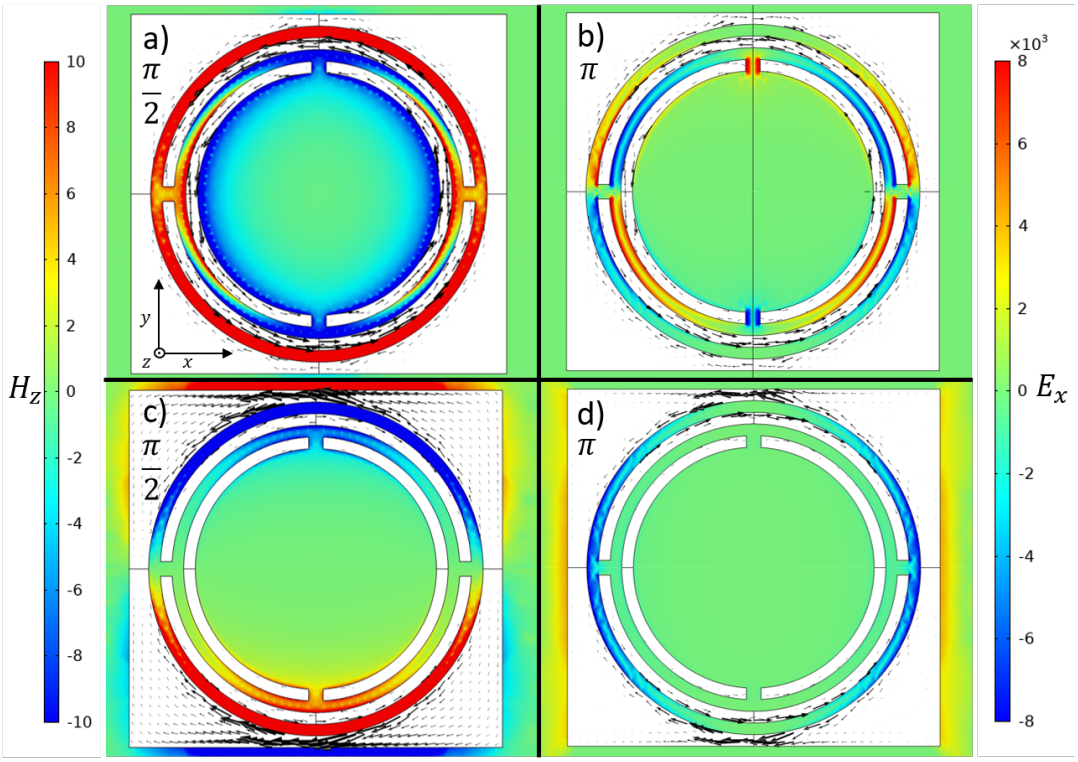

Figure 6.7: Plots of the simulated z component of the magnetic field (a,c) and the x component of Electric field (b,d) and surface current (black arrows) for the ring (a,b) and frame (c,d) modes at phases of $\frac{\pi}{2}$ and π. Areas of white are perfect electric conductor and both modes are at 1.36 GHz and k=353.86.

Figure 6.8 shows the simulated dispersions as the splits are rotated by 10°, 20° and 30° underlayed with the dispersion of the symmetric designs previously covered. Even at 10° there is a highly noticeable shift in the J-type mode when compared to the symmetric meta-molecule. This is due to weaker magnetic coupling as the magnetic dipole shifts to have an in-plane component (recall equation 3.29). However, splitting at the crossing point is hard to discern and less than the width of the measured mode in experiment. Similarly, at 30° the splitting is so marginal as to be likely imperceptible in a measurement. This is perhaps counter-intuitive as we would expect the net electric dipole induced by the symmetry breaking to increase with rotation, as it corresponds to putting a higher contribution of the two angled dipoles in the x direction. However, as the angle increases so too does the distance between the rotating splits and x-axis of the structure where the electric field of the frame mode is strongest, see figure 6.7d, and so the coupling between the two decreases. There are many other contributing factors to this feature, including counteracting charges between the outer and inner rings and the increased

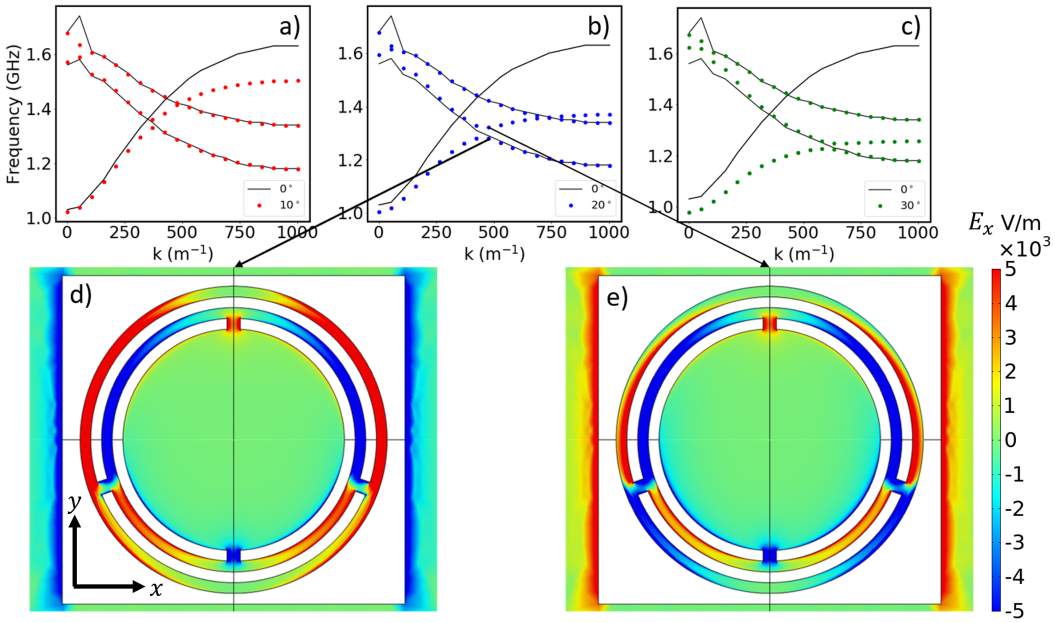

Figure 6.8: Dispersion plots for an infinite chain of combined meta-molecules structures as their outer splits are rotated down by 10° (a), 20° (b) and 30° (c). The underlayed black line shows the simulated dispersion of the symmetrical structure for comparison. The lower plots show the x component of the electric field for the lower (d) and upper (e) modes supported by the 20° structure at their crossing point of k=530 m^{-1}. Non-zero fields in the splits show that a net electric dipole has been created through this rotation.

field confinement at high k values, but it doesn't serve my purpose to go into them here. From this analysis a rotation of 20° was chosen and figure 6.8d-e show the x-component of the electrical field for the lower and upper bands respectively at the crossing point. It is of note that there is a small, non-zero and complementary field within the rotated splits as we had expected. Additionally, both show features from the field plots of both the H- and J-type modes, which was absent in the plots of figure 6.7, indicating a hybridisation indicative of a coupling interaction..

The experimental response from a chain of such meta-molecules, shown in figure 6.9 now exhibits coupling between the J- and H-type modes in the form of an anti-crossing, seen at 430 m^{-1} in figure 6.9. Of the two H-type modes from figure 6.6, here only one couples with the J-type mode. The H-type mode that does couple corresponds to the horizontally oriented mode, the vertical mode does not couple because it is now perpendicular to the net electric dipole created by the symmetry breaking. The data shown in figure 6.9 show that I have indeed been able to explore phenomena that have not been seen in molecular systems, highlighting the power of

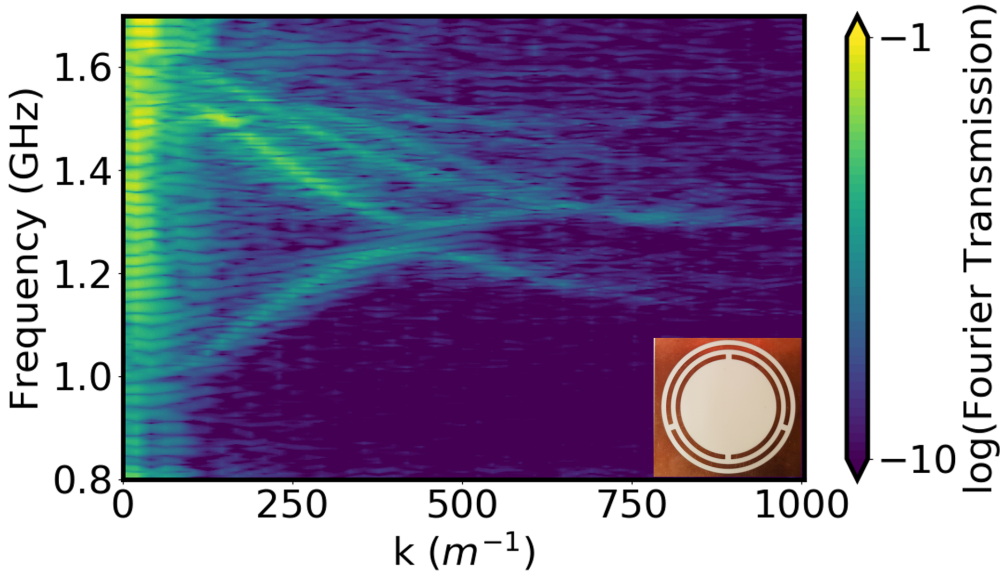

Figure 6.9: Dispersion for chains of the symmetry breaking double ring + frame meta-molecules with a single meta-molecule inset. Contour plots for the the asymmetric combined sample. The inclusion of a symmetry breaking rotation leads to a coupling between the J and H like modes, opening a band gap at 1.26 GHz. For the asymmetric sample both coupled modes have zero group velocity at 430 1/m. The high values (yellow regions) around $k \sim 0$ are due to direct transmission between the launch antenna and the probe antenna.

the meta-analogues approach.

6.4 Conclusion

In summary, I have established a number of designs of meta-molecules suitable for studying microwave analogues to molecular aggregates, based on split-ring resonators. I have shown that such meta-molecules may be assembled into 1D chains where the inter-molecular separation is substantially sub-wavelength. Using two different designs of meta-molecule I have separately shown J- and H-like aggregation behaviour. Further, by combining two meta-molecule designs into a more complex structure, I have shown that my 1D analogue can simultaneously support both forward and backward propagating waves. Finally, by introducing an asymmetry into the design of my meta-molecule, specifically by introducing a controlled amount of bianisotropy, I have shown that forward and backward propagating modes may interact so as to anti-cross on a dispersion diagram, introducing a geometry-dependent

stop-band in propagation along the chain. In terms of metamaterials, to the best of my knowledge, this is the first observation of simultaneous forward and backward propagating modes, one that may be of potential interest in RF applications such as power transfer [136].

Chapter 7

Edge States and Boundary Modes in a Metamaterial Analogue For Molecular Aggregates

One of the defining differences between artificially and naturally formed structures is the appearance of disorder in the latter. The previous chapter examined an ordered chain of resonators and likened it in behaviour to a molecular aggregate. In order to expand the analogy even further, this chapter will introduce defects into similarly constructed chains and examine them in the context of the Su, Schrieffer and Heeger (SSH) model, a model that was originally formulated to explain the modes supported by trans-polyacetylene. This chapter will experimentally demonstrate how the different chain termination and defect types found in trans-polyacetylene lead to edge states and disorder modes using the meta-atom structure. It will do this by matching the resulting field profiles from the metamaterial cases to those predicted mathematically.

7.1 Introduction

When presented with two structures, of similar design and purpose, anyone requested to identify which was grown and which manufactured would find a likely route to answering that question in the relative uniformity of the two samples. While manufactured structures tend towards a strict, designed, order, the results of nature's hand turned to the same task are often only semi-regular. Studies of natural processes must eventually consider the effects of this disorder in their systems if they are to explain them fully.

If the study of aggregate phenomena in the ideally ordered case was difficult on the molecular scale then studies of disorder, where systems cannot be fully explained by a single unit cell, become even more complex. Experimental investigations are typically constrained to probing consequences of near-field interactions in the far field [80], and even those techniques that are able to probe the near-field are not able to do so on the inter-molecular scale [66]. As a result the disorder in these systems, which is known to play an important role in, for example, exciton transport [31], can only be inferred rather than directly probed.

Fortunately, the increased difficulty of such studies due to scale has no equivalent effect when using a metamaterial analogue approach. I needn't adjust my physical components, only scale down what they represent. Indeed, in the case presented here I utilise the same components for my metamaterial as in chapter 6. Each elements goes from representing molecules, as in the previous chapter, to individual atoms with equal validity. It is the premise of this chapter that metamaterials, shown in the previous chapter to mimic aggregate behaviour in an ideally ordered case, can replicate the defect behaviour of aggregates. By directly comparing the defect modes of an aggregate like metamaterial with those predicted by the SSH model, explained in more detail in section 7.2, I further validate the power and value of the metamaterial approach to studying molecular aggregate properties.

I create a linear chain of meta-molecule resonators and, by structurally altering the order of this chain, I introduce defects that support localised modes. Subsequently, I directly probe the near-fields of these defect modes by employing

electrically-small near-field antennas, and compare my results to those predicted by the Su-Schrieffer-Heeger (SSH) model. For all of its wide applicability the SSH model was originally used to map the probability density of electrons along chains of polyacetylene, and to predict the effect of disorder in the properties of these chains [90].

7.2 The SSH Model

7.2.1 Introduction

Su, Schrieffer and Heeger had a problem back in 1979. Interest in semiconducting polymers, of which polyacetylene is one, was heating up fast. The benefits of doping in these substances was plain, in the introduction to their work they cite eleven papers focused on the topic, but to them even the undoped material was still not fully explained. Polyacetylene, in its *trans* form, consists of carbon atoms coupled via alternating single and double bonds. This alternating structure leads to a bandgap in the allowed electron probability distributions but experiments showed the presence of allowed states within the gap. Defects and solitons (solitary wave) were being blamed but the precise nature of them and how these naturally occurring defects might interact with the defect sites created by dopants was uncertain. They needed a model for these atomic chains that could tell them what the experiments of the day could not.

To this end they introduced a very effective toy-model that employs a tight-binding Hamiltonian to represent the alternating bonds of the trans-polyacetylene chain. The SSH model, as it became known, can be used to simulate the energies and field intensities in many systems of alternating harmonic resonators [90, 137], a generalised representation of which is shown in Fig. 7.1a.

With this model, the existence of non-propagating (appearing as a flat horizontal line in a dispersion diagram) soliton states were predicted (see section 3.4.2), states arising from phase changes due to the periodic carbon structure that could explain some of the substance's unique properties. These soliton states were both highly

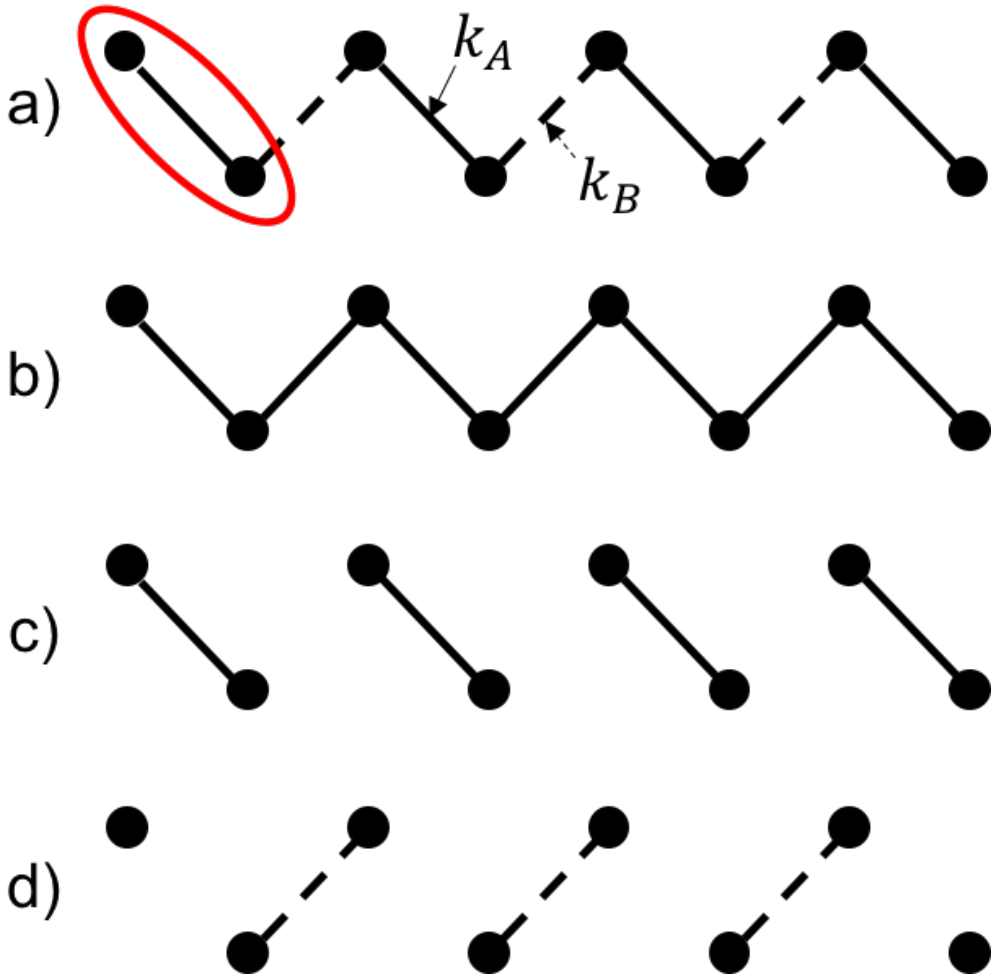

Figure 7.1: (a) A schematic of a chain of 8 resonators, each with a resonance frequency ω. Two resonators within a 'cell' are coupled together via an intra-cell coupling term k_A (red ellipse), with each cell in the chain being coupled to neighbouring cells via a second inter-cell coupling term, k_B. When $k_A \neq k_B$ the system deviates from the mono-atomic, single banded, case (b) and a bandgap will emerge in the dispersion of the chain. (c) In the dimer limit when $k_B = 0$ and $k_A \neq 0$ the chain consists of 4 isolated dimers. Each dimer will support two modes with frequencies that will lie above and below ω. The difference in frequency between them is determined by the magnitude of k_A. (d) In the other dimer limit, when $k_A = 0$ and $k_B \neq 0$, there are three isolated dimers, and in this case the difference in frequency between their modes is determined by k_B. In addition, there are two isolated resonators at each end of the chain. These isolated resonators will have resonance frequencies of ω, which lie between those of the dimers; i.e. within the bandgap. It is not just in the dimer limit that these "edge" modes appear, rather it is only necessary that $k_A < k_B$.

localised, existing over only a few atoms, and present within the chain's bandgap where they should have been forbidden, explaining the polymer's odd property. In 2016 Meier *et al.* directly observed the soliton in polyacetylene that had first been predicted in 1979 [138].

7.2.2 Theory

The SSH model has a significant degree of crossover in theory with the coupled chains of section 3.1. The key difference is that it concerns chains with some periodic variation in its resonators. In the mass and spring analogy this could be alternating the mass between two values, or alternating the spring constant of the coupling springs. This periodicity opens a bandgap, a region of frequencies between the lowest and highest allowed modes of the chain that are not themselves allowed modes. Figure 7.2a shows the mode frequencies against mode number for two spring-mass chains with the same average mass, but for the black line each resonator has the same mass and for the blue dots each mass alternates from a lower to a higher value. A bandgap has opened, splitting the periodic chain into an upper and lower band. This large, singular, bandgap is entirely due to the periodicity. If the varyingly sized masses are randomly arranged along the chain, as in 7.2b, no such bandgap appears.

Periodic Coupling Strengths

I will demonstrate a version of the SSH model here. The Hamiltonian in Eq. 7.1 represents a system of eight resonators, each of which has a resonance frequency ω, connected in a loop (represented by coupling terms in the bottom left and top right of the matrix). The resonators are coupled via two alternating nearest neighbour coupling terms of differing strength. This arrangement results in four 'cells', with k_A being the coupling between two resonators within the same cell (intra-cell coupling), and k_B being the coupling between the cells (inter-cell coupling).

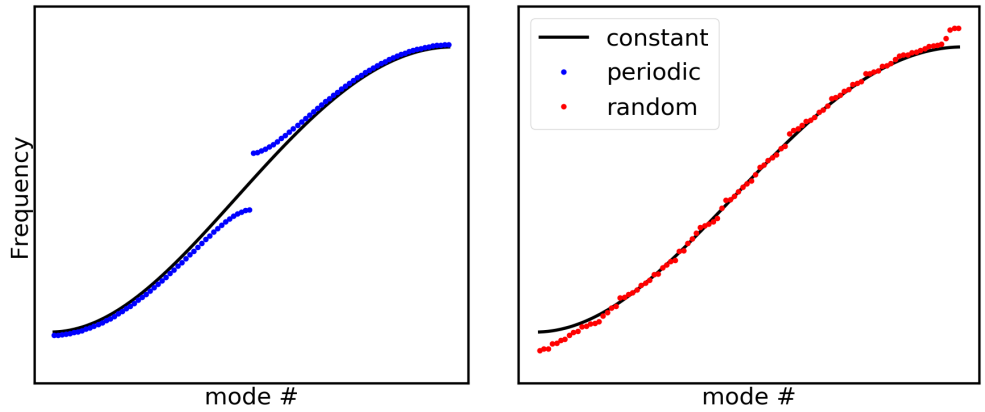

(a) (b)

Figure 7.2: Allowed modes for a chain of linearly coupled mass and spring oscillators 100 resonators long. Black line corresponds to a chain with the same average mass but no variation between each resonator. (a) The case where every other mass in the chain of oscillators is double that of the other masses. Note that a band gap has now opened in the system. This is due to the periodicity of the alternating mass structure. (b) The case where 50 masses are 110% the mass of the other 50 masses in the chain but their position is random along the chain. No bandgap has formed in the absence of periodicity

$$\hat{H} = \begin{bmatrix} \omega & -k_A & 0 & 0 & 0 & 0 & 0 & -k_B \\ -k_A & \omega & -k_B & 0 & 0 & 0 & 0 & 0 \\ 0 & -k_B & \omega & -k_A & 0 & 0 & 0 & 0 \\ 0 & 0 & -k_A & \omega & -k_B & 0 & 0 & 0 \\ 0 & 0 & 0 & -k_B & \omega & -k_A & 0 & 0 \\ 0 & 0 & 0 & 0 & -k_A & \omega & -k_B & 0 \\ 0 & 0 & 0 & 0 & 0 & -k_B & \omega & -k_A \\ -k_B & 0 & 0 & 0 & 0 & 0 & -k_A & \omega \end{bmatrix} \tag{7.1}$$

This Hamiltonian can be solved to obtain its eigenvalues (see section 3.1), which correspond to the frequencies of the resonances supported by the chain of resonators, and its eigenvectors, which correspond to the relative amplitude distribution along the chain for each of the eigenvalues. This chain is effectively infinite in appearance to any mode propagating along it, as it is a closed loop, and perfectly ordered. We can imagine switching the values of k_A and k_B with no effect on the chain's eigenvalues or vectors. However, if we break the loop by eliminating the k_B coupling

term between the first and last resonator then one thing does change when we make such a transformation, the terminations of our newly finite system. In short, does the chain end with a complete cell, k_A termination, or a partial cell, k_B termination.

$$\hat{H} = \begin{bmatrix} \omega & -k_A & 0 & 0 & 0 & 0 & 0 & 0 \\ -k_A & \omega & -k_B & 0 & 0 & 0 & 0 & 0 \\ 0 & -k_B & \omega & -k_A & 0 & 0 & 0 & 0 \\ 0 & 0 & -k_A & \omega & -k_B & 0 & 0 & 0 \\ 0 & 0 & 0 & -k_B & \omega & -k_A & 0 & 0 \\ 0 & 0 & 0 & 0 & -k_A & \omega & -k_B & 0 \\ 0 & 0 & 0 & 0 & 0 & -k_B & \omega & -k_A \\ 0 & 0 & 0 & 0 & 0 & 0 & -k_A & \omega \end{bmatrix} \tag{7.2}$$

Disregarding cells for a moment, the true crux of the issue is in the relative strength of the two coupling terms. Terminations are a kind of defect in periodic systems as they are a deviation from the defining periodicity i.e. an end to it. With the matrix 7.2 we will consider two cases: 1) where $k_A > k_B$, and 2) where $k_B > k_A$. The case of $k_A = k_B$ is trivial and corresponds to that of a mono-atomic chain and is not of interest here (see Fig. 7.1b for a visualisation and section 3.1 for analysis of this structure).

To gain some physical insight we begin by considering the limits of $k_A > k_B = 0$ and $k_B > k_A = 0$, these are the so called 'dimer limits' where the chain consists of a series of non-interacting dimers. In the $k_A > k_B = 0$ dimer limit we find just two distinct resonance frequencies, the higher and lower energy modes of each of the four dimers in our chain, see Fig. 7.1c, with the difference in energy between them being determined by the strength of the intra-cell coupling and each being four-fold degenerate. The case when $k_B > k_A = 0$ is a little more interesting. Here we find three dimers within the body of the chain, but in addition we now have two independent resonators at the ends of the chain (see Fig. 7.1d). These independent resonators will have a resonance frequency of ω, which will lie between the resonance

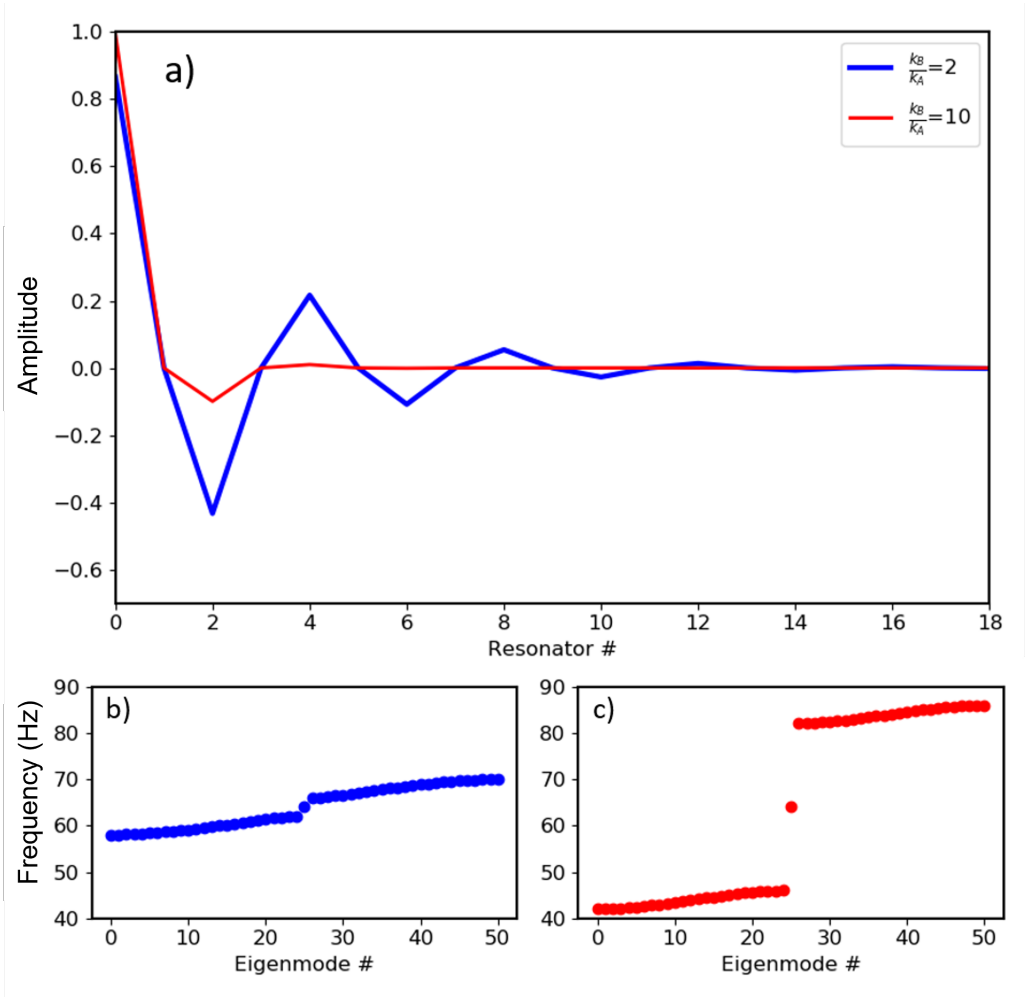

Figure 7.3: Plotted eigen-vectors (a) and eigen-modes (b-c) for an SSH model with different ratios of $\frac{k_B}{k_A}$. The Eigen-vectors plotted in panel (a) are of the mid bandgap defect mode for the two ratios that forms at the termination of the chain. Increasing the ratio from 2 to 10 leads to a significant increase in the localisation of the mode as it becomes more difficult for that mode to penetrate into the bulk. Panels (b) and (c) show the eigen-modes plotted in ascending frequency order for the two chains. Where the ratio is 2 (b) the band gap is very small but increasing the ratio to 10 widens that gap without changing the eigen-mode of the defect.

frequencies of the dimers, i.e. within the bandgap, as much as can be said to exist in such an extreme where all modes are localised and no propagating 'bands' truly exist.

If we move away from the dimer limit by increasing the intra-cell coupling, k_A, the localisation of the dimer modes is removed, resulting in a discrete set of modes that are supported by the entire chain. However, the localised modes at the terminations remain within the bandgap – all reintroducing k_A has done is to change the degree of localisation, which decreases as the coupling terms approach parity, along with the size of the bandgap, which increases linearly with $\frac{k_B}{k_A}$ (assuming a constant k_A) in

this simple model. This effect can be seen in Figure 7.3. Of important note is that the degree of localisation is dependent only on the ratio of the coupling terms whilst the magnitude of the bandgap is more complicated, and depends on the individual resonator frequencies and both coupling terms.

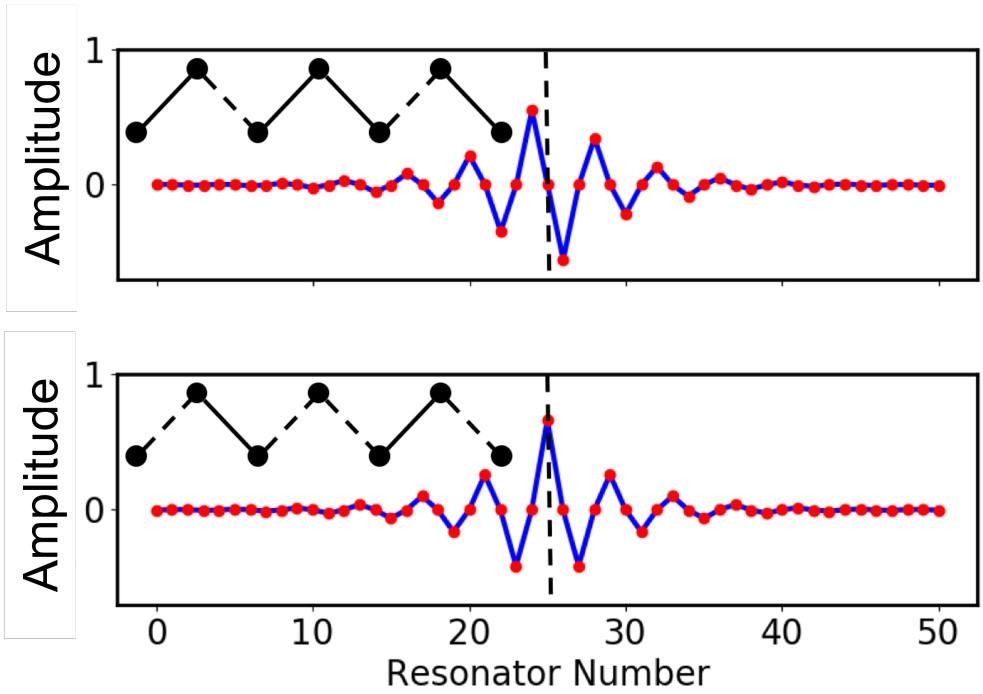

Figure 7.4: Top: Calculated eigenvector of a fifty resonator long chain in which the relative strengths of k_A and k_B are switched midway along the chain such that the resonator at the boundary is strongly coupled to both its nearest neighbours. This boundary mode has an asymmetric form. Bottom: The same as the top figure, but in this case the position of the switch occurs such that the resonator at the boundary is weakly coupled to its neighbours. In this case the boundary mode is symmetric. Boundaries in both cases are marked by the vertical black dashed line.

It is not just the terminations of the chain that can support localised modes, defects can also be introduced into the bulk of the chain. Consider a case where, part way along a chain, we switch the relative magnitudes of k_A and k_B such that we have $k_A > k_B$ on one side of a resonator and $k_B > k_A$ on the other. Depending upon whether we perform this switch at the site of a k_A or a k_B we get two distinct cases, one where the resonator at the boundary is strongly coupled to both its nearest neighbours, and one where it is weakly coupled to its nearest neighbours, see the insets of Fig. 7.4. If we calculate the eigenvalues for both cases we can identify localised modes centred at the boundaries where the switch occurs, which once again

have frequencies that occur within the bandgap. However, the eigenvectors for the two cases show distinctly different behaviours, as shown in Fig. 7.4. In the case where the resonator at the boundary is strongly coupled to both its nearest neighbours, that resonator will have zero amplitude (I will call this the 'asymmetric' boundary case based on the shape of the field amplitudes), whereas when the resonator at the boundary is weakly coupled to its neighbours it has maximum amplitude (the 'symmetric' boundary case). These two cases can be directly related to the soliton and anti-soliton states of polyacetylene [139].

Periodic Element Frequency

So far we've only examined the effects of changing inter-element coupling on the SSH model, and this is largely what it is used for, but the incorporation of metamaterials and their ever-malleable parameters allows us to explore further. Specifically, we can also see how alternating the resonance frequency of the resonators, in the same manner as we have coupling previously, induces boundary modes.

$$\hat{H} = \begin{bmatrix} \omega_p & -k & 0 & 0 & 0 & 0 & 0 & -k \\ -k & \omega_a & -k & 0 & 0 & 0 & 0 & 0 \\ 0 & -k & \omega_p & -k & 0 & 0 & 0 & 0 \\ 0 & 0 & -k & \omega_a & -k & 0 & 0 & 0 \\ 0 & 0 & 0 & -k & \omega_a & -k & 0 & 0 \\ 0 & 0 & 0 & 0 & -k & \omega_p & -k & 0 \\ 0 & 0 & 0 & 0 & 0 & -k & \omega_a & -k \\ -k & 0 & 0 & 0 & 0 & 0 & -k & \omega_p \end{bmatrix} \tag{7.3}$$

Using a fifty one element version of equation 7.3 (note the boundary highlighted in red) we can then sweep ω_a from 0.2 ω_p through to 1.8 ω_p to get the plot in figure 7.5 where black dots mark modes that are extended along the chain. The defect mode within the bandgap has been plotted in red, with Fig. 7.5a showing the eigenvector for a defect mode where $\omega_a < \omega_p$ and Fig. 7.5b showing the same for an $\omega_a > \omega_p$ case. Note that, much like the eigenvectors shown in figure 7.4, there is a

symmetric and an asymmetric mode which is dependent on the ratio between the periodic elements of the chain (in that case coupling strength but here frequency).

Despite sharing a symmetry these frequency defect modes are noticeably different in form to their coupling defect counterparts, primarily that elements 25 and 26 (the elements at the defect that share a frequency) both have maximum displacement. In the coupling case this only occurred for the symmetric mode, with the asymmetric mode having a node at its boundary element. This is not surprising when we consider that, for this frequency alternating case, the boundary in the chain falls between two resonators as opposed to on a resonator. Resonators on either side of the boundary are then displaced symmetrically or asymmetrically accordingly and identically.

From this examination of the SSH model, we have identified five distinct localised modes that could be supported by our aggregate-like metamaterial chains: an "edge" mode when the coupling between resonators in a cell is weaker than the coupling between cells, and two "boundary" modes each for chains alternating either coupling strength or element frequency that change phase at some boundary. Each of these boundary modes has a different form that depends upon the nature of the boundary elements relative to the rest of the chain. In the following, I will discuss the designs of our analogues, and report measurements that directly probe the forms of these three types of localised modes.

7.3 Chain design

In order to replicate the SSH model thoroughly I will perform two studies using two different chains, the periodic coupling study will measure the boundary modes in a metamaterial chain with periodically alternating coupling terms k_A and k_B, whilst the periodic frequency study will do the same with a different chain that alternates resonator frequencies ω_a and ω_p. It should be noted that, whilst in these studies either coupling or resonator frequency will dominate their respective chain's behaviour, there will be elements of both periodicities present. As discussed in Chapter 5 the frequency periodicity study must contend with the changing in coupling between resonators of different frequencies, and the differing environments

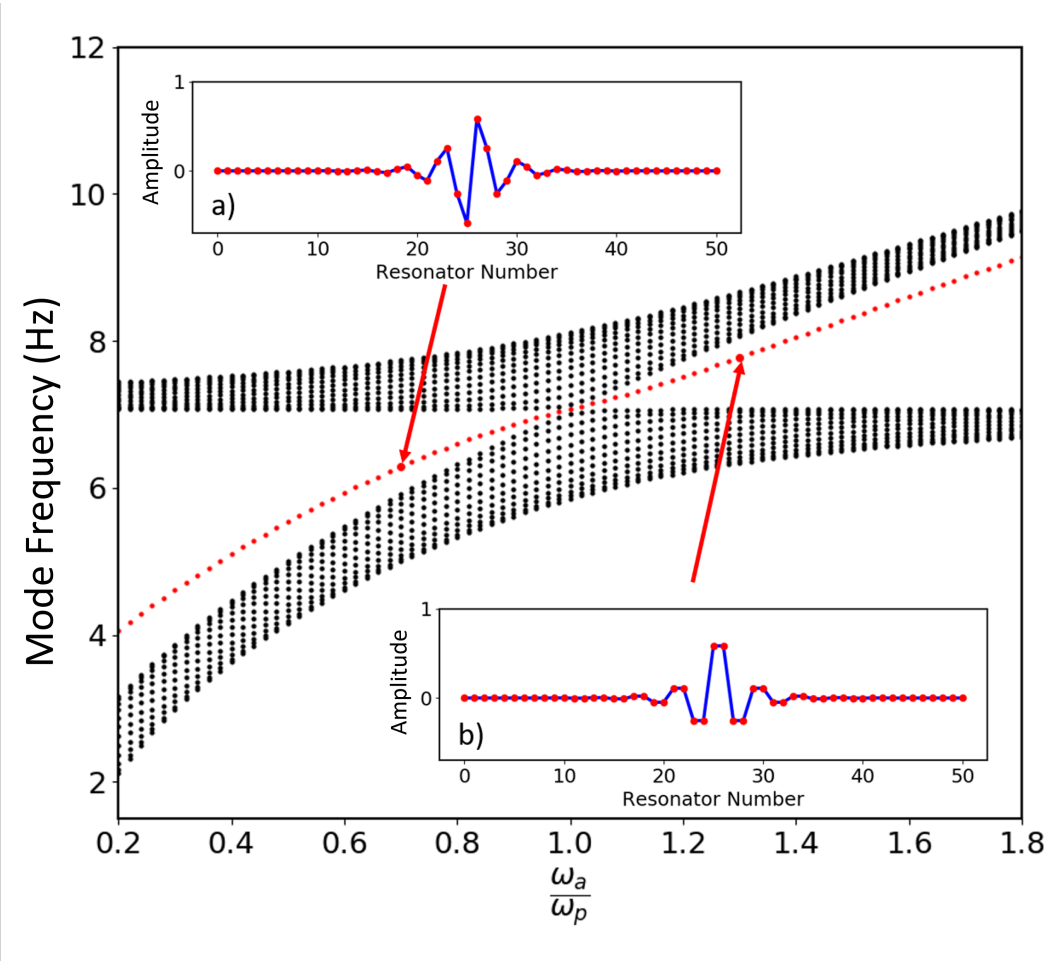

Figure 7.5: A plot of the modes for a chain of 51 resonators modelled using the SSH model, alternating ω_p to ω_a for the first 26 resonators and ω_a to ω_p for the final 25, as the frequency of one of the elements, ω_a is tuned through the frequency of ω_p. The black dots correspond to non-localised modes of the chain that extend across its length. The mode corresponding to the defect at the transition point is plotted in red whilst the bulk modes are plotted in black. The insets show a) the asymmetric eigenvector for the defect mode when $\frac{\omega_a}{\omega_p} = 0.7$ and b) the symmetric eigenvector corresponding to $\frac{\omega_a}{\omega_p} = 1.3$.

required to change coupling strength in the coupling study will also have an effect on resonator frequency. As a result, greatly disparate meta-atoms are used for each study. Their design and chain arrangement are discussed in the following.

Periodic Coupling Strengths

The meta-molecule design used in this study is the same non-bianisotropic SRR as that used in chapter 6, pictured in Fig. 7.7a. See section 6.2 for more details on how that meta-molecule was designed and manufactured. Of importance here is that the lowest order resonance frequency of a single resonator symmetrically bounded by

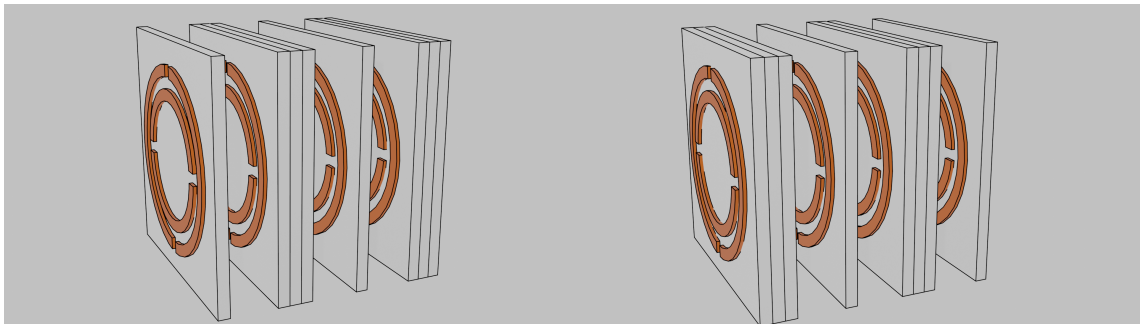

(a) ABAB

(b) BABA

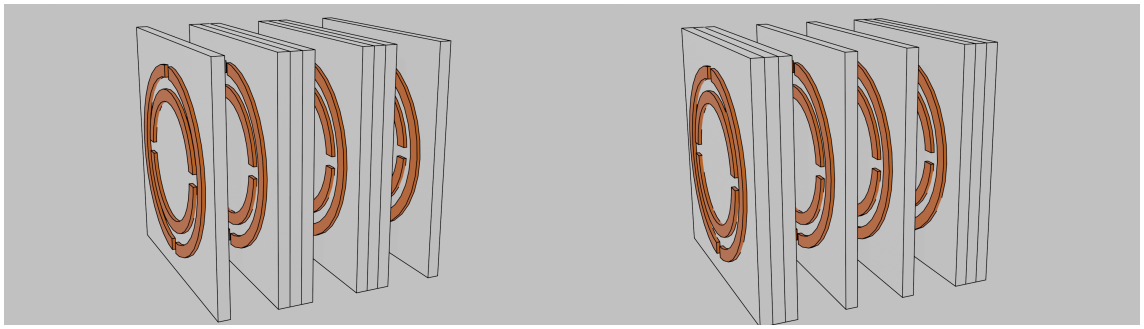

(c) ABBA

(d) BAAB

Figure 7.6: Exploded schematics of the four chain formations where A refers to copper (orange) and a dielectric spacer (white) whilst B refers to copper and three dielectric spacers. a) formation that supports no edge mode. b) Formation that supports an edge mode. c) A boundary formation that supports a symmetric boundary mode. d) A boundary formation that supports and asymmetric boundary mode.

the substrate material was 1.40 GHz.

To form my chains I stacked the resonators axially, whilst altering the inter- and intra-cell coupling strengths by inserting additional blank substrates (without any copper layer) in appropriate positions. Figure 7.3 shows how a high ratio of $\frac{k_B}{k_A}$ is important for making the defect mode as localised as possible. With this as a consideration, no additional spacer was added between the strongly coupled resonators. This element will be referred to as A in following schematics of Figure 7.6. On the other hand, the B component of the cell was a resonator with two spacers behind it.

These building blocks were then combined into the chains used for the following four experiments: two chains to investigate edge modes with $k_A > k_B$ and $k_A < k_B$, and two chains to investigate symmetric and asymmetric defect (boundary) modes when sub-chains with switched values of k_A and k_B are joined together. Each chain consisted of 94 resonators. See Figure 7.6 for details of the formations of each chain.

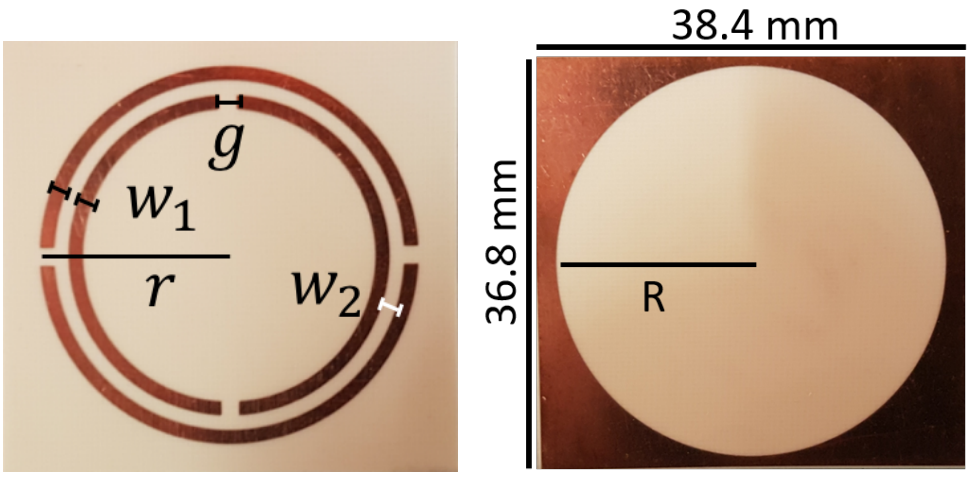

(a) (b)

Figure 7.7: The meta-molecules used in this study are based on the split-ring resonator, a), and a rectangular patch with a circular hole in it, b). Dark regions correspond to copper-coated areas of a dielectric substrate, light regions correspond to the bare substrate. a) r=16 mm, $w_1 = w_2$ =1.2 mm and g=1.5 mm. b) R=17.2 mm

Periodic Element Frequency

For this study I used the frame-only meta-atom design, also covered previously in chapter 6. A single frame resonator with the dimensions in figure 7.7b has a lowest order resonance frequency of 1.94 GHz. When paired with a second frame resonator, however, it doesn't couple to produce two separate resonances. Rather, the pair of frames become capacitively linked and act as a single resonator, with the new resonance frequency being determined by the size of the frame, the dielectric constant of the spacer, and the spacing between the frames.

With this in mind I designed two resonators, a 1.55 mm thick substrate bounded on both sides by a frame, with a resonance frequency of 1.14 GHz; and three sections of substrate, totalling 4.65 mm, also bounded by frames, with a resonance frequency of 1.31 GHz. These elements, C and D respectively, form a single cell of the periodic chain. Each chain was made up of 32 resonators and schematics of each in the vicinity of the two sub-chain boundaries is depicted in figure 7.8.

7.4 Methods

All measurements were conducted using an Anritsu Vectorstar MS4644A Vector Network Analyser (VNA). To excite any modes supported by my chains with $k_B > k_A$ and $k_B < k_A$ a small loop antenna, resonant far from the spectral range of interest, was placed at one end of the chain adjacent to one of the splits in the rings. The near-fields of the excited modes were then probed using a second loop antenna that was swept along the length of the sample while measuring the transmission (S21) between the exciting and probing antennas, see Fig. 7.9a. The dimensions of the antennas were such that, at the frequencies studied here, they were far from resonance and minimally perturbed the modes of the chains. The magnitude of the power transmission between the antennas was measured as a function of position along the chains over the frequency range 1.2 to 1.8 GHz.

To probe the boundary modes, I needed to alter my experimental set up somewhat since any mode localised in the bulk of the chain will not be excited by an antenna placed at one end. Instead I sweep the two antennas in tandem along opposite sides of the chain, see bottom of Fig. 7.9b, whilst recording the transmission between them as a function of distance and frequency.

For the frequency alternating chains the same method was used again but making use of straight wire antennas for both probes, that can detect and excite electric modes, instead of loop antennas as depicted in Fig. 7.9b. Both antennas were

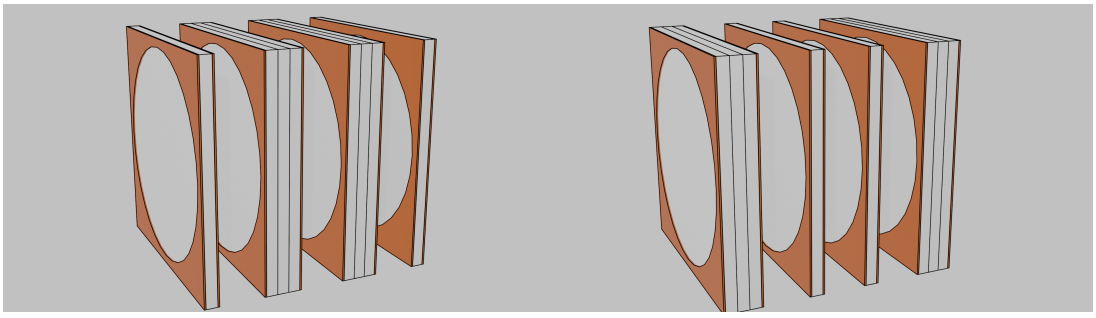

(a) CDDC (b) DCCD

Figure 7.8: Exploded schematics in the vicinity of the boundary between sub-chains in a frequency alternating chain with low, C, and high, D, frequency elements. Each element is made up of an amount of substrate, white, bounded by copper, orange. a) A boundary to produce a symmetric boundary mode and b) a boundary to produce an asymmetric boundary mode.

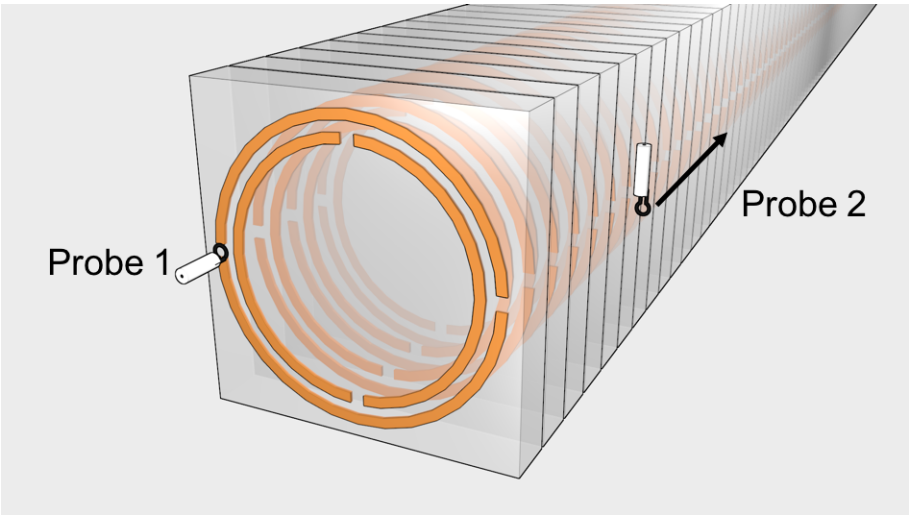

(a)

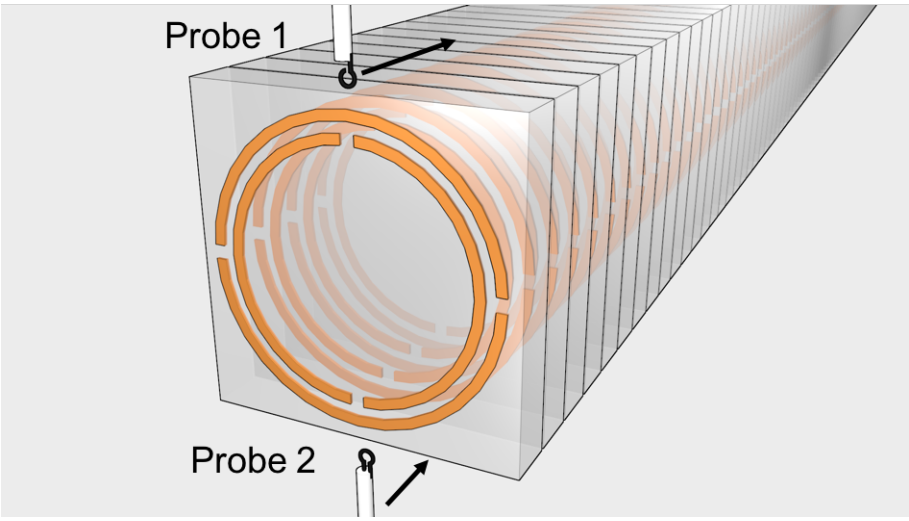

(b)

Figure 7.9: A schematic of the two methods used to detect localised modes within a chain of resonators. In both, Probe 1 is the exciting antenna and Probe 2 is the receiving antenna. Black arrows indicate which Probes are scanned as part of the measurement. a) The scanning method for probing edge modes uses a loop antenna (Probe 1) placed at a split on the outer ring of the first resonant element so as to excite the modes of the chain. The loop was orientated in the plane of the resonator. A second loop antenna (Probe 2) was scanned along the edge of the chain with the same loop orientation. The transmission between the two antennas was measured. b) The scanning method for probing localised modes within the bulk of the chain. Two loop antennas (Probes 1 and 2) are scanned in tandem along opposite edges of the chain, and the transmission between them measured.

orientated to point towards each other across the chain, aligned to its central axis and parallel to its longest side so as to detect the lowest order mode only.

7.5 Direct Observation of Edge States

In Fig. 7.10a I show the transmission data for the chain with $k_A > k_B$. Note that the transmission is shown for only the first 60 mm of the 290 mm long chain. At low frequencies the chain supports collective modes that are distributed along the entire length of the chain. These appear as long-range oscillations in the transmission as a function of distance. As the frequency is increased the wavelength of these collective modes becomes shorter, until a band gap is encountered at approximately 1.4 GHz. This bandgap extends to 1.65 GHz, beyond which oscillatory modes become evident once again. Within the band gap there is some direct transmission between the two antennas, but no transmission mediated via modes of the chain (There is no periodicity in the fields along the chain axis). No localised mode at the end of the chain within the band gap is observed, as expected when $k_A > k_B$.

In Fig. 7.10b I show equivalent data for the case where $k_B > k_A$. The data look very similar to those in Fig. 7.10a, except that in this case there is a clear mode within the band gap, at 1.52 GHz, that decays into the chain, as predicted by the SSH model. The mode's rate of decay is governed by multiple factors. As discussed previously in section 7.2, this can be tuned by altering the resonance frequency of the end resonator, or by decreasing the difference between k_A and k_B and partially closing the bandgap.

In Fig. 7.11a I show the transmission data for the chain design depicted in Fig. 7.6c. Note that I am only presenting data over a relatively narrow range of frequencies and distances as compared to Fig 7.10 so as to identify more clearly the boundary mode, which is evident as a localised oscillation at a frequency of 1.42 GHz, within the band gap of both sub-chains. The data presented here are markedly different to those shown in Fig. 7.10, and this is a result of the different measurement set-ups. Firstly, there is significant direct transmission between the antennas giving a much larger background transmission. Secondly, as opposed to observing maxima

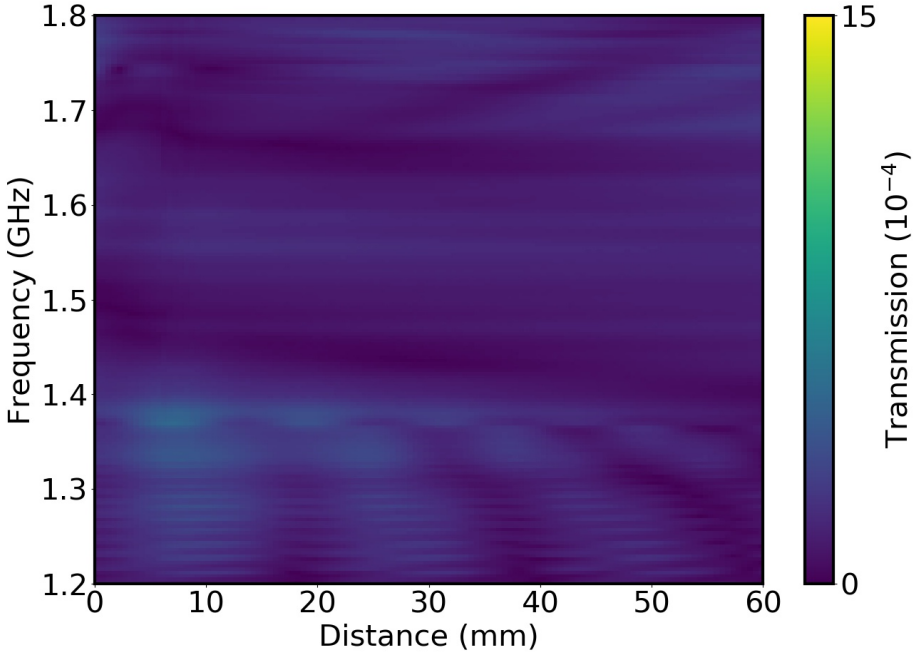

(a)

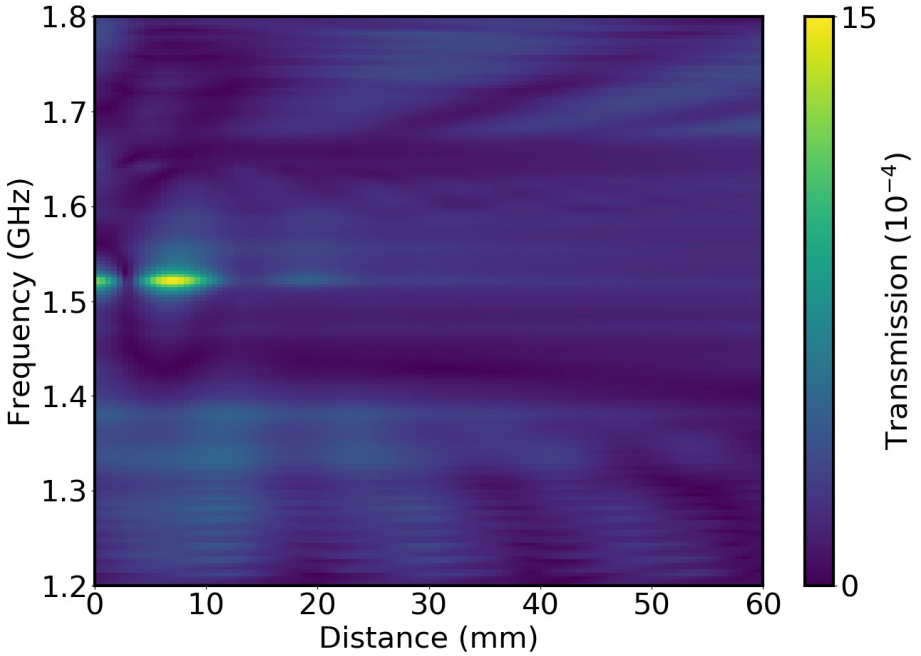

(b)

Figure 7.10: (a) The magnitude of the transmission between the exciting and probing antennas as a function of frequency and distance along a 60 mm section at one end of a chain with $k_A > k_B$. Collective modes of the entire chain are evident as oscillations in the transmission with distance for frequencies above and below the band gap (between 1.38 and 1.65 GHz). No modes are evident within the band gap. (b) The same as (a), but with $k_B > k_A$. In this case a localised mode confined to the end of the chain within the band gap occurs at 1.52 GHz. In both plots light green is used to show areas of high transmission while dark blue shows areas of low transmission. For both a change from maximum to minimum represents a 100% change in magnitude.

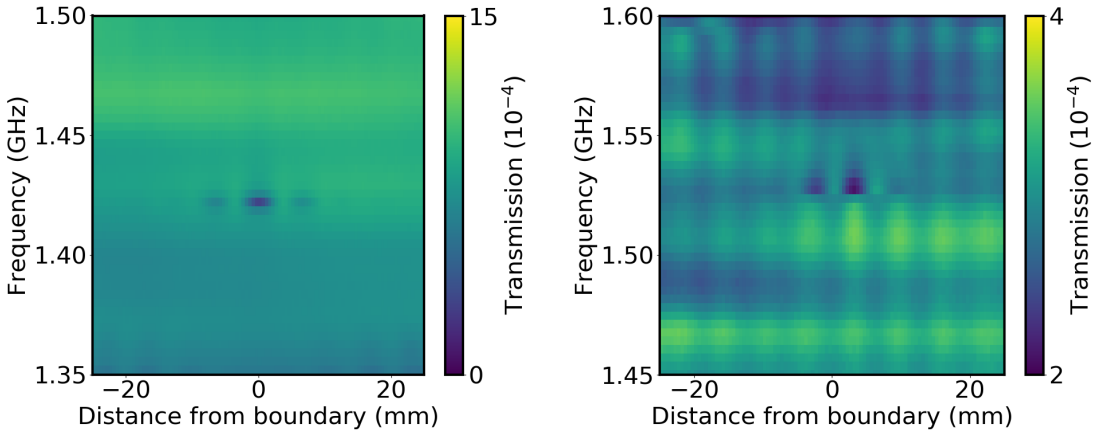

(a) (b)

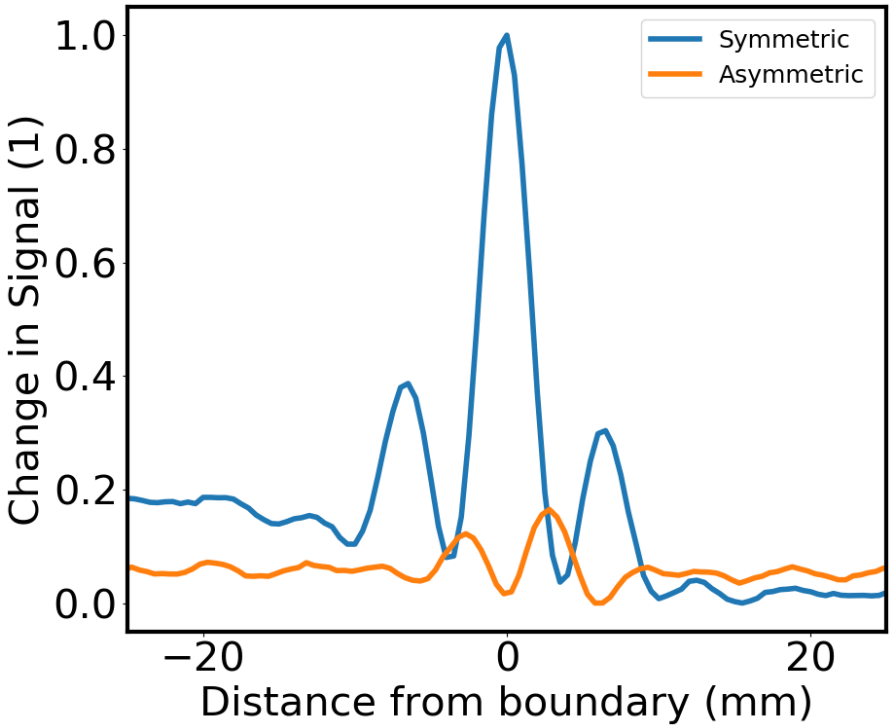

(c) Periodic coupling strength

Figure 7.11: (a) The magnitude of the transmission between the exciting and probing antennas as a function of frequency and distance along a chain that supports a symmetric localised mode at the boundary between sub-chains with $k_A > k_B$ and $k_A < k_B$. The mode is observed as a localised oscillation in the transmission at the boundary at a frequency of 1.42 GHz. (b) The same as (a) but for a chain that supports an asymmetric localised mode. In this case the localised mode occurs at a frequency of 1.526 GHz.. In both plots, light green is used to show areas of high transmission while dark blue shows areas of low transmission. For (a), a change from maximum to minimum represents a 100% change in magnitude while for (b) the same colour shift is only a 62% change in magnitude. (c) The absolute value of the change in the transmission for the two modes (symmetric at 1.42 GHz; asymmetric at 1.526 GHz) demonstrating the different symmetries. (Note that background slopes in the data for c) have been removed here for clarity).

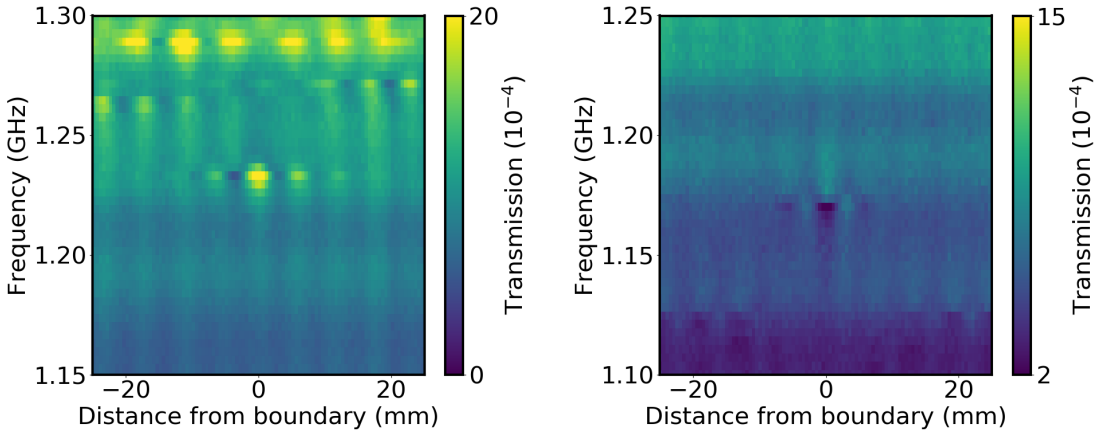

(a) (b)

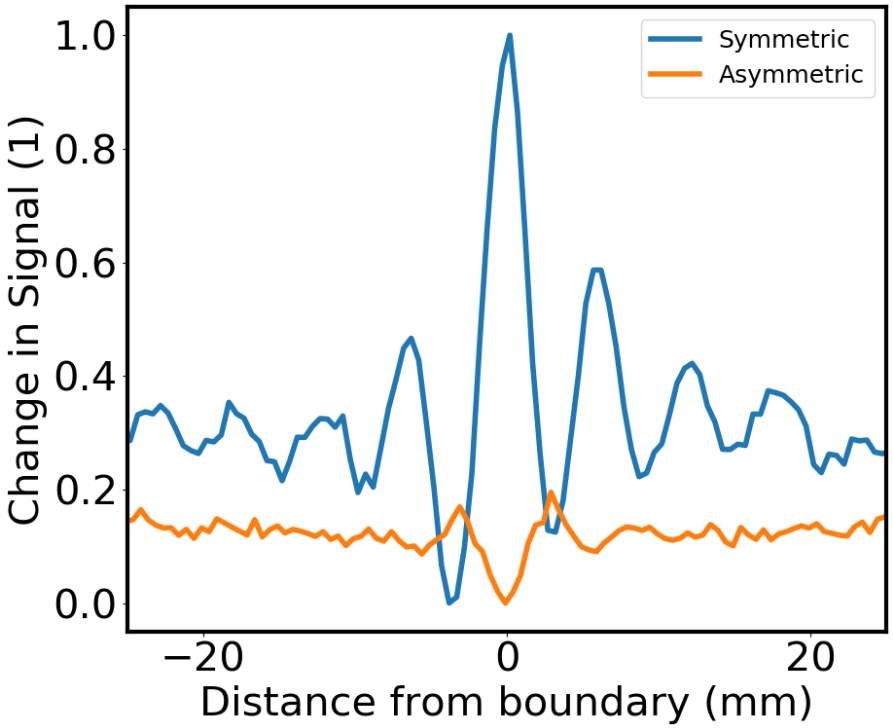

(c) Periodic element frequency

Figure 7.12: (a) The magnitude of the transmission between the exciting and probing antennas as a function of frequency and distance along a chain that supports a symmetric localised mode at the boundary between sub-chains with $\omega_A > \omega_B$ and $\omega_A < \omega_B$. The mode is observed as a localised oscillation in the transmission at the boundary at a frequency of 1.23 GHz. (b) The same as (a) but for a chain that supports an asymmetric localised mode. In this case the localised mode occurs at a frequency of 1.17 GHz. In both plots, light green is used to show areas of high transmission while dark blue shows areas of low transmission. For (a), a change from maximum to minimum represents a 100% change in magnitude while for (b) the same colour shift is only a 96% change in magnitude. (c) The absolute value of the change in the transmission for the two modes (symmetric at 1.23 GHz; asymmetric at 1.17 GHz) demonstrating the different symmetries. (Note that background slopes in the data for (c) have been removed here for clarity).

in the transmission as evidence of a mode, here we see minima. This is a result of energy that would have been transmitted directly between the antennas now being coupled into the mode and thereby lost to absorption. Thirdly, the measurement effectively rectifies the signal as a result of the antennas being swept in tandem.

Whilst the observation of the predicted symmetric mode is pleasing, I have to note a disparity between my results and the predictions of the SSH model. The SSH model, as described previously, predicts that the symmetric boundary mode should appear at the midpoint of the band gap, whereas in my experiment it is observed at a reduced frequency, closer to the lower energy band edge. In the simple SSH model all resonators are treated as identical with only the coupling strength between them altering. However, our system is rather more complex, with the resonance frequency of an oscillator being determined not only by its structure but also by its environment. In all other cases along the chain each resonator has one neighbouring resonator in close proximity (one spacer away) and one that is more distant (3 spacers away). However, in the present case the resonator at the boundary between the sub-chains has no neighbouring resonator nearby with both adjacent resonators being 3 spacers away. This results in the mode occurring at a lower frequency. However, I do not think this harms the validity of the metamaterial comparison. Gap states in true polyacetylene, and other soliton supporting structures, also appear asymmetrically within their associated band gaps [139–142].

In Fig. 7.11b I present similar data, but for the chain that was designed to support an asymmetric boundary mode. Once again, a localised oscillation is observed at the boundary between the sub-chains and, as expected, the mode occurs at a frequency of 1.52 GHz (in the middle of the band gap). To confirm the difference in symmetry of the boundary modes supported by my two chains, in Fig. 7.11c I present the normalised absolute value of the change in transmission as a function of distance from the boundary for both cases. Note that background slopes in the data have been removed for clarity. Comparison between the traces in Fig. 7.11a-b and the eigenvectors in Fig. 7.4 show that these two features are well matched in form with those predicted by the SSH model. That is, in the symmetric boundary case the

fields are concentrated around the central resonator at the boundary, whilst in the asymmetric case the central resonator is at a null. The apparent symmetry of the asymmetric mode is due to the rectifying effect of the measuring method; it can detect the presence of the mode but phase information is lost.

Finally, in Fig. 7.12 I show the equivalent results for the chains depicted in Fig. 7.8. My results show the symmetric, at 1.23 GHz, and asymmetric, at 1.17 GHz, boundary modes that were predicted by the SSH model. In contrast to the periodic coupling strength case, their appearance at different points within the bandgap is also a predicted feature of the SSH model when the resonator frequency is being alternated. Fig. 7.5 shows how the symmetric mode, when two low frequency resonators meet at the boundary, will approach the lower energy band and vice versa for the asymmetric mode.

7.6 Conclusions

In this chapter I have directly observed two classes of defect modes in molecular aggregate-like metamaterial chains at microwave frequencies – an 'edge mode' localised at the ends of the chain, and 'boundary modes' localised at the boundary between sub-chains of differing design. I have taken advantage of the cm scale structures to probe the modes at a resolution deep within their near-fields. For the edge mode I found the presence or not of the mode to be dependent on the inter- and intra-cell coupling terms. For the types of boundary mode in a chain with periodic coupling terms, a weakly coupled defect leads to a symmetric mode whilst a more strongly coupled defect results in an asymmetric one. I have also considered defects in a chain of periodically alternating resonance frequencies where a boundary between sub chains that results in two low resonance frequency resonators being adjacent produces a highly localised asymmetric mode, whereas if the boundary is located between two high resonance frequency resonators the boundary mode is symmetric. I have compared these results to predictions based on a simple Su, Schrieffer and Heeger (SSH) model, showing qualitative agreement between the two.

The results of this chapter further demonstrate the capability of metamaterial

analogues to mimic molecular aggregates, allowing the physics that underpins their behaviours to be explored in ways not possible in molecular systems. This work has shown how the symmetry of a defect mode can alter its resonance frequency, an observation that could be used to extrapolate the nature of disorder in an aggregate where the form of a defect may not be directly observed.

Chapter 8

Aggregate-like Cavity-Molecule Coupling using Microwave Resonators

The meta-analogue approach presented thus far has been used to replicate and probe molecular and atomic structures in a manner that their true form, and scale, would not allow. In the final step for this thesis I will take the analogy a step further and duplicate the results from a common molecular aggregate/strong coupling experiment. Subsequently I will, as before, exploit the increased scale and tunability of the meta-analogue approach to interrogate deeper within the phenomena presented. In previous chapters, however, I have simply reiterated the results of more arduous experimental work as a proof of the meta-analogue concept's validity. Here, I will demonstrate an entirely novel observation; the direct observation of a hybrid state between light and metamaterial, a meta-polariton.

In this chapter I will show that meta-molecules placed inside a microwave cavity may exhibit strong coupling, and show that near-field radio-frequency techniques allow us, for the first time, to probe the response of individual meta-molecules under strong coupling conditions.

8.1 Introduction

When a pair of resonators are coupled each resultant mode will be a mixture of the two, with the degree of mixing being dependent on their relative energy and coupling strength. Chapter 5 is a great example of this mixing. When the two rings studied in that chapter are tuned apart in frequency they approach their uncoupled counterparts. From this it is tempting to consider that the coupling must also be decreasing but I was able to show that this is not the case. Rather, it was the degree of mixing between the resonators that was reducing. When they are greatly disparate the higher energy mode has nearly all of its current and field focused in and around the higher energy ring, resulting in a mode that is near identical to that ring oscillating alone with the same applying in this case for the lower energy ring. When both rings are similar in energy then each of the system's two modes included oscillations in both rings of similar magnitude. We can imagine looking at both rings from a distance and identifying aspects of both rings' field character from their radiation. This combination of features wouldn't be overly dramatic, they are both SRR's after all, but it would be present. So what happens when we mix together resonators with very different make ups and character, a resonator of photons and one of matter? In such a case the same thing would happen, a photon mode and a material excitation coupled together in the strong coupling regime (see subsection 3.4.3) will mix together. The resultant hybrid is a type of quasi-particle known as a polariton (see subsection 3.4.2).

The formation of polariton modes due to the strong coupling of light and matter has led to exciting developments in physics, chemistry and materials science. Polaritons inherit characteristics of both the light and the matter from which they are formed. The potential to radically modify the properties of molecular materials by strongly coupling the molecules to a confined light field is so far-reaching that a new field known as 'polariton chemistry' is now emerging [39–44]. Molecular aggregates are of particular interest to this new field as their sharp absorption feature makes them easier to push into the strong coupling regime. However, the molecular scale of

the materials involved make probing strong coupling at the individual resonator level extremely challenging. As such, analysis of the forms polaritons take and how they might be better exploited is limited. The meta-analogue approach is thus perfectly suited to the task.

8.2 Typical Aggregate study

It is useful to briefly summarise what is involved in a typical experiment in the optical regime, as it is this I seek to replicate. Figure 8.1a is a schematic of such a system; the cavity in this case is formed of two planar metallic mirrors and the molecules are located between the mirrors, usually by being doped into an inert host (not pictured). In a typical experiment the interaction between the optical cavity mode and the molecular transition is revealed by looking at the transmission of light through the combined structure as a function of energy (frequency) and the in-plane wavevector of the light (the in-plane wavevector is related to the angle of incidence (θ) through $k_{\|} = 2\pi/\lambda \sin(\theta)$). Figure 8.1b shows a simulated set of such data in the form of a dispersion plot, Figure 8.1c shows a corresponding set of experimentally acquired data.

On their own the cavity mode and the excitonic transition behave quite differently. The excitonic transition has no propagating mode; its energy is independent of the incident angle, as indicated by the dash-dot white line in Figure 8.1b. The cavity mode on the other hand is dispersive; its energy increases (i.e. the mode blue shifts) as the angle of incidence increases, as indicated by the dashed white line in Figure 8.1b. Most importantly, the modes of the combined structure, indicated by regions of high transmission (yellow/green areas in the colour plots), are very different from those supported by the constituent elements.

When the transmission through the molecule-filled cavity is measured it becomes clear that the modes interact to form two new much-displaced modes. The interaction can be viewed as an anti-crossing of the constituent exciton and cavity modes so as to form two new hybrid polaritons. These hybrid modes are also evident in

the experimental data in panel c). Section 3.1 details how and why such a feature is indicative of a coupling interaction between the modes that have anti-crossed.

In the work reported here I sought to replicate this anti-crossing for strong coupling using my metamaterial analogue. I also set out to probe the character of the polaritons by making use of another RF advantage, that of being able to map easily the electromagnetic near-fields.

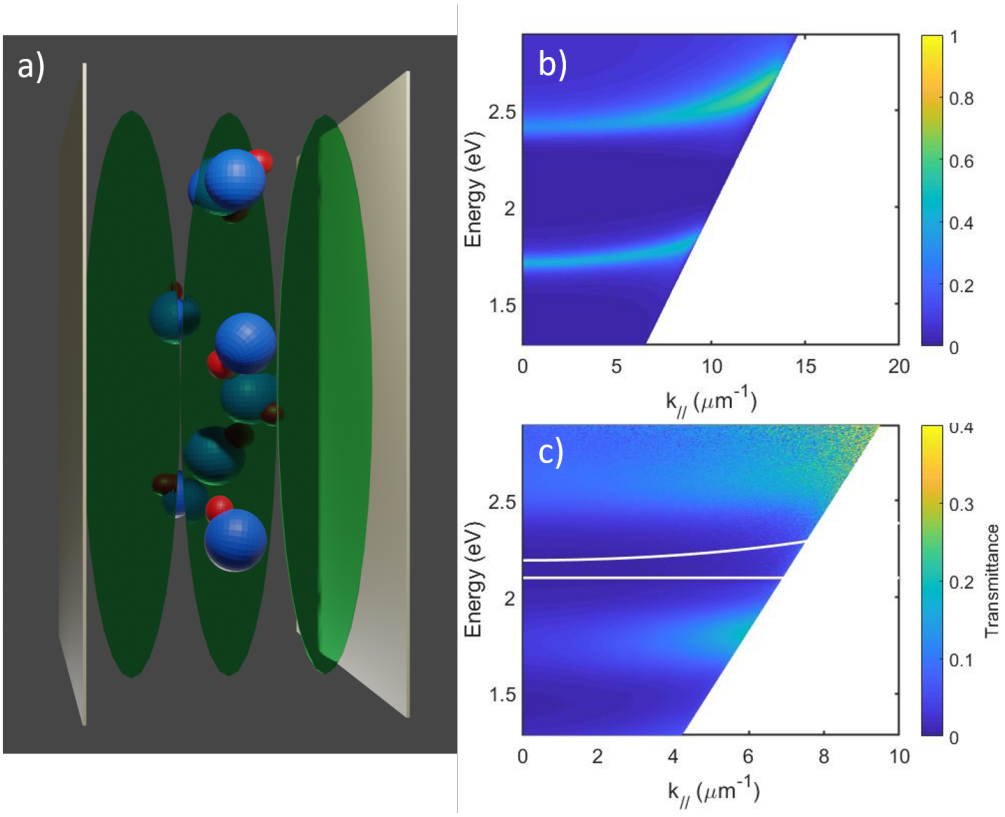

Figure 8.1: Experimental schematic, modelling, and results for a typical strong coupling experiment in an optical microcavity (data and modelling provided by Wai Jue Tan). a) A schematic of a cavity filled with molecules. (b,c) The simulated (b) and experimental (c) results of a strong coupling experiment in the optical regime where molecules of the dye TDBC are confined within an optical microcavity. In both (b) and (c) the transmission through the cavity is shown as a function of energy (eV) and in-plane wavevector ($k_{\|}$). The plots show how the modes, indicated by relatively high regions of transmission, change in energy with increasing wavevector. The transmission in the experiment is roughly a factor of 2 less than in the simulation. This is likely due to losses that are not included in the simulation, e.g. scattering. The curved (cavity) and flat (exciton) lines represent the uncoupled modes. The anti-crossing between the cavity mode and the exciton mode seen in both simulation and experiment is a key signature of strong coupling.

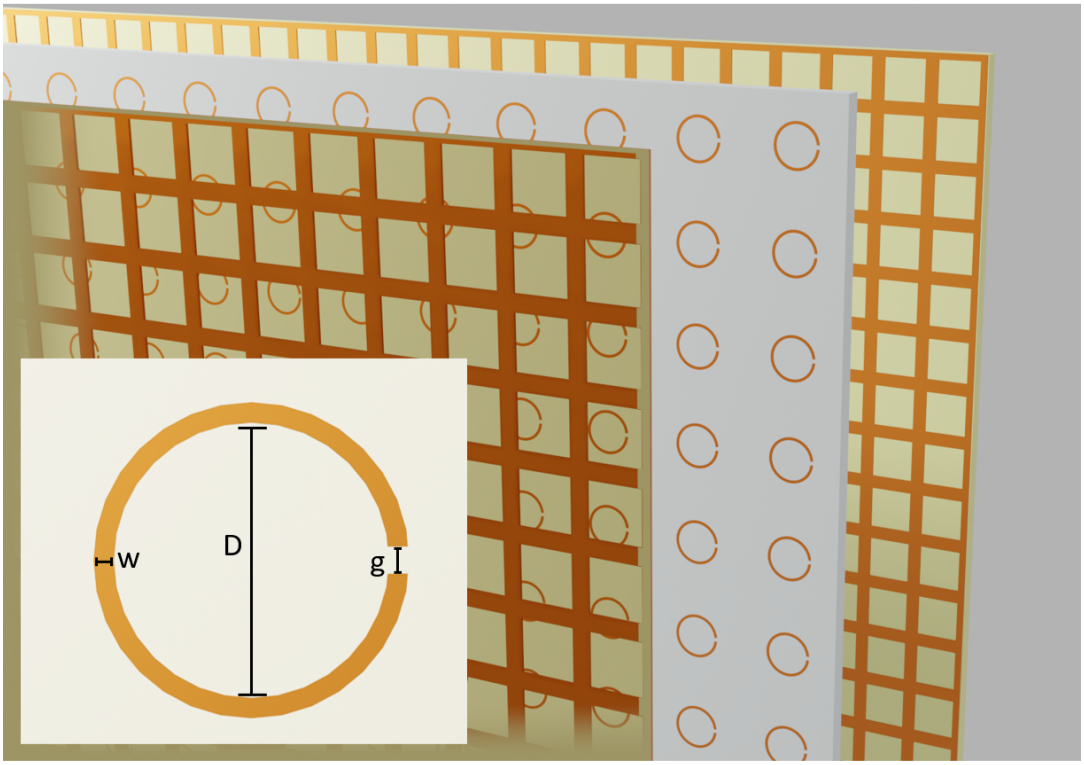

Figure 8.2: Metamaterial cavity and meta-molecules. The schematic shows a cavity made from two mesh/grid mirrors, between which is a sheet of meta-molecules. The mirrors are formed of a copper grid on a dielectric substrate with a grid period of 1.5 mm and an aperture size of 1.25 mm. The meta-molecules are copper split-ring resonators, also on a dielectric substrate. The inset shows the dimensions of a single split-ring resonator: w = 0.15 mm, D = 1.1 mm, g = 0.1 mm. The mirrors were 300 mm × 300 mm in area, the mirror separation was 29 mm. All metal areas were 35 μm in thickness.

8.3 Resonator Design

To investigate the use of metamaterials as analogues for molecular strong coupling two key components are required, a planar Fabry-Pérot cavity suitable for GHz frequencies, and a set of meta-molecules to place inside the cavity. Both were created using commercial wet-etching techniques by the company Multi Circuit Boards, see section 4.2, and all samples have a copper thickness of 35 μm. Let us look at each of these in turn.

8.3.1 Cavity

Here, a cavity refers to the space between two mirrors. The Fabry-Pérot modes of a cavity such as this arise because the mirrors act to confine the electric field inside the cavity, the field must form a standing wave - much as the vibrations on

a violin string are standing waves. At normal incidence the wavelengths that can pass through a Fabry-Pérot cavity are only those that can fit as a standing wave in the cavity, that is, $a = n\lambda/2$, where a is the distance between the two plates of the cavity and n is some integer value.

The cavities used in strong coupling experiments in the visible and infrared parts of the spectrum frequently make use of mirrors based on simple metal films [47, 143–146]. These metal films are typically 30 nm or so thick, a thickness comparable with the skin depth. At this thickness they are highly reflecting, but still provide some degree of field penetration, allowing the incident light to be coupled in to the modes of the cavity. Such an approach is not suitable at the GHz frequencies associated with the radio frequency RF range, owing to the very large impedance mismatch between metals and air at these frequencies.

For an operating frequency of $\sim$ 24 GHz – my chosen frequency regime – a continuous metal film would need to be of order only 1 nm thick to provide the same degree of transmission as is commonly achieved at optical frequencies. Instead the cavities used in this work were based on metallic mesh mirrors. Each of the mirrors was formed from a dielectric panel 300 mm x 300 mm in area (substrate material FR4, thickness 1.55 mm), upon which there was a square copper mesh (mesh period 1.5 mm, the mesh wires being 0.25 mm wide and 35 μm thick, see figure 8.2). The mesh character of these panels means that they provide $\sim$75% reflectance and $\sim$25% transmittance in my chosen frequency range.

I chose to work with a cavity having a spacing between the mirrors of 29 mm. This choice of cavity thickness means that it is the fifth-order mode that occurs in the chosen frequency range near 24 GHz. Whilst it might seem better to work with a cavity thickness that results in 24 GHz being the frequency of the lowest-order mode, such a cavity would be only $\sim$ 5 mm across, and this would not provide the space needed to include both meta-molecules and near-field probes. The first order mode ($n = 1$) would occur at a wavelength of 58 mm and would have a peak of electric field at the center of the cavity. Due to the semi-permeable nature of the cavity this is not entirely the case and the wavelength will be slightly longer as the

mode 'leaks' past the mesh, but the field peak remains central. This is true for all odd ordered modes, whilst all even ordered modes will have a field minimum at the center of the cavity. As I intended to include only a panel of resonators at the centre, rather than filling the entire cavity, only odd ordered modes are of interest to coupling.

I should note that when making my 'empty' cavity measurements the cavity was not in fact empty. When making empty cavity measurements I made use of a blank substrate to mimic everything about my filled cavity except for the array of SRR meta-molecules. To do this I included in the 'empty' cavity a 300 x 300 mm, 1.55 mm thick panel of Rogers 4350B substrate, positioned with one surface at the center of the cavity. The inclusion of this blank substrate lowers the frequency of the odd-order modes of the cavity when compared to the frequency expected for an empty cavity, this is because the odd-order modes have a field maximum at the cavity centre and thus experience a different effective cavity permittivity. The even-ordered modes are less effected by the blank substrate than the even-ordered modes since they have a field minimum at this position.

8.3.2 Split-ring Resonator Panel

The meta-molecule here needs to replicate a few features of an exciton for this study: it needs to interact with the cavity mode through a single dipole interaction and, in the absence of the cavity, it needs to have little to no interaction with its neighbouring meta-molecules[147].

I chose to base my meta-molecules on split-ring resonators [14] (SRRs), as shown in the inset of Figure 8.2. The SRRs had an outer radius of 0.7 mm, a ring width of 0.15 mm, a gap size of 0.1 mm. These parameters give the SRRs a first-order resonance frequency of 24.46 GHz when printed on a (dielectric) Rogers 4350B substrate. This lowest-order mode of the SRR has two dipole moments. A magnetic moment oriented out of the plane of the ring and an electric moment oriented in the plane. The electric moment is localised within the split of the SRR and directed across the split whilst the magnetic moment goes through the plane of the ring at

its center. By changing the polarisation of an externally applied exciting field one, both, or none of these moments can be coupled to so as to excite the SRR. In this study I chose an orientation for the incident electric field such that only the electric moment is excited. This choice still results in a magnetic moment being induced by currents circulating in the ring [148] but, because this moment is perpendicular to the magnetic fields in the cavity, it contributes only negligibly to the subsequent interaction. The SRRs were printed so that the spacing between the center of each resonator was 6 mm, enabling 2500 resonators to be produced on a single sheet.

At this spacing the interaction between the resonators is low, the primary affect being a modest increase in resonance linewidth rather than a shift in resonance frequency, this is comparable to observations made elsewhere [103]. If coupling were significant between the rings then modes would be able to propagate along the surface. This would be indicated by a significantly non-zero gradient in the mode's dispersion plot.

8.4 Methods

Two characterisation techniques were used in this work to probe the far- and near-field responses of my system. The details of each follow.

8.4.1 Far-field Measurements

The far field is considered to be the radiative component of a system's fields. Far-field, or radiative, measurements are how such strong coupling experiments are performed in the optical regime as the modes of a cavity, both loaded and unloaded with aggregate, are easy to see in transmission. Here, it excellently complements the novel near-field measurements. Measurements in the far field serve to present a structure's ensemble response, something that can be hard to ascertain from the near-field measurements.

In order to measure the radiative transmission through a microwave cavity loaded with resonators, two far-field horn antennas were used. A horn antenna is a type of electromagnetic source that uses the geometry of a horn to produce or detect free-

space RF radiation. The horn antenna is designed in such a way as to impedance match the 50 Ω connecting cables to free-space radiation over a specific frequency range, in this case 18 - 26.5 GHz. Additionally, the horns used had plastic microwave lenses to partially collimate the microwaves. Each had a 3dB beam-width of 5.7 deg in the E-plane and 6.6 deg in the H-plane.

The two horns were positioned facing each other across a optical table with the empty cavity, bare meta-molecules, or combined system placed between them. A VNA, connected to the horns via coaxial cables, was used to measure the transmission through the cavity as it was gradually rotated through 20 degrees on a motorized stage.

8.4.2 Near-field Measurements

The response in the near field was characterised by exciting the cavity at a fixed angle of 15.5 degrees using a horn antenna and measuring the transmission between the horn antenna and a wire antenna mounted within the cavity.

The wire antenna comprised a length of coaxial cable from which the metallic mesh shielding and outer dielectric (plastic) layer had been removed at one end so as to expose a short length of the central metallic wire that acts as an electric dipole, and is able to detect local incoming fields.

The wire antenna was positioned 2 ±1 mm from the substrate panel so as to detect the localised fields around the rings and the de-localised fields within the cavity whilst they are excited by the external far field. This antenna was then scanned in a raster pattern in the plane of the resonator sheet in both x- and y-directions to map out the response across the sheet.

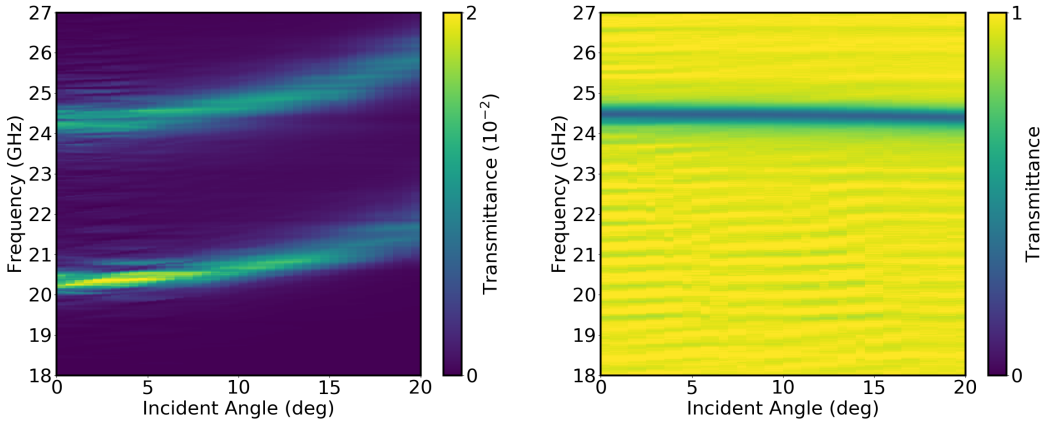

Figure 8.3: The transmittance as a function of frequency and incident angle through a) a 29 mm mesh cavity and b) and panel of SRRs.

8.5 Response of Meta-analogue System and Constituents

In this section I will describe the far- and near-field responses of the above described resonators, both individually and in combined form. The far-field results from the constituent components will be used to show that strong coupling has been achieved between the two resonators, then a near-field analysis will show the effects of this strong coupling on individual resonators in a manner not possible in the molecular regime.

8.5.1 Far Field

Angle dependent far-field transmission data were acquired for three different configurations: the empty (unloaded) cavity; the sheet of SRR meta-molecules on their own, i.e. outside the cavity; and the cavity loaded with the sheet of SRR meta-molecules. Transmission data were acquired for a range of incident angles between 0° and 20°. The data for the 'empty' cavity and bare rings is shown in figure 8.3.

The data for the 'empty' cavity shows two transmission peaks at 0°, $\sim$ 20.5 GHz and $\sim$ 24.5 GHz; these are the fourth- and fifth-order cavity modes respectively. They also disperse up in frequency as the incident angle is increased to 21.5 GHz

and 25.8 GHz at 20°, as expected for cavity modes. The bare rings show a single transmission dip at $\sim$ 24.42 GHz. There is also a very slight shift in the frequency of this mode as the incident angle increases, Figure 8.3b indicates a shift to 24.4 GHz at 20°. This is due to an anti-crossing between the SRR's first order mode and their highly negatively dispersive second order mode which intersects at high incident angle. While this is not ideal, the SRR panel is suitably non-interacting over the 20° range of interest for my purposes.

Figure 8.4 shows transmission for an empty and filled cavity at 6° where the fifth order cavity and SRR modes from figure 8.3 cross. For the filled cavity the fourth order mode still shows as a single peak, similar to that for the 'empty' (uncoupled) cavity. However, the fifth-order mode shows a very clear splitting. The cause of this splitting can be understood by looking at the data in panel a) of Figure 8.5, where the transmittance is shown as a function of incident angle for the filled (loaded) cavity.

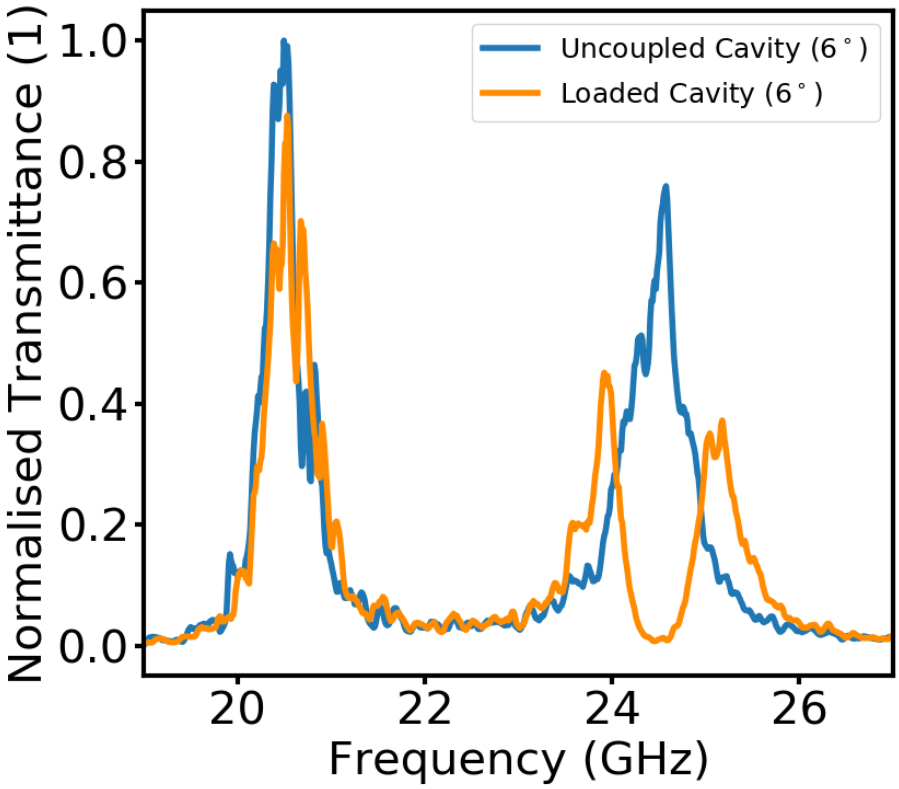

Figure 8.4: Transmission spectra for both the 'empty' and 'filled' cavities at 6° where the uncoupled modes of the exciton and empty cavity intersect. Coupling between the two is clear from the prominent splitting centered at 24.6 GHz.

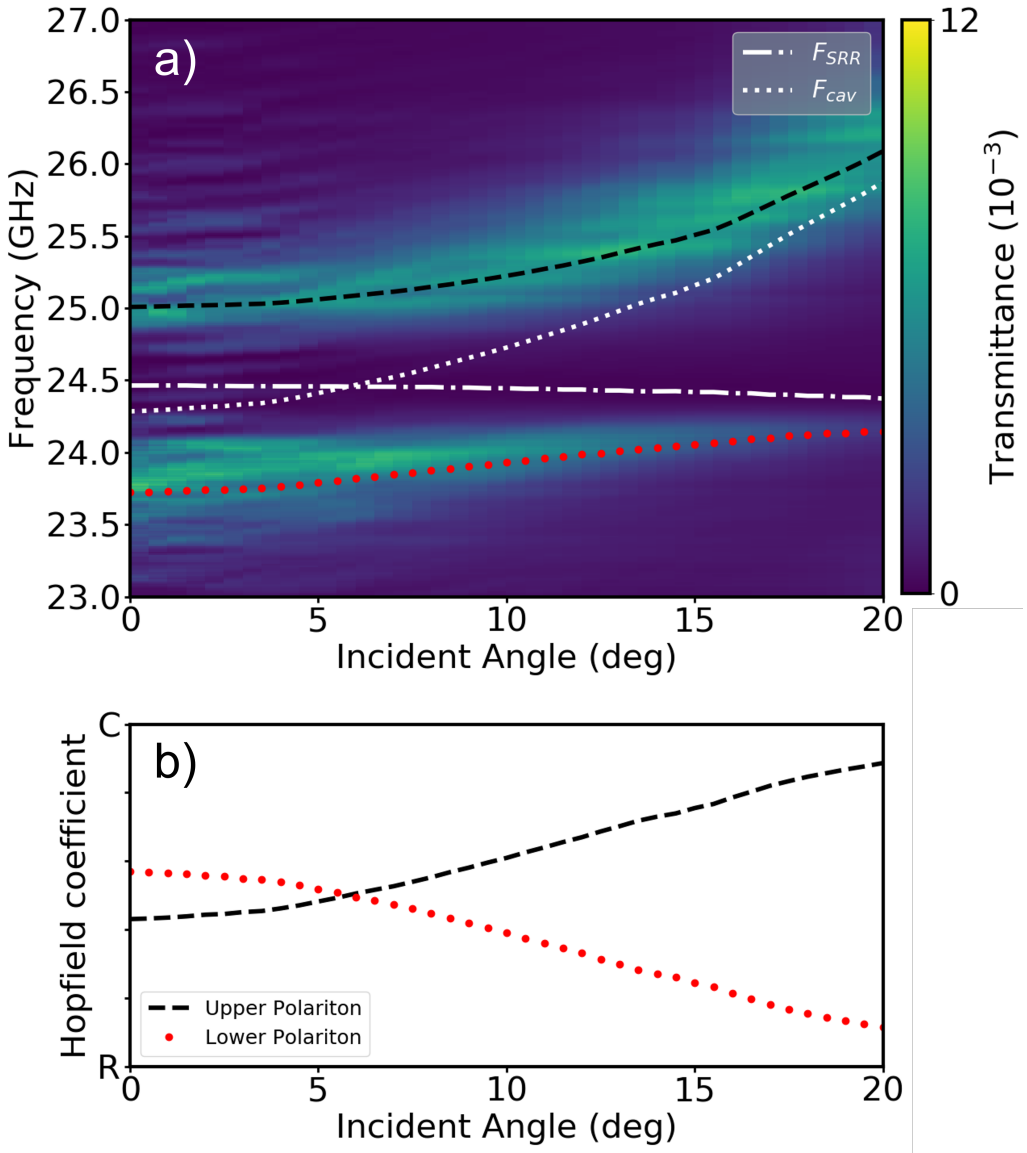

Figure 8.5: a) Transmission through a 29 mm cavity filled with SRR's as the incident angle is swept between 0 and 20 degrees. Plotted in white are the uncoupled mode positions of the resonators (F_{SRR}) and the cavity (F_{cav}). Plotted in black and red are the calculated Upper and Lower polariton modes respectively. b) Plot of the Hopfield coefficients for the upper and lower polariton modes as the incident angle is swept between 0 and 20 degrees. The coefficients are plotted between R, which represents a fully SRR-like mode, and C, which represents a fully cavity-like mode.

In Figure 8.5a the measured position of the SRR meta-molecule resonance is indicated by the white dash-dot line, whilst the measured position of the 'empty' cavity is indicated by the white dotted line. Both of these lines were extracted from the data sets in Figure 8.4 by fitting a lorentzian curve to their transmission features and recording the fitted peak value. The frequency of the 'empty' cavity mode matches that of the meta-molecule resonance for an angle of incidence of 6°, and it can be seen from the transmittance data for the loaded cavity (colour map) that there is an anti-crossing. This anti-crossing is the key feature of strong coupling, it is one of the major results from this investigation. See section 3.1 for an explanation of why an anti-crossing is indicative of coupling.

To check that we are in the strong coupling regime we need to determine the extent of the anti-crossing, i.e. the frequency separation, Ω, and compare it with the width of the bare cavity mode, $\Delta\omega_{cav}$, and the width of the bare resonator modes, $\Delta\omega_{SRR}$. More specifically we need to check whether, $\Omega > \Delta\omega_{cav} + \Delta\omega_{SRR}$ [149, 150], this is perhaps the most stringent criterion of strong coupling. We determined the widths as follows: $\Delta\omega_{cav} = 0.57 \pm 0.02$ GHz, and $\Delta\omega_{SRR} = 0.38 \pm 0.04$ GHz, so that $\Delta\omega_{cav} + \Delta\omega_{SRR} = 0.95 \pm 0.05$ GHz. The splitting is determined by the frequency separation of the new hybrid modes at what, in the absence of coupling, would be the crossing point, i.e. at an angle of incidence of 6°. From the data in figure 8.4 we find the splitting to be $\Omega = 1.25 \pm 0.05$ GHz, significantly greater than the sum of the line-widths; we are thus in the strong coupling regime.

Strong coupling involves the formation of hybrid polariton modes, and one indication of this comes from looking at the dispersion of the modes and the observation of an anti-crossing, as we have seen in Figure 8.5. In addition it is both interesting and informative to look at the hybrid nature of the strongly coupled modes, specifically to explore the light/matter content that they possess. In the optical regime this has not so far been directly possible. As I will show below, the metamaterial analogue approach does allow such an opportunity. I will discuss probing this aspect by experiment below but before doing so I wish to focus on calculating the light/matter content of these hybrid modes.

A convenient technique for predicting the degree of hybridisation we expect in a system such as that explored here is to make use of a simple coupled oscillator model [36, 151]. The near flat-band nature of the resonator (SRR) only response indicates that the interaction between the SRR resonators is very weak and can be treated as a single oscillator, the coupled oscillator model for the system can thus be represented as (8.1),

$$\begin{bmatrix} F_{cav} & \Omega \\ \Omega & F_{SRR} \end{bmatrix} \cdot \begin{bmatrix} x_1 \\ x_2 \end{bmatrix} = \lambda \begin{bmatrix} x_1 \\ x_2 \end{bmatrix}, \tag{8.1}$$

where F_{cav} is the resonance frequency of the empty cavity, F_{SRR} is the resonance frequency of the bare SRRs and Ω is the coupling strength between the two. x_1 and x_2 make up an eigenvector of the system whilst λ is a corresponding eigenvalue. The eigenvalues of this matrix are the frequency positions of the upper and lower polaritons of the coupled system, while the components of the eigenvectors (x_1 and x_2) are the Hopfield coefficients, in this case these give the degree of 'cavity-like' and 'meta-molecule-like' character of the polaritons. By choosing a value of Γ that fits the polariton modes to those measured in experiment we can derive the degree of mode hybridisation between the resonators and the cavity from the eigenvectors. These fitted eigenvalues can be seen as red dotted and black dashed lines in Figure 8.5a. Figure 8.5b shows the results of the Hopfield analysis on my system. The upper polariton (UP) changes from being more SRR-like at normal incidence to almost entirely cavity-like at 20°, and vice-versa for the lower polariton (LP). The Hopfield coefficients crossing at 6° also coincides with the uncoupled mode crossing. As will be seen below, I chose to make my near-field measurements at an angle of incidence of 15.5°, where the upper polariton is 74.6% cavity-like and the lower polariton is 25.4% cavity like.

8.5.2 Near Field

Let us turn now to the experimental data relevant to probing the character of the measured polariton modes. Looking first at the empty cavity, figure panel 8.6a shows two spectra, one for each of the component systems: the empty cavity (orange) and the array of meta-molecules on their own (red). Panels b) and c) show near-field scans of the bare SRRs at their resonance frequency and the empty cavity at its fifth-order mode respectively. The near-field scans are plotted as colour scales, the colour indicating the strength of the detected field as a function of spatial location across the resonator array. These two scans show the features I expect to mix in the hybridised system. In panel b) excitation around the bare SRRs is highly localised to the neighbourhood of the resonators. The streaks in these data in the y-direction are due to the smearing effect resulting from the finite size of the near-field antenna. In the x-direction it is clear that there is little to no interaction between neighbouring resonators, as would be expected in a low dispersion structure such as this.

In the empty cavity data, panel c), we see clear bands, or oscillations, arising from the in-plane propagating nature of the cavity mode. These are related to the incident angle of the exciting fields by $k_x = k\sin(\theta)$. Where k_x is the wavenumber in the x direction, k is the total wavenumber of the incident radiation, and θ is the incident angle. From this equation it can be deduced that at normal incidence the spacing would be infinite (no oscillations visible) and that at 90 degrees, when the wave is propagating along rather than through the cavity, the spacing will unsurprisingly match the wavelength. The bands observed here, with a spacing of 44.2 mm, are consistent with the fields inside the cavity being excited at an angle of incidence of 15.5°. The band positions are arbitrary as they are determined by the phase at which the snap shot was chosen. An animation over the full phase would show the bands processing across the plot in the x direction.

Looking now at Figure 8.7a, we again see a line spectrum. This time the spectrum is that obtained by a far-field transmission measurement, again at an angle of incidence of 15.5°, of the loaded cavity. Four frequencies of interest are indicated as b), c), d) and e) - referring to the near-field maps shown in panels b), c), d) and e);

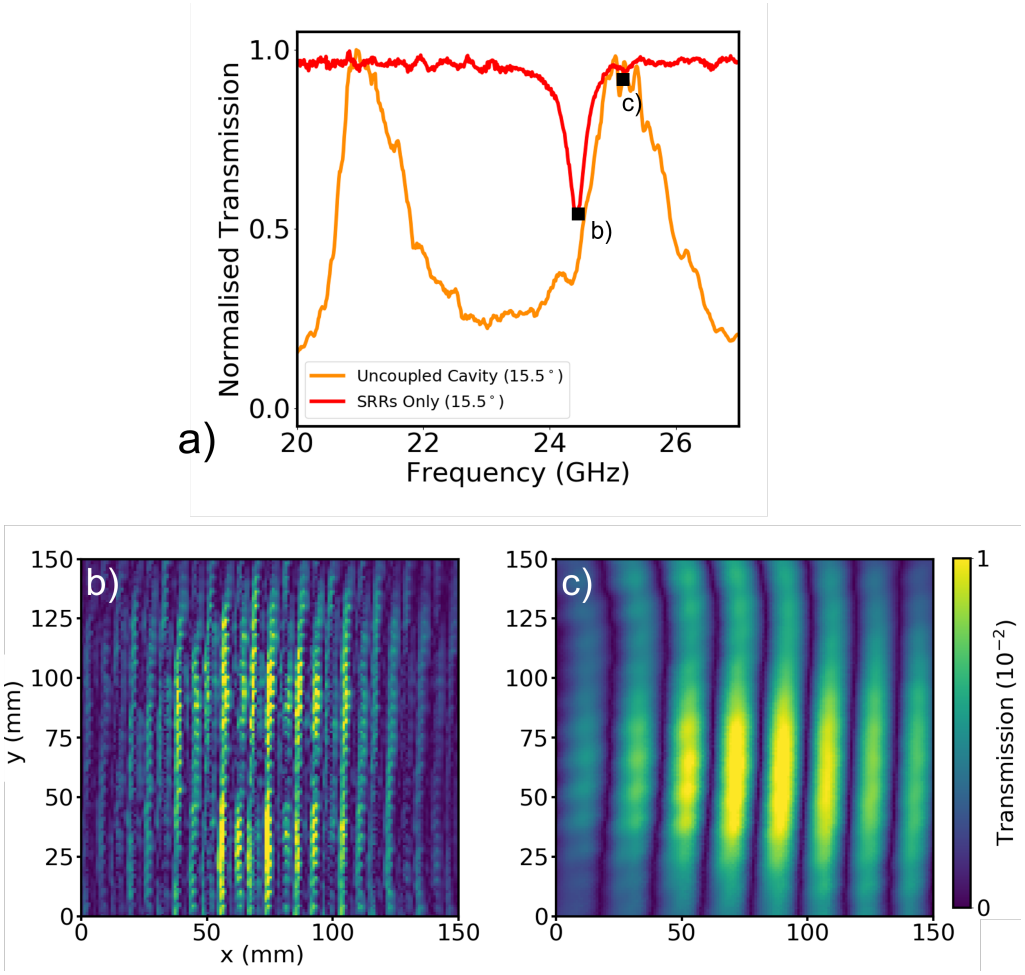

Figure 8.6: All the features in this figure were taken with an incident angle of 15.5 degrees. (a) far-field transmission spectra at a 15.5° angle of incidence for cavity-only and SRR-only systems, the frequencies at which the cavity-only (25.42 GHz) and SRR-only (24.45 GHz) near-field plots were obtained are indicated; (b) map of the near field across the sheet of resonators; (c) map of the near field inside the empty cavity.

let us look at each of these in turn. The fourth-order mode (b) of the loaded (filled) cavity is very similar to the data for the empty cavity, panel c) although with the change in frequency comes a change in the period of the oscillations to 53.4 mm. Despite being filled with the SRR array there are no signs of hybridisation, only small perturbations in the field when the detecting antenna is in close proximity to the metal resonators. Panel d) shows a near-field map for a frequency that matches the resonance of the bare SRRs. Despite the near-zero transmission at this point (see panel a)) we can see that the SRRs are nonetheless excited, and that there is very little indication of any hybridisation to a cavity mode. Panels c) and e) show near-field scans at the frequency of the lower and upper polaritons modes for this

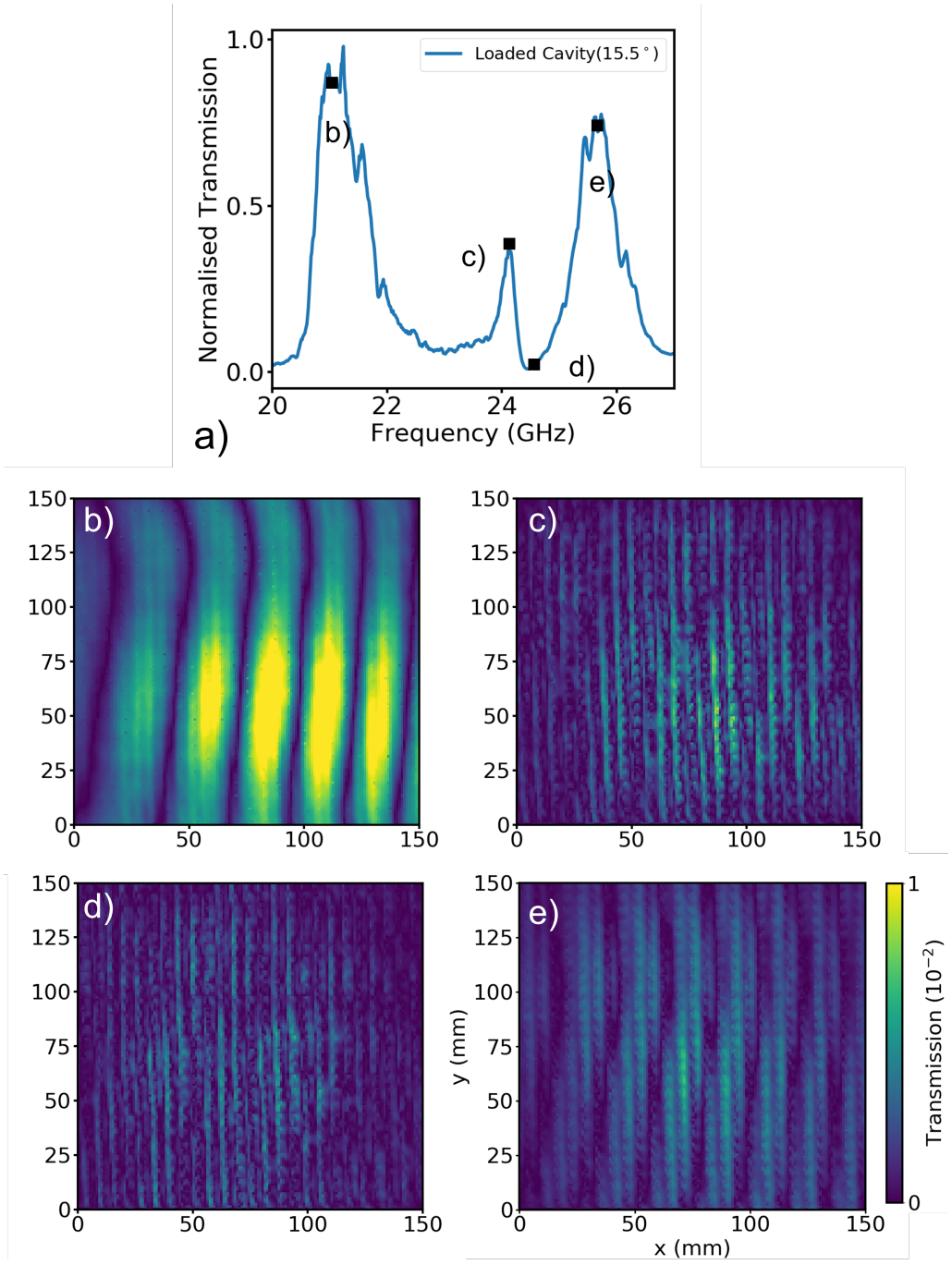

Figure 8.7: All the features in this figure were taken with an incident angle of 15.5 degrees. he spectrum for the filled cavity, again at a 15.5° angle of incidence. The frequencies at which the near-field maps in the remaining panels were acquired are indicated, (b) near-field map at the fourth order mode (21.0 GHz); (c) near-field map for the lower polariton (24.12 GHz); d) near-field map at the frequency of the bare SRR resonance (24.41 GHz); (e) near-field map for the upper polariton (25.5 GHz). As predicted by the Hopfield analysis at 15.5° (see Figure 8.5b), the two polaritons share both cavity and SRR-like features though to very different degrees, with the lower polariton being SRR-like and sharing many features with the measurement of the bare SRRs whilst the lower polariton has SRR-like features but predominately resembles the empty cavity in near-field profile.

angle of incidence. From the Hopfield analysis described above we can expect a high degree of SRR-like features in (c), whilst we should expect cavity-like features in (e). This is indeed the case with the LP mode being primarily similar in form to the bare SRRs, but with a slight modulation in the x-direction from the cavity mode, whilst the UP mode appears to look like a cavity mode perturbed by the presence of the SRRs.

8.6 Conclusions

I have shown that metamaterials can be used to construct an analogue of a very topical and important class of structures in which strong coupling between molecules and confined light fields is explored and exploited. I have made use of circuit board techniques to make a radio-frequency cavity filled with meta-molecules. My cavity employed mirrors made of a metallic mesh to form a planar Fabry-Pérot cavity whilst my meta-molecules were based on split-ring resonators. Specifically I have shown that anti-crossing between a cavity mode and the meta-molecule resonance can be achieved, and that the extent of the mode splitting between the hybrid polariton modes so formed satisfies the most stringent of strong coupling criteria. I have then exploited a key feature of working at GHz frequencies by directly probing the RF near field to look at the mixed light/matter content of the polariton modes, finding good agreement with what is expected on the basis of a well-established coupled oscillator model.

Chapter 9

Conclusion and Future Work

9.1 Conclusions

In the initial data chapter 5, I presented an analysis of two coupled SRR's as one is actively tuned through the other. This analysis revealed a tuning dependence in the electric and magnetic coupling terms, a feature not previously presented in the literature, along with a surprisingly high degree of electric coupling in the case of orthogonal orientation. I ascribed this seemingly anomalous coupling to the rotational symmetry of the ring inducing an offset alongside the rotation. This chapter highlighted some of the difficulties in the meta-analogue approach, the need to tailor meta-atoms carefully and consider the full extent of their interactions, and it informed the design of meta-atoms used in future chapters.

In the following chapter I used non-bianisotropic meta-atom designs to eliminate some of the difficulties from the previous chapter. In this chapter I presented two meta-atom designs that exhibited a dipole moment either out of the plane or along the plane and stacked them axially. I then probed them in the near field and utilised Fourier analysis to reveal that they coupled together in manners analogous to J- and H- type aggregates respectively. This served as a proof of concept for the proposed meta-analogy, but also allowed me to create a novel metamaterial design. By exploiting the non-bianisotropic nature of the meta-atoms I combined them into a single design that could simultaneously support J- and H- like interactions without coupling them, allowing for a mode crossing. Finally, I broke the symmetry of this

hybrid design to couple the two modes and create an anti-crossing of modes in the middle of the structure's Brillouin zone, a previously undocumented behaviour in meta-material chains.

In chapter 7 I reapplied the J- and H- like aggregate chains from the previous chapter as analogues for single molecules in the SSH model. This model was first used to predict Soliton states due to defects in a molecular aggregate, and so in this chapter I replicated that prediction on the microwave scale. I directly observed the formation of Soliton states that agreed in symmetry and character to those predicted by the SSH model. The accuracy of this agreement was shown to be robust across multiple conditions allowed by the model: termination defects, tight and loose bulk boundaries and the system being periodic in either coupling strength or resonator frequency. These results show both the power and flexibility of the meta-analogue approach as a tool for directly observing modes that, in a molecular aggregate, would otherwise manifest at an atom to atom scale.

In the final data chapter I recreated a classical strong coupling experiment in the microwave regime with a panel of microwave resonators and a wire mesh cavity. The two elements coupled together in a manner matching the criteria of the strong coupling regime, exhibiting a clear upper and lower polariton state. I then probed within the cavity during excitation in the near field and mapped the meta-polariton states, directly showing how cavity and exciton-like resonances hybridized into the meta-polariton quasi-particle. A visualisation of the hybridisation of mode character is an insight into the strong coupling interaction not previously afforded before the application of the meta-analogue approach.

This thesis has presented the development and initial application of a novel meta-analogue approach to researching molecular aggregate phenomena. The meta-analogue approach is to replicate aggregate phenomena using microwave metamaterials whose larger scale allows for far more invasive interrogation than their aggregate counterparts. In this way the approach offers new insights into molecular aggregate properties whilst also promoting the creation of a new class of aggregate inspired metamaterials.

9.2 Future Work

1. **Using active components to tune dispersion:** The results of chapter 5, namely that the coupling can be tuned as well as resonance frequency, can be exploited to create chains with a tunable dispersion. This application could not only flatten a dispersion curve, but also switch whether its dispersion was positive or negative, changing the direction of a propagating mode's group velocity, by tuning into a region where coupling between elements switches from being net-positive to net negative. This does present the engineering challenge of stacking and simultaneously tuning a long chain of resonators, but the results presented here reveal it as a possibility

2. **2D and 3D meta-analogue structures:** There is a metamaterials challenge to develop meta-molecules that go deeper into the sub-wavelength regime [152]. In chapter 6 I achieved sufficient sub-wavelength aggregation by working in 1D, stacking my meta-molecules in an axial direction. It would be convenient to extend the work to higher dimensions, but even in 2D, sub-wavelength inter-molecular separations are hard to achieve [124]. Ring systems, lying between 1 and 2D might make an interesting next step and are widely found in molecular systems, both natural and synthetic [153, 154]. There is a need to develop meta-molecules whose size in all three dimensions are significantly less than their associated resonance wavelength.

3. **Random disorder along a chain:** In chapter 7 I explored static disorder along the chain, but a more granular approach to the meta-atom construction could allow for investigations of random disorder and the possibility of directly probing Anderson localisation [155]. This could either be achieved by incorporating a random element into the meta-atom design or by actively tuning each element by a random amount. Both methods have their respective difficulties in experimental execution but are certainly conceivable in finite element modelling if computationally taxing.

4. **Further exploring dark modes in strong coupling:** The resonator panel used in chapter 8 incorporated no disorder in its design. The dark states in molecular aggregate research are strongly linked to disorder and adding disorder to the orientation, size and positioning of the resonators on the panel could explore them more fully.

5. **Two level meta-atoms:** One of the primary flaws of the meta-analogue approach is that it seeks to to replicate atoms with a non-zero ground state energy with passive meta-atoms that do have a zero ground state. It is possible, however, to imagine a resonator with an incorporated circuit and power source that could be switched to a different mode through the application of resonant radiation. Designing such a circuit, and compressing it down enough to significantly effect how the resonator couples to radiation, are the two primary challenges presented by this task. However, if achieved it would greatly increase the strength of the meta-analogue approach.

6. **Resonator concentration dependence of strong coupling:** The concentration of aggregate molecules within the cavity of a strong coupling experiment is known to influence the strength of the coupling [156]. The relationship between that concentration and the coupling strength could be determined exactly in a meta-analogue study. A precisely spaced and known number of resonators is simple achieve at the cm scale and could offer strong confirmation to the theories already presented.

Chapter 10

Publications

Published

- M. Baraclough, I. R. Hooper and W. L. Barnes. Investigation of the coupling between tunable split-ring resonators. *Phys. Rev. B*, 98:085146, Aug 2018.
- M. Baraclough, S. S. Seetharaman, I. R. Hooper and W. L. Barnes. Metamaterial Analogues of Molecular Aggregates. *ACS Photonics*, 6(11):3003–3009, Nov 2019.
- M. Baraclough, I. R. Hooper and W. L. Barnes. Direct observation of defect modes in molecular aggregate analogs. *Phys. Rev. B*, 102:224105, Dec 2020.

Under Review

- M. Baraclough, I. R. Hooper and W. L. Barnes. Metamaterial analogues of strongly coupled molecular ensembles. *ACS Photonics*

Poster Presentation

- M. Baraclough, I. R. Hooper and W. L. Barnes. Anti-crossing of counter propagating modes within the Brillouin Zone. *META2019* Jul 2019

Bibliography

[1] Trevon Badloe, Inki Kim, and Junsuk Rho. Moth-eye shaped on-demand broadband and switchable perfect absorbers based on vanadium dioxide. *Scientific Reports*, 10(1):4522, 2020.

[2] N. S. Kardashev. Transmission of Information by Extraterrestrial Civilizations. *Soviet Astronomy*, 8:217, October 1964.

[3] R. Bansal. Roman invisibility cloak? [microwave surfing]. *IEEE Microwave Magazine*, 21(1):14–118, 2020.

[4] Enoch Stefan Brûlé, Stéphane and Sébastien Guenneau. Role of nanophotonics in the birth of seismic megastructures. *Nanophotonics*, 8(10):1591–1605, 2019.

[5] H. Lamb. *On Group-velocity.* C.F. Hodgson & Son, 1st edition, 1904.

[6] V. G. Veselago. The electrodynamics of substances with simultaneously negative values of ϵ and μ. *Phys. Usp.*, 10(4):509–514, 1968.

[7] Earl R. Callen and Herbert B. Callen. Static magnetoelastic coupling in cubic crystals. *Phys. Rev.*, 129:578–593, Jan 1963.

[8] H. N. Spector and T. N. Casselman. Interaction of alfvén waves and spin waves in a ferromagnetic metal. *Phys. Rev.*, 139:A1594–A1597, Aug 1965.

[9] Eli Yablonovitch. Inhibited spontaneous emission in solid-state physics and electronics. *Phys. Rev. Lett.*, 58:2059–2062, May 1987.

[10] Victor Veselago, L. Braginsky, Valery Shklover, and Christian Hafner. Negative refractive index materials. *Journal of Computational and Theoretical Nanoscience*, 3:189–218, 04 2006.

[11] D. R. Smith, Willie J. Padilla, D. C. Vier, S. C. Nemat-Nasser, and S. Schultz. Composite medium with simultaneously negative permeability and permittivity. *Phys. Rev. Lett.*, 84:4184–4187, May 2000.

[12] J. B Pendry. Photonic band structures. *Journal of Modern Optics*, 41:209–229, 1994.

[13] J. B. Pendry, A. J. Holden, W. J. Stewart, and I. Youngs. Extremely low frequency plasmons in metallic mesostructures. *Phys. Rev. Lett.*, 76:4773–4776, Jun 1996.

[14] J. B. Pendry, A. J. Holden, D. J. Robbins, and W. J. Stewart. Magnetism from conductors and enhanced nonlinear phenomena. *IEEE Transactions on Microwave Theory and Techniques*, 47:2075–2084, 1999.

[15] Eli Yablonovitch. Photonic Bandgap Structures as Meta-Materials. In *APS March Meeting Abstracts*, APS Meeting Abstracts, page Z5.002, March 2000.

[16] E. Shamonina, V. A. Kalinin, K. H. Ringhofer, and L. Solymar. Magneto-inductive waveguide. *Electronics Letters*, 38:371–373, 2002.

[17] E. Shamonina, V. A. Kalinin, K. H. Ringhofer, and L. Solymar. Magnetoinductive waves in one, two, three dimensions. *Journal of Applied Physics*, 92:6252–6261, 2002.

[18] M.C.K. Wiltshire. Dispersion characteristics of magneto-inductive waves: comparison between theory and experiment. *Electronics Letters*, 39:215–217(2), January 2003.

[19] M. Beruete, F. Falcone, M. J. Freire, R. Marqués, and J. D. Baena. Electroinductive waves in chains of complementary metamaterial elements. *Applied Physics Letters*, 88(8):083503, 2006.

[20] W. J. Padilla, D. N. Basov, and D. R. Smith. Negative refractive index metamaterials. *Materials Today*, 9:28–35, 2006.

[21] J.-H. Lee, J. P. Singer, and E. L. Thomas. Micro-/nanostructured mechanical metamaterials. *Advanced Materials*, 24:4782–4810, 2012.

[22] K. Yao and Y. Liu. Plasmonic metamaterials. *Nanotechnology Reviews*, 3:177–210, 2014.

[23] S. Haxha, F. AbdelMalek, F. Ouerghi, M. D. B. Charlton, A. Aggoun, and X. Fang. Metamaterial Superlenses Operating at Visible Wavelength for Imaging Applications. *Scientific Reports*, 8(1):16119, 2018.

[24] Zhi Ning Chen, Qing Xianming, Jin Shi, Chean Goh, Mei Sun, Anna Lau, and Wei Liu. Metamaterials-based antennas: from concepts to technology. 05 2014.

[25] Stéphane Brûlé, Stefan Enoch, and Sébastien Guenneau. Emergence of seismic metamaterials: Current state and future perspectives. *Physics Letters A*, 384(1):126034, 2020.

[26] Edwin E Jelley. Spectral Absorption and Fluorescence of Dyes in the Molecular State. *Nature*, 138(3502):1009–1010, 1936.

[27] Frank Würthner, Theo E. Kaiser, and Chantu R. Saha-Möller. J-aggregates: From serendipitous discovery to supramolecular engineering of functional dye materials. *Angewandte Chemie International Edition*, 50(15):3376–3410, 2011.

[28] G. Scheibe. About the variability of the absorption spectra in solutions and the minor valences as their cause. *Angew. Chem.*, 50(11):212–219, 1937.

[29] G. Scheibe. Reversible polymerisation als ursache neuartiger absorptionsbanden von farbstoffen. *Kolloid-Zeitschrift*, 82:1–14, 1938.

[30] Tadaaki Tani. *Photographic sensitivity: theory and mechanisms*, volume 8. Oxford University Press on Demand, 1995.

[31] Nicholas J. Hestand and Frank C. Spano. Expanded Theory of H- and J-Molecular Aggregates: The Effects of Vibronic Coupling and Intermolecular Charge Transfer. *Chemical Reviews*, 118(15):7069–7163, 2018.

[32] E. M. Purcell, H. C. Torrey, and R. V. Pound. Resonance absorption by nuclear magnetic moments in a solid. *Phys. Rev.*, 69:37–38, Jan 1946.

[33] C. Weisbuch, M. Nishioka, A. Ishikawa, and Y. Arakawa. Observation of the coupled exciton-photon mode splitting in a semiconductor quantum microcavity. *Phys. Rev. Lett.*, 69:3314–3317, Dec 1992.

[34] R. J. Thompson, G. Rempe, and H. J. Kimble. Observation of normal-mode splitting for an atom in an optical cavity. *Phys. Rev. Lett.*, 68:1132–1135, Feb 1992.

[35] R. Houdré, R. Stanley, U. Oesterle, M. Ilegems, and C. Weisbuch. Room temperature exciton-photon rabi splitting in a semiconductor microcavity. *Journal de Physique IV*, 3(C5):51–58, 1993.

[36] M. S. Skolnick, T. A. Fisher, and D. M. Whittaker. Strong coupling phenomena in quantum microcavity structures. *Semiconductor Science and Technology*, 13:645–669, 1998.

[37] Daniel Polak, Rahul Jayaprakash, Thomas P Lyons, Luis Á Martínez-Martínez, Anastasia Leventis, Kealan J Fallon, Harriet Coulthard, David G Bossanyi, Kyriacos Georgiou, Anthony J Petty Ii, John Anthony, Hugo Bronstein, Joel Yuen-Zhou, Alexander I Tartakovskii, Jenny Clark, and Andrew J Musser. Manipulating molecules with strong coupling: harvesting triplet excitons in organic exciton microcavities. *Chem Sci*, 11(2):343–354, Jan 2020.

[38] D G Lidzey, D D C Bradley, M S Skolnick, T Virgili, S Walker, and D M Whittaker. Strong exciton–photon coupling in an organic semiconductor microcavity. *Nature*, 395(6697):53–55, 1998.

[39] Thomas W. Ebbesen. Hybrid light–matter states in a molecular and material science perspective. *Accounts of Chemical Research*, 49(11):2403–2412, Oct 2016.

[40] Johannes Feist, Javier Galego, and Francisco J. Garcia-Vidal. Polaritonic chemistry with organic molecules. *ACS Photonics*, 5(1):205–216, Oct 2017.

[41] Kochise Bennett, Markus Kowalewski, and Shaul Mukamel. Novel photochemistry of molecular polaritons in optical cavities. *Faraday Discussions*, 194:259–282, 2016.

[42] Hoi Ling Luk, Johannes Feist, J. Jussi Toppari, and Gerrit Groenhof. Multiscale molecular dynamics simulations of polaritonic chemistry. *Journal of Chemical Theory and Computation*, 13(9):4324–4335, Aug 2017.

[43] Raphael F. Ribeiro, Luis A. Martínez-Martínez, Matthew Du, Jorge Campos-Gonzalez-Angulo, and Joel Yuen-Zhou. Polariton chemistry: controlling molecular dynamics with optical cavities. *Chemical Science*, 9(30):6325–6339, 2018.

[44] Joel Yuen-Zhou and Vinod M. Menon. Polariton chemistry: Thinking inside the (photon) box. *Proceedings of the National Academy of Sciences*, 116(12):5214–5216, Mar 2019.

[45] D. G. Lidzey, D. D. C. Bradley, T. Virgil, A. Armitage, M. S. Skolnick, and S. Walker. Room temperature polariton emission from strongly coupled organic semiconductor microcavities. *Physical Review Letters*, 82:3316–3319, 1999.

[46] A. Shalabney, J. George, J. Hutchison, G. Pupillo, C. Genet, and T. W. Ebbesen. Coherent coupling of molecular resonators with a microcavity mode. *Nature Communications*, 6(1):1–6, Jan 2015.

[47] B. S. Simpkins, Kenan P. Fears, Walter J. Dressick, Bryan T. Spann, Adam D. Dunkelberger, and Jeffrey C. Owrutsky. Spanning strong to weak normal mode coupling between vibrational and fabry–pérot cavity modes through tuning of vibrational absorption strength. *ACS Photonics*, 2(10):1460–1467, Oct 2015.

[48] S. Dai, Z. Fei, Q. Ma, A. S. Rodin, M. Wagner, A. S. McLeod, M. K. Liu, W. Gannett, W. Regan, K. Watanabe, T. Taniguchi, M. Thiemens, G. Dominguez, A. H. Castro Neto, A. Zettl, F. Keilmann, P. Jarillo-Herrero,

M. M. Folger, and D. N. Basov. Tunable phonon polaritons in atomically thin van der waals crystals of boron nitride. *Science*, 343:1125–1129, 2014.

[49] P. Pons-Valencia, F. J. Alfaro-Mozaz, M. M. Wiecha, V. Biolek, I. Dolado, S. Vélez, P. Li, P. Alonso-González, F. Casanova, L. E. Hueso, L. Martín-Moreno, R. Hillenbrand, and A. Y. Nikitin. Launching of hyperbolic phonon-polaritons in h-bn slabs by resonant metal plasmonic antennas. *Nature Communications*, 10(1):3242, 2019.

[50] M. Ramezani, A. Halpin, A. Fernández-Domínguez, J. Feist, S. Rodriguez, F. Garcia-Vidal, and J. Gómez Rivas. Plasmon-exciton-polariton lasing. *Optica*, 4:31–37, 2017.

[51] J. Kasprzak, M. Richard, S. Kundermann, A. Baas, P. Jeamburn, J. M. J. Keeling, F. M. Marchetti, M. H. Szymanska, R. Andre, J. L. Staehli, V. Savona, P. B. Littlewood, B. Deveaud, and Le Si Dang. Bose-einstein condensation of exciton polaritons. *Nature*, 443:409–414, 2006.

[52] Mikhail Vasilevskiy, Darío Santiago-Pérez, C. Trallero-Giner, Nuno Peres, and Alexey Kavokin. Exciton-polaritons in 2d dichalcogenide layers placed in a planar microcavity: tuneable interaction between two bose-einstein condensates. *Physical Review B*, 92, 09 2015.

[53] Rui Su, Sanjib Ghosh, Jun Wang, Sheng Liu, Carole Diederichs, Timothy C H Liew, and Qihua Xiong. Observation of exciton polariton condensation in a perovskite lattice at room temperature. *Nature Physics*, 16(3):301–306, 2020.

[54] Anoop Thomas, Jino George, Atef Shalabney, Marian Dryzhakov, Sreejith J. Varma, Joseph Moran, Thibault Chervy, Xiaolan Zhong, Eloïse Devaux, Cyriaque Genet, T. A. Hutchison, and T. W. Ebbesen. Ground-state chemical reactivity under vibrational coupling to the vacuum electromagnetic field. *Angewandte Chemie*, 128(38):11634–11638, Aug 2016.

[55] A. Thomas, L. Lethuillier-Karl, K. Nagarajan, R. M. A. Vergauwe, J. George, T. Chervy, A. Shalabney, E. Devaux, C. Genet, J. Moran, and T. W. Ebbesen.

Tilting a ground-state reactivity landscape by vibrational strong coupling. *Science*, 363(6427):615–619, 2019.

[56] Jyoti Lather, Pooja Bhatt, Anoop Thomas, Thomas W. Ebbesen, and Jino George. Cavity catalysis by cooperative vibrational strong coupling of reactant and solvent molecules. *Angewandte Chemie International Edition*, 58(31):10635–10638, 2019.

[57] Xiaolan Zhong, Thibault Chervy, Shaojun Wang, Jino George, Anoop Thomas, James A. Hutchison, Eloise Devaux, Cyriaque Genet, and Thomas W. Ebbesen. Non-radiative energy transfer mediated by hybrid light-matter states. *Angewandte Chemie International Edition*, 55(21):6202–6206, Apr 2016.

[58] Xiaolan Zhong, Thibault Chervy, Lei Zhang, Anoop Thomas, Jino George, Cyriaque Genet, James A. Hutchison, and Thomas W. Ebbesen. Energy transfer between spatially separated entangled molecules. *Angewandte Chemie International Edition*, 56(31):9034–9038, Jun 2017.

[59] Kyriacos Georgiou, Paolo Michetti, Lizhi Gai, Marco Cavazzini, Zhen Shen, and David G. Lidzey. Control over energy transfer between fluorescent bodipy dyes in a strongly coupled microcavity. *ACS Photonics*, 5(1):258–266, Dec 2017.

[60] E. Orgiu, J. George, J. A. Hutchison, E. Devaux, J. F. Dayen, B. Doudin, F. Stellacci, C. Genet, J. Schachenmayer, C. Genes, G. Pupillo, P. Samorì, and T W Ebbesen. Conductivity in organic semiconductors hybridized with the vacuum field. *Nature Materials*, 14(11):1123–1129, Sep 2015.

[61] Johannes Feist and Francisco J. Garcia-Vidal. Extraordinary exciton conductance induced by strong coupling. *Physical Review Letters*, 114(19):196402, May 2015.

[62] Shaojun Wang, Arkadiusz Mika, James A. Hutchison, Cyriaque Genet, Abdelaziz Jouaiti, Mir Wais Hosseini, and Thomas W. Ebbesen. Phase transition

of a perovskite strongly coupled to the vacuum field. *Nanoscale*, 6:7243–7248, 2014.

[63] Arko Graf, Laura Tropf, Yuriy Zakharko, Jana Zaumseil, and Malte C. Gather. Near-infrared exciton-polaritons in strongly coupled single-walled carbon nanotube microcavities. *Nature Communications*, 7(1):13078, Oct 2016.

[64] Vanik A. Shahnazaryan, Vasil A. Saroka, Ivan A. Shelykh, William L. Barnes, and Mikhail E. Portnoi. Strong light–matter coupling in carbon nanotubes as a route to exciton brightening. *ACS Photonics*, 6:904–914, Mar 2019.

[65] Igor Vurgaftman, Blake S. Simpkins, Adam D. Dunkelberger, and Jeffrey C. Owrutsky. Negligible effect of vibrational polaritons on chemical reaction rates via the density of states pathway. *The Journal of Physical Chemistry Letters*, 11(9):3557–3562, 2020.

[66] Thomas Stangl, Philipp Wilhelm, Klaas Remmerssen, Sigurd Höger, Jan Vogelsang, and John M. Lupton. Mesoscopic quantum emitters from deterministic aggregates of conjugated polymers. *Proceedings of the National Academy of Sciences*, 112(41):E5560–E5566, Sep 2015.

[67] Markus Pollnau and Marc Eichhorn. Spectral coherence, Part I: Passive-resonator linewidth, fundamental laser linewidth, and Schawlow-Townes approximation. *Progress in Quantum Electronics*, 72:100255, 2020.

[68] V. Savona and C. Piermarocchi. Microcavity polaritons: Homogeneous and inhomogeneous broadening in the strong coupling regime. *physica status solidi (a)*, 164(1):45–51, 1997.

[69] O. Sydoruk, E. Tatartschuk, E. Shamonina, and L. Solymar. Analytical formulation for the resonant frequency of split rings. *Journal of Applied Physics*, 105(1):014903, 2009.

[70] W Froncisz and James S Hyde. The loop-gap resonator: a new microwave lumped circuit esr sample structure. *Journal of Magnetic Resonance (1969)*, 47(3):515 – 521, 1982.

[71] W. N. Hardy and L. A. Whitehead. Split-ring resonator for use in magnetic resonance from 200–2000 mhz. *Review of Scientific Instruments*, 52(2):213–216, 1981.

[72] Stevens Chris J. Castles Flynn Grant Patrick S. Isakov, Dmitry. A split ring resonator dielectric probe for near-field dielectric imaging. *Scientific Reports*, 7(2038), 2017.

[73] J. E. Allen and S. E. Segre. The electric field in single-turn and multi-sector coils. *Il Nuovo Cimento (1955-1965)*, 21(6):980–987, Sep 1961.

[74] S. S. Seetharaman, B. Tremain, W. L. Barnes, and I. R. Hooper. Realizing an ultra-wideband backward-wave metamaterial waveguide. *Phys. Rev. B*, 98:235408, Dec 2018.

[75] E. Tatartschuk, N. Gneiding, F. Hesmer, A. Radkovskaya, and E. Shamonina. Mapping inter-element coupling in metamaterials: Scaling down to infrared. *Journal of Applied Physics*, 111(9):094904, 2012.

[76] J.-S. Hong. Couplings of asynchronously tuned coupled microwave resonators. *IEE Proceedings - Microwaves, Antennas and Propagation*, 147:354–358(4), October 2000.

[77] Leilei Yu, Yuanyuan Huang, Changji Liu, Fangrong Hu, Yanping Jin, Yi Yan, and Xinlong Xu. Giant plasmonic mode splitting in thz metamaterials mediated by coupling with lorentz phonon mode. *Applied Physics Letters*, 112(15):151101, 2018.

[78] J. Knoester. *Proceedings of the International School of Physics "Enrico Fermi" Course CLIX*, pages 149–186. IOS Press (Amsterdam), 2002.

[79] Frank C Spano and Carlos Silva. H- and J-aggregate behavior in polymeric semiconductors. *Annual Review of Physical Chemistry*, 65:477–500, 2014.

[80] J. Moll, S Daehne, J. R. Durrant, and D. A. Wiersma. Optical dynamics of

excitons in j aggregates of a carbocyanine dye. *Journal of Physical Chemistry*, 102:6362–6370, 1995.

[81] I. Pockrand, A. Brillante, and D Möbius. Exciton-surface plasmon coupling: an experimental investigation. *Journal of Chemical Physics*, 77(12):6289–6295, 1982.

[82] L. Gu, J. Livenere, G. Zhu, E. E. Narimanov, and M. A. Noginov. Quest for organic plasmonics. *Applied Physics Letters*, 103:021104, 2013.

[83] M. J. Gentile, S. Nunez-Sanchez, and W. L. Barnes. Optical field-enhancement and subwavelength field-confinement using excitonic nanostructures. *Nano Letters*, 14:2339–2344, 2014.

[84] Kentaro Takatori, Takayuki Okamoto, Koji Ishibashi, and Ruggero Micheletto. Surface exciton polaritons supported by a j-aggregate-dye/air interface at room temperature. *Opt. Lett.*, 42(19):3876–3879, Oct 2017.

[85] Carlos Gonzalez-Ballestero, Johannes Feist, Eduardo Gonzalo Badía, Esteban Moreno, and Francisco J. Garcia-Vidal. Uncoupled dark states can inherit polaritonic properties. *Phys. Rev. Lett.*, 117:156402, Oct 2016.

[86] Vladimir V Egorov. Theory of the J-band: From the Frenkel exciton to charge transfer. *Physics Procedia*, 2(2):223–326, 2009.

[87] J. Frenkel. On the transformation of light into heat in solids. i. *Phys. Rev.*, 37:17–44, Jan 1931.

[88] Sara C Massey, Po-Chieh Ting, Shu-Hao Yeh, Peter D Dahlberg, Sara H Sohail, Marco A Allodi, Elizabeth C Martin, Sabre Kais, C Neil Hunter, and Gregory S Engel. Orientational Dynamics of Transition Dipoles and Exciton Relaxation in LH2 from Ultrafast Two-Dimensional Anisotropy. *The Journal of Physical Chemistry Letters*, 10(2):270–277, 2019.

[89] Akira Hasegawa and Frederick Tappert. Transmission of stationary nonlinear

optical pulses in dispersive dielectric fibers. i. anomalous dispersion. *Applied Physics Letters*, 23(3):142–144, 1973.

[90] W. P. Su, J. R. Schrieffer, and A. J. Heeger. Solitons in polyacetylene. *Phys. Rev. Lett.*, 42:1698–1701, Jun 1979.

[91] Felipe Herrera and Jeffrey Owrutsky. Molecular polaritons for controlling chemistry with quantum optics. *Journal of Chemical Physics*, 152(10), 2020.

[92] S. A. Moskalenko and I. M. Tiginyanu. Exciton-polariton laser. *Low Temperature Physics*, 42(5):330–339, 2016.

[93] Olivier Bleu, Guangyao Li, Jesper Levinsen, and Meera M. Parish. Polariton interactions in microcavities with atomically thin semiconductor layers. *Phys. Rev. Research*, 2:043185, Nov 2020.

[94] D S Dovzhenko, S V Ryabchuk, Yu. P Rakovich, and I R Nabiev. Light–matter interaction in the strong coupling regime: configurations{,} conditions{,} and applications. *Nanoscale*, 10(8):3589–3605, 2018.

[95] Guido Van Rossum and Fred L Drake Jr. *Python tutorial*. Centrum voor Wiskunde en Informatica Amsterdam, The Netherlands, 1995.

[96] Charles R. Harris, K. Jarrod Millman, St'efan J. van der Walt, Ralf Gommers, Pauli Virtanen, David Cournapeau, Eric Wieser, Julian Taylor, Sebastian Berg, Nathaniel J. Smith, Robert Kern, Matti Picus, Stephan Hoyer, Marten H. van Kerkwijk, Matthew Brett, Allan Haldane, Jaime Fern'andez del R'ıo, Mark Wiebe, Pearu Peterson, Pierre G'erard-Marchant, Kevin Sheppard, Tyler Reddy, Warren Weckesser, Hameer Abbasi, Christoph Gohlke, and Travis E. Oliphant. Array programming with NumPy. *Nature*, 585(7825):357–362, September 2020.

[97] S. S. Seetharaman, C. G. King, I. R. Hooper, and W. L. Barnes. Electromagnetic interactions in a pair of coupled split-ring resonators. *Phys. Rev. B*, 96:085426, Aug 2017.

[98] H. Liu, D. A. Genov, D. M. Wu, Y. M. Liu, Z. W. Liu, C. Sun, S. N. Zhu, and X. Zhang. Magnetic plasmon hybridization and optical activity at optical frequencies in metallic nanostructures. *Physical Review B - Condensed Matter and Materials Physics*, 76:1–4, 2007.

[99] M. Decker, S. Linden, and M. Wegener. Coupling effects in low-symmetry planar split-ring resonator arrays. *Optics Letters*, 34:1579–1581, 2009.

[100] N. Liu and H. Giessen. Three-dimensional optical metamaterials as model systems for longitudinal and transverse magnetic coupling. *Optics Express*, 16:21233–8, 2008.

[101] I. V. Shadrivov, A. N. Reznik, and Y. S. Kivshar. Magnetoinductive waves in arrays of split-ring resonators. *Physica B: Condensed Matter*, 394:180–183, 2007.

[102] A. Radkovskaya, O. Sydoruk, M. Shamonin, E. Shamonina, C. J. Stevens, G. Faulkner, D. J. Edwards, and L. Solymar. Experimental study of a bi-periodic magnetoinductive waveguide: comparison with theory. *IET Microwav. Antennas Propag.*, 1:80–83, 2007.

[103] I. Sersic, M. Frimmer, E. Verhagen, and A. F. Koenderink. Electric and Magnetic Dipole Coupling in Near-Infrared Split-Ring Metamaterial Arrays. *Physical Review Letters*, 103:1–4, 2009.

[104] M. Lapine, D. Powell, M. Gorkunov, I. Shadrivov, R. Marqués, and Y. Kivshar. Structural tunability in metamaterials. *Applied Physics Letters*, 95:23–26, 2009.

[105] D. R. Smith, J. Gollub, J. J. Mock, W. J. Padilla, and D. Schurig. Calculation and measurement of bianisotropy in a split ring resonator metamaterial. *Journal of Applied Physics*, 100:024507, 2006.

[106] X. Liu, H. Liu, Q. Sun, and N. Huang. Metamaterial terahertz switch based on split-ring resonator embedded with photoconductive silicon. *Appl. Opt.*, 54:3478–3483, 2015.

[107] A. Ishikawa and T. Tanaka. Negative magnetic permeability of split ring resonators in the visible light region. *Optics Communications*, 258:300 – 305, 2006.

[108] A. A. Oliner. A planar negative-refractive-index medium without resonant elements. *IEEE MTT-S International Microwave Symposium Digest, 2003*, 1:191–194, 2003.

[109] N. Kundtz and D. R. Smith. Extreme-angle broadband metamaterial lens. *Nat. Mater.*, 9:129–132, 2010.

[110] D. A. Powell, M. Lapine, M. V. Gorkunov, I. V. Shadrivov, and Y. S. Kivshar. Metamaterial tuning by manipulation of near-field interaction. *Physical Review B*, 82:1–8, 2010.

[111] D. A. Powell, K. Hannam, I. V. Shadrivov, and Y. S. Kivshar. Near-field interaction of twisted split-ring resonators. *Physical Review B - Condensed Matter and Materials Physics*, 83:1–6, 2011.

[112] Hongfeng Gai, Ji-a Wang, and Qian Tian. Tuning the resonant wavelength of a nanometric bow-tie aperture by altering the relative permittivity of the dielectric substrate. *Journal of Nanophotonics - J NANOPHOTONICS*, 1, 01 2007.

[113] X Wang, P Bao, and T J Jackson M J Lancaster. Tunable microwave filters based on discrete ferroelectric and semiconductor varactors. *IET Microwaves, Antennas and Propagation*, 5(December 2010):776–782, 2011.

[114] D. A. Powell, I. V. Shadrivov, Y. S. Kivshar, and M. V. Gorkunov. Self-tuning mechanisms of nonlinear split-ring resonators. *Applied Physics Letters*, 91(14):144107, October 2007.

[115] Kwok Kwok Ng. *p-n Junction Diode*, chapter 1, pages 11–23. John Wiley Sons, Ltd, 2010.

[116] D. M. Pozar. *Microwave Engineering*. Wiley, 2004.

[117] J. D. Baena, J. Bonache, F. Martin, R. M. Sillero, F. Falcone, T. Lopetegi, M. A. G. Laso, J. Garcia-Garcia, I. Gil, M. F. Portillo, and M. Sorolla. Equivalent-circuit models for split-ring resonators and complementary split-ring resonators coupled to planar transmission lines. *IEEE Transactions on Microwave Theory and Techniques*, 53(4):1451–1461, 2005.

[118] L. Novotny. Strong coupling, energy splitting, and level crossings: A classical perspective. *American Journal of Physics*, 78:1199, 2010.

[119] Na Liu, Hui Liu, Shining Zhu, and Harald Giessen. Stereometamaterials. *Nature Photonics*, 3(3):157–162, 2009.

[120] P. Gay-Balmaz and O. Martin. Electromagnetic resonances in individual and coupled split-ring resonators. *Journal of Applied Physics*, 92:2929–2936, 2002.

[121] A. Eisfeld, S. M. Vlaming, V. A. Malyshev, and J. Knoester. Excitons in molecular aggregates with lévy-type disorder: Anomalous localization and exchange broadening of optical spectra. *Physical Review Letters*, 105(13):137402, Sep 2010.

[122] Diederik S. Wiersma. Disordered photonics. *Nature Photonics*, 7(3):188–196, Feb 2013.

[123] Parinda Vasa, Wei Wang, Robert Pomraenke, Melanie Lammers, Margherita Maiuri, Cristian Manzoni, Giulio Cerullo, and Christoph Lienau. Real-time observation of ultrafast rabi oscillations between excitons and plasmons in metal nanostructures with j-aggregates. *Nature Photonics*, 7(2):128–132, Jan 2013.

[124] Stewart D. Jenkins, Nikitas Papasimakis, Salvatore Savo, Nikolay I. Zheludev, and Janne Ruostekoski. Strong interactions and subradiance in disordered metamaterials. *Physical Review B*, 98(24):245136, Dec 2018.

[125] François Dubin, Romain Melet, Thierry Barisien, Roger Grousson, Laurent Legrand, Michel Schott, and Valia Voliotis. Macroscopic coherence of a single

exciton state in an organic quantum wire. *Nature Physics*, 2(1):32–35, Jan 2006.

[126] D. Chaudhuri, D. Li, Y. Che, E. Shafran, J. M. Gerton, and J. M. Lupton. Enhancing long-range exciton guiding in molecular nanowires by h-aggregation lifetime engineering. *Nano Letters*, 11:488–492, 2011.

[127] Andreas T. Haedler, Klaus Kreger, Abey Issac, Bernd Wittmann, Milan Kivala, Natalie Hammer, Jürgen Köhler, Hans-Werner Schmidt, and Richard Hildner. Long-range energy transport in single supramolecular nanofibres at room temperature. *Nature*, 523(7559):196–199, Jul 2015.

[128] Justin R. Caram, Sandra Doria, Dörthe M. Eisele, Francesca S. Freyria, Timothy S. Sinclair, Patrick Rebentrost, Seth Lloyd, and Moungi G. Bawendi. Room-temperature micron-scale exciton migration in a stabilized emissive molecular aggregate. *Nano Letters*, 16(11):6808–6815, Oct 2016.

[129] E. Prodan, C. Radloff, N. J. Halas, and P. Nordlander. A hybridization model for the plasmon response of complex nanostructures. *Science*, 302:419–422, 2003.

[130] Meng Gao and Ben Zhong Tang. Fluorescent sensors based on aggregation-induced emission: Recent advances and perspectives. *ACS Sensors*, 2(10):1382–1399, Sep 2017.

[131] Tu N. Nguyen, Wolfgang Wernsdorfer, Muhandis Shiddiq, Khalil A. Abboud, Stephen Hill, and George Christou. Supramolecular aggregates of single-molecule magnets: exchange-biased quantum tunneling of magnetization in a rectangular [mn3]4 tetramer. *Chemical Science*, 7(2):1156–1173, 2016.

[132] Semion K. Saikin, Alexander Eisfeld, Stéphanie Valleau, and Alán Aspuru-Guzik. Photonics meets excitonics: natural and artificial molecular aggregates. *Nanophotonics*, 2(1):21–38, Jan 2013.

[133] Lord Rayleigh and A. Schuster. On the determination of the ohm in absolute measure. *Proceedings of the Royal Society*, 32:104–141, 1881.

[134] F. W. Grover. *Inductance calculations (Ch 16)*. Dover (New York), 2009.

[135] A. Radkovskaya, M. Shamonin, C. J. Stevens, G. Faulkner, D. J. Edwards, and L. Shamonina, E. Solymar. Resonant frequencies of a combination of split rings: Experimental, analytical and numerical study. *Microwave and Optical Technology Letters*, 46:473–476, 2005.

[136] A. Kurs, A. Karalis, R. Moffatt, and J. D. Joannopoulos. Wireless power transfer via strongly coupled magnetic resonances. *Science*, 317:83–86, 2007.

[137] Navketan Batra and Goutam Sheet. Understanding basic concepts of topological insulators through su-schrieffer-heeger (ssh) model. 2019.

[138] Eric J Meier, Fangzhao Alex An, and Bryce Gadway. Observation of the topological soliton state in the Su–Schrieffer–Heeger model. *Nature Communications*, 7(1):13986, 2016.

[139] S.-R. Eric Yang. Soliton Fractional Charges in Graphene Nanoribbon and Polyacetylene: Similarities and Differences. *Nanomaterials*, 9(6):1–16, 2019.

[140] W. P. Su, J. R. Schrieffer, and A. J. Heeger. Soliton excitations in polyacetylene. *Phys. Rev. B*, 22:2099–2111, Aug 1980.

[141] A. J. Heeger, S. Kivelson, J. R. Schrieffer, and W. P. Su. Solitons in conducting polymers. *Rev. Mod. Phys.*, 60:781–850, Jul 1988.

[142] Abu Md. Asaduzzaman, Karla Schmidt-D'Aloisio, Yi Dong, and Michael Springborg. Properties of polythiophene and related conjugated polymers: a density-functional study. *Phys. Chem. Chem. Phys.*, 7:2714–2722, 2005.

[143] P. A. Hobson, W. L. Barnes, D. G. Lidzey, G. A. Gehring, D. M. Whittaker, M. S. Skolnick, and S. Walker. Strong exciton–photon coupling in a low-q all-metal mirror microcavity. *Applied Physics Letters*, 81(19):3519–3521, Nov 2002.

[144] T. Schwartz, J. A. Hutchison, C. Genet, and T. W. Ebbesen. Reversible switching of ultrastrong light-molecule coupling. *Physical Review Letters*, 106(19):196405, May 2011.

[145] Merav Muallem, Alexander Palatnik, Gilbert D. Nessim, and Yaakov R. Tischler. Strong light-matter coupling and hybridization of molecular vibrations in a low-loss infrared microcavity. *The Journal of Physical Chemistry Letters*, 7(11):2002–2008, May 2016.

[146] Laura Tropf and Malte C. Gather. Investigating the onset of the strong coupling regime by fine-tuning the rabi splitting in multilayer organic microcavities. *Advanced Optical Materials*, 6(17):1800203, Jun 2018.

[147] J. J. Hopfield. Theory of the contribution of excitons to the complex dielectric constant of crystals. *Phys. Rev.*, 112:1555–1567, Dec 1958.

[148] S. S. Seetharaman, C. G. King, I. R. Hooper, and W. L. Barnes. Electromagnetic interactions in a pair of coupled split-ring resonators. *Physical Review B*, 96(8):085426, Aug 2017.

[149] V. Savona and F. Tassone. Exact quantum calculation of polartion dispersion in semiconductor microcavities. *Solida State Communications*, 95:673–678, 1995.

[150] P. A Thomas, W. J. Tan, H. A. Fernandez, and W. L. Barnes. A new signature for strong light-matter coupling using spectroscopic ellipsometry. *Nano Letters*, 20:6412–6419, 2020.

[151] D. Bajoni. Polariton lasers. hybrid light-matter lasers without inversion. *Journal of Physics D: Applied Physics*, 45:313001, 2012.

[152] W.-C. Chen, C. M. Bingham, K. M. Mak, N. W. Caira, and W. J. Padilla. Extremely subwavelength planar magnetic metamaterials. *Physical Review B*, 85(20):201104R, May 2012.

[153] G. McDermott, S. M. Prince, A. A. Freer, A. M. Hawthornethwaite-Lawless, M. Z. Papiz, R. J. Cogdell, and N. W. Isaacs. Crystal structure of an integral membrane light-harvesting complex from photosynthetic bacteria. *Nature*, 374:517–521, 1995.

[154] Chaw-Keong Yong, Patrick Parkinson, Dmitry V. Kondratuk, Wei-Hsin Chen, Andrew Stannard, Alex Summerfield, Johannes K. Sprafke, Melanie C. O'Sullivan, Peter H. Beton, Harry L. Anderson, and Laura M. Herz. Ultrafast delocalization of excitation in synthetic light-harvesting nanorings. *Chemical Science*, 6(1):181–189, 2015.

[155] Wonjun Choi, Cheng Yin, Ian R. Hooper, William L. Barnes, and Jacopo Bertolotti. Absence of anderson localization in certain random lattices. *Phys. Rev. E*, 96:022122, Aug 2017.

[156] Arko Graf, Laura Tropf, Yuriy Zakharko, Jana Zaumseil, and Malte Gather. Near-infrared exciton-polaritons in strongly coupled single-walled carbon nanotube microcavities. *Nature Communications*, 7:13078, 11 2016.